NANOMANUFACTURING OF WEARABLE ELECTRONICS FOR ENERGY CONVERSION AND HUMAN-INTEGRATED MONITORING

by

Min Wu

A Dissertation

Submitted to the Faculty of Purdue University

In Partial Fulfillment of the Requirements for the degree of

Doctor of Philosophy

School of Industrial Engineering

West Lafayette, Indiana

December 2020

THE PURDUE UNIVERSITY GRADUATE SCHOOL
STATEMENT OF COMMITTEE APPROVAL

Dr. Wenzhuo Wu, Chair

School of Industrial Engineering

Dr. Gary Cheng

School of Industrial Engineering

Dr. Ramses Martinez

School of Industrial Engineering

Dr. Benxin Wu

School of Mechanical Engineering

Approved by:

Dr. Abhijit Deshmukh

Dedicated to my beloved family

ACKNOWLEDGMENTS

Throughout the writing of this dissertation I have received a great deal of support and assistance. My deep gratitude goes first to my advisor Professor Wenzhuo Wu, who expertly guided me through my graduate education. His extensive knowledge, enthusiasm for research, and also the vision and motivation have greatly inspired me. He has taught me the methodology to carry out the research and to present the research works as clearly as possible. It was a greatly privilege and honor to work and study under his guidance. I would also like to thank him for his friendship and empathy.

My appreciation also extends to my committee members: Professor Gary Cheng, Professor Ramses Martinez, Professor Benxin Wu. They all have provided me with many strategic and precious suggestions for my research work.

I would also like to thank my colleagues in our research group. Dr. Yixiu Wang, Dr. Chenxiang Ma, Mr. Shengjie Gao, Ms. Ruoxing Wang have helped me a lot with my research projects. We also cooperated on some research projects and made some exciting research progress, I really enjoyed the collaborations with them. I also would like to thank other lab members, Mr. Mo Lv, Mr. Shihan Wan, Mr. Xiongchao Chen, Ms. Yihui Ma, Ms. Nianzu Liu, Ms. Ruifang Zhang, Mr. Mingyi Wang, Mr. Shujia Xu, Mr. Qiang He, Ms. Hongmei Yang, Ms. Jing Jiang, Mr. Meng Hao Lee. Thanks for being so kind and I will definitely miss the days in Wu Group.

I would also like express my great appreciation to my family, who have always been there for me no matter where I am, for all unconditional supports and patience. Thank you for being ever so understanding and supportive.

TABLE OF CONTENTS

LIST OF FIGURES

LIST OF SYMBOLS

μ	Mobility
t	Thickness
R	Contact Resistance
V_{sd}	Source-to-Drain Voltage
V_{oc}	Open-circuit Voltage
I_{sc}	Short-circuit Current
Q_{sc}	Short-circuit Transferred Charges
τ_y	Yield Stress
σ	Nominal Stress
ε	Tensile Strain
G’	Storage Modulus
G’’	Loss Modulus

LIST OF ABBREVIATIONS

PENG	Piezoelectric Nanogenerator
TENG	Triboelectric Nanogenerator
AM	Additive Manufacturing
SL	Stereolithography
SLS	Selective Laser Sintering
CAD	Computer Aided Design
2D	Two-Dimensional
TEM	Transmission Electron Microscopy
vdW	van der Waals
1D	One-Dimensional
AFM	Atomic Force Microscopy
XRD	X-ray Powder Diffraction
LB	Langmuir-Blodgett
HRTEM	High Resolution Transmission Electron Microscopy
EDS	Energy Dispersive X-ray Spectrometry
SAED	Selected-Area Electron-Diffraction
FTIR	Fourier-transform infrared spectroscopy
DIW	Direct Ink Writing

NOMENCLATURE

Se	Selenium
SeO_2	Selenium Dioxide
Te	Tellurium
Cu	Copper
Ag	Silver
N_2H_4	Hydrazine
Na_2TeO_3	Sodium Tellurite
$C_6H_{12}O_6$	Glucose
PVP	Polyvinylpyrrolidone
PDMS	Polydimethylsiloxane
NaOH	Sodium Hydroxide
DMF	N,N-dimethylformamide
$CHCl_3$	Chloroform
SiO_2	Silicone Dioxide
CMC	Carboxymethyl Cellulose
SA	Sodium Alginate

ABSTRACT

Recently, energy crisis and environment pollution has become global issues and there is a great demand for developing green and renewable energy system. At the same time, advancements in materials production, device fabrication, and flexible circuit has led to the huge prosperity of wearable devices, which also requires facile and efficient approaches to power these ubiquitous electronics. Piezoelectric nanogenerators and triboelectric nanogenerators have attracted enormous interest in recent years due to their capacity of transferring the ambient mechanical energy into desired electricity, and also the potential of working as self-powered sensors. However, there still exists some obstacles in the aspect of materials synthesis, device fabrication, and also the sensor performance optimization as well as their application exploration.

Here in this research, several different materials possessing the piezoelectric and triboelectric properties (selenium nanowires, tellurium nanowires, natural polymer hydrogel) have been successfully synthesized, and also a few novel manufacturing techniques (additive manufacturing) have been implemented for the fabrication of wearable sensors. The piezoelectric and triboelectric nanogenerators developed could effectively convert the mechanical energy into electricity for an energy conversion purpose, and also their application as self-powered human-integrated sensors have also been demonstrated, like achieving a real-time monitoring of radial artery pulses. Other applications of the developed sensors, such as serving as electric heaters and infrared cloaking devices are also presented here. This research is expected to have a positive impact and immediate relevance to many societally pervasive areas, e.g. energy and environment, biomedical electronics, and human-machine interface.

1. INTRODUCTION

1.1 Piezoelectric and Triboelectric Nanogenerators

1.1.1 Principle of piezoelectric and triboelectric nanogenerators

Piezoelectric nanogenerators, which could effectively convert the external kinetic energy into electrical energy via nano-structured piezoelectric material, has attracted enormous research interest since its invention by Wang et al. in 2006[1]. The principle of piezoelectric nanogenerator originates from the piezoelectric property found in non-centrosymmetric material. Take the ZnO crystal of wurtzite-structured as example, the tetrahedrally coordinated Zn^{2+} and O^{2-} are accumulated layer-by-layer along the c-axis. At its original state, the charge center of the anions and cations coincide with each another. Once applying an external force, the structure is deformed (stretching or compressing). Therefore, the negative and positive charge centers are separated and form an electric dipole leading to a piezoelectric potential[2]. If an external load is connected to the deformed material, the free electrons are driven to partially screen the piezoelectric potential and flow through the external circuit to realize a new equilibrium state. Therefore, a current pulse flowing through the external circuit is continuously generated when the piezoelectric potential is altered sequentially by applying a dynamic external force. This primary mechanism of piezoelectric potential generation applies to various piezoelectric materials. Taking advantage of the piezoelectric properties of non-centrosymmetric materials, various types of PENG device have been fabricated and demonstrated to be capable of transferring the ambient mechanical energy into our desired electrical format.

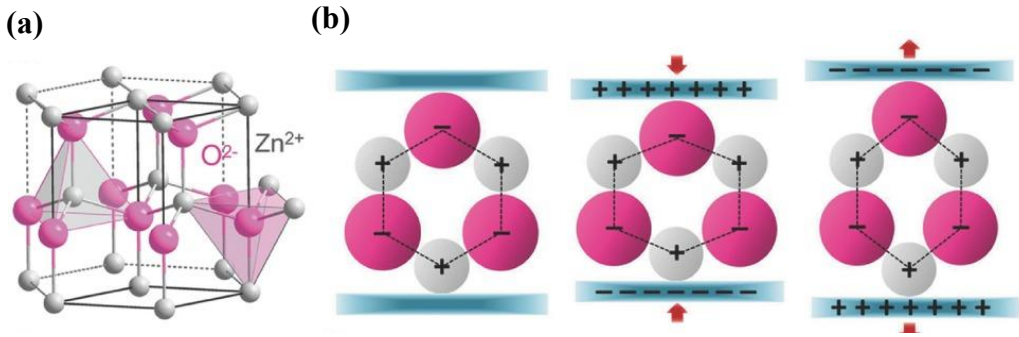

Figure 1.1 (a) Atomic model of the wurtzite-structured ZnO. (b) Different piezo potential in tension and compression modes of the PENG[2].

Triboelectric nanogenerators (TENGs), which relies on the principles of triboelectric effect and the electrostatic induction from two materials that exhibit opposite tribo-polarity[3], have much less dependency on the material categories as compared to the PENGs. The most typical TENG devices are based on the vertical contact-separation mode[4]. Initially, when two materials with different tribopolarity get contacted, a charges transfer will begin at the inner surfaces of the two sheets, making one surface negatively charged and the other positively charged. When the two sheets are moved away from each other, an electrical potential difference is built between the two separated oppositely charged surfaces. Then a transient charge flows between the two electrodes, generating a current pulse. An electrostatic equilibrium is achieved when the two sheets reach the maximum separation distance. As the two sheets moved back again and get contacted, the process is reversed, thus a charge flow along the opposite direction appears. In this way, the continual contact-separation motion described above produces an alternative current.

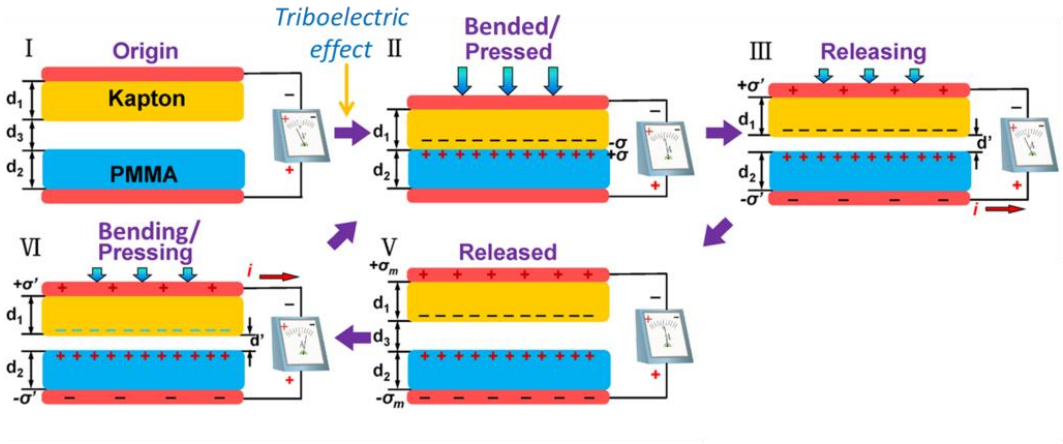

Figure 1.2 Schematic of the vertical contact-separation mode of triboelectric nanogenerator[4].

1.1.2 Application of PENGs and TENGs

Currently, both PENGs and TENGs have been widely implemented for the energy harvesting purpose, they can be applied to harvest all kind mechanical energy that is available but wasted in our daily life, such as human motion, walking, vibration, mechanical triggering, rotating tire, wind, flowing water and more[5]. The energy conversion efficiency as well as the output power density of the PENGs and TENGs have been improved for several orders of magnitude in recent years[6]. On the other hand, since the PENGs and TENGs devices are quite sensitive to very tiny mechanical vibrations, they can be utilized to work as self-powered sensors to detect the trivial mechanical

agitations[7]. One of the most important applications of the PENGs and TENGs is in the field of human-integrated monitoring[8]. There are already some reports about utilizing the PENGs and TENGs sensors for physiological monitoring purpose[9].

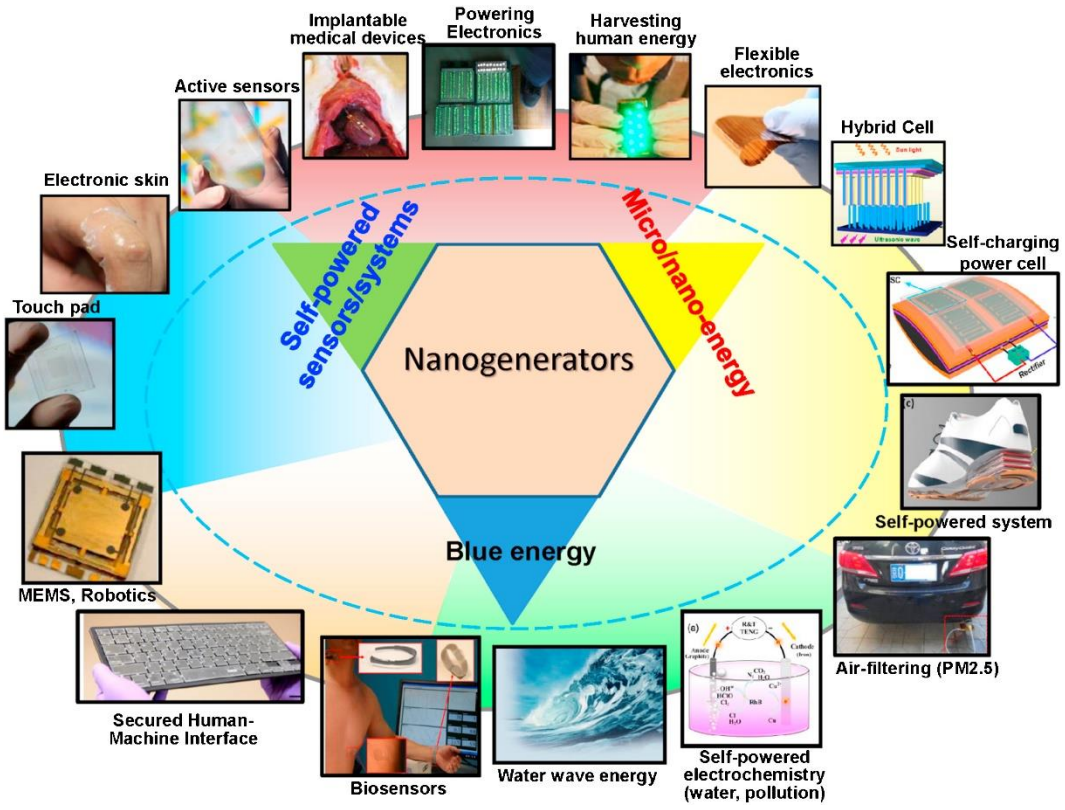

Figure 1.3 A summary about the three major application fields of nanogenerators as micro-/nano-energy source, for blue energy and self-powered sensors[5].

1.2 Additive Manufacturing

1.2.1 Category of additive manufacturing

Additive Manufacturing, also called 3D printing, has gradually evolved into one popular method for the fabrication of three-dimensional objects[10]. As compared to the conventional bottom-up manufacturing method like lathing and casting, additive manufacturing enjoyed many advantages in the aspect of fabrication time, materials cost, and also the possibility of constructing more complex structures. The 3D printing process starts with constructing a 3D model using the CAD, then proceeds to print the object layer by layer with the extruder movement. Recently, a couple of different 3D printing methods have been developed, including but not limited to direct ink

writing[11], selective laser sintering[12], and stereolithography[13]. Researchers and engineers have already realized the 3D printing with metals[14], plastics[15], polymers[16] as the raw materials, and we already find the wide applications of the 3D printed objects in the field of aerospace, biomedicine, etc.

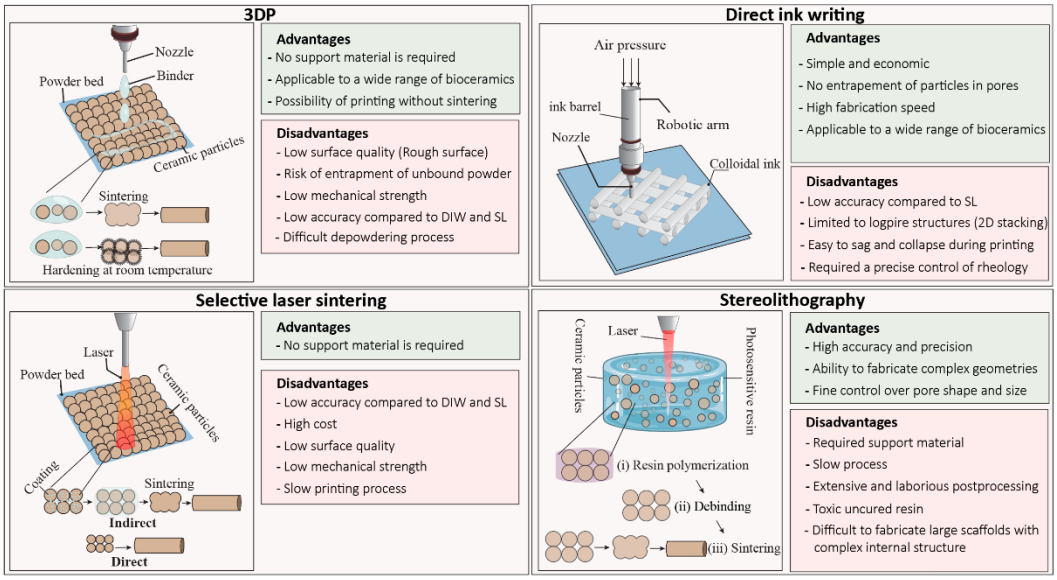

Figure 1.4 Schematic of common additive manufacturing techniques including 3D printing (3DP), direct-ink writing (DIW), stereolithography (SL), and selective laser sintering (SLS) for printing bio ceramic scaffolds and their advantages and disadvantages[17].

1.2.2 Direct ink writing of hydrogel electronics

Due to the differences between the soft, wet, and living biological tissues and rigid, dry and synthetic electronic systems, it is challenging to develop an effective, compatible and stable interface between the human bodies and the wearable electronics[18]. In recent years, hydrogel has emerged to be a promising candidate for the next-generation bioelectronics interfaces and have received much research attention[19]. Hydrogel shares pretty many similarities to the body tissues in the aspect of mechanical and electrical properties, and also has exceptional biocompatibility which is imperative in the bioelectronics design and fabrication. Currently there are already many researches and practical applications of hydrogels utilized as bioelectronic electrodes for biomedical stimulation / recording, or as coatings and encapsulations for bioelectronic devices / medicines modification.

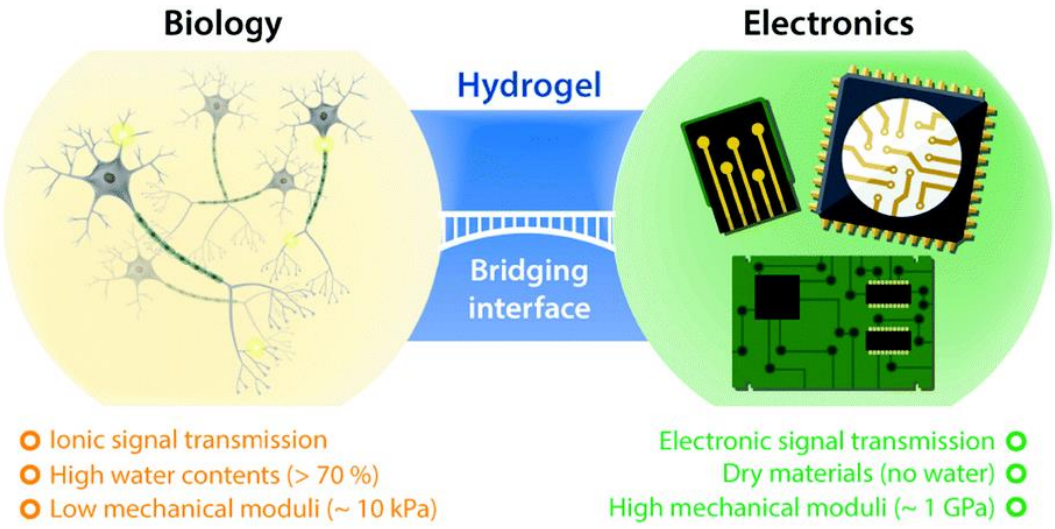

Figure 1.5 hydrogel used as electronic interfaces between the biology and the electronic system[18].

Direct-ink-writing has proven to be an effective and efficient approach for the fabrication of hydrogel electronics[20]. By tailoring the viscosity and other rheological properties of the hydrogel precursor ink coupled with the 3D printing process design, the DIW technique would help construct arbitrary, delicate, and continuous hydrogel structures.

1.3 Metal-nanowires network as electrical heaters and IR cloaking devices

The meatal nanowires (Cu, Ag nanowires) have intrinsic properties like good thermal and electrical conductivity, high aspect ratio, low sheet resistance, excellent optical transparency, etc[21]. It has been demonstrated when these nanowires are carefully deposited and embedded onto the surfaces of soft elastomers, they will form a conductive network which is capable of withstanding a relative high stretchability, an example has been illustrated in Figure 1.6[22]. The as-fabricated devices could be utilized as an efficient electrical heater which then applied as thermal therapy pads, their softness ensures the conformability when worn by human bodies.

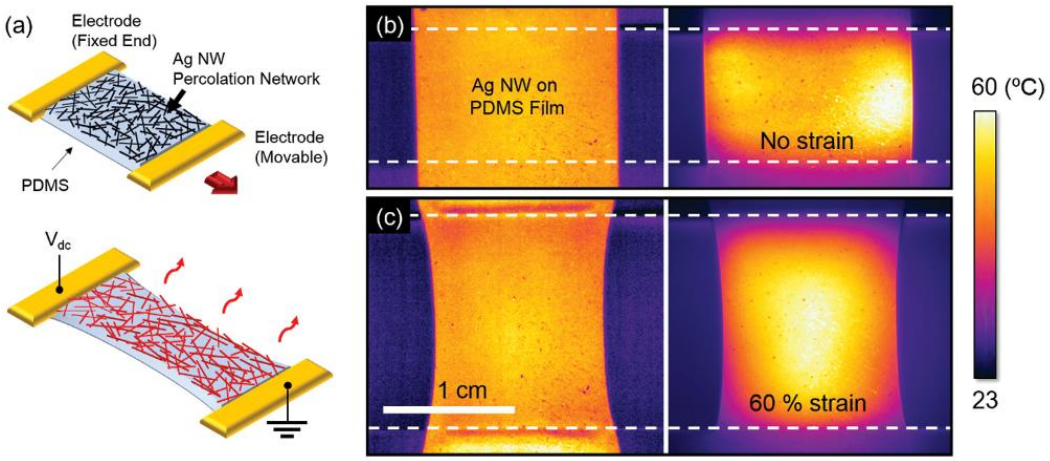

Figure 1.6 Highly stretchable and transparent heater based on Ag nanowires network[22].

In addition, the metal nanowires also are endowed with a low infrared emissivity, in recent reports it has been shown that the device consisting of metal nanowires could effectively block the majority of the infrared emissions, and help conceal the hot object under the detection of IR camera[23].

Figure 1.7 Thermal images under IR camera for the S-shaped Ag nanowires cloth[23].

1.4 Outline of the dissertation

Although currently numerous PENG and TENG devices have been invented and gradually found applications for energy harvesting or sensing purpose, but there still exists some obstacles needing to be tackled, like the limited classes of the suitable piezoelectric materials or triboelectrically responsive materials, cumbersome manufacturing process and the associated high cost, as well as the compatibility when integrated with human bodies as biosensors.

In this dissertation, we have developed a new class of piezoelectrical material, the trigonal-structured selenium (t-Se) nanowires and explored its application for human physiological monitoring. The t-Se material is synthesized via a low-cost solution-grown method, and also the piezoelectric devices is prepared via a facile Langmuir-Blodgett (LB) assembly of the Se nanowires. Device made could effectively harvest the mechanical energy, and be extended for applications for human-integrated monitoring.

Traditional manufacturing steps for the PENG and TENG devices fabrication usually involve complex steps like mold casting, which greatly affects the efficiency. Here we have implemented the novel 3D printing methods for the PENG and TENG devices manufacturing, a couple of piezoelectric and triboelectric devices with complex structures could be successfully fabricated, which could effectively alter the mechanical properties of the devices and enhance their piezoelectric / triboelectric output.

We also explored the application of hydrogel materials as triboelectric active layer in the TENG device. The DIW technique has been applied for the fabrication of hydrogel TENG device. Thanks to the softness and the high compatibility, the chitosan hydrogel based TENG could work as wearable sensors for self-powered cardiovascular monitoring.

In the last part of this dissertation, we have prepared conductive composite hydrogel via 3D printing method, which could then act as electrical heaters and also IR cloaking devices.

2. HIGHLY DURABLE AND STRETCHABLE PIEZOELECTRIC NANOGENERATOR BASED ON SELENIUM NANOWIRES FOR HUMAN PHYSIOLOGICAL MONITORING

2.1 Introduction

In 2006, Wang *et al* invented ZnO-based piezoelectric nanogenerators (PENG) which could realize the conversion of mechanical energy from ambient environment into electrical power[1]. Since then, the harvesting of mechanical energy using nanostructured piezoelectric materials has received considerable attentions, including wurtzite materials like GaN[24-26], CdS[27-28], perovskite materials like $BaTiO_3$[29-32], $ZnSnO_3$[33-35], other inorganic lead-free piezoelectric material[36-37] and also synthetic polymers such as PVDF and its copolymers[38-40]. The low-dimensional geometries, superior mechanical properties of piezoelectric nanomaterials compared to their bulk counterparts, and the direct energy conversion in piezoelectric process facilitate the integration into deformable devices for efficiently harvesting ubiquitous mechanical energy, hinged on principles of the time-variant piezoelectric polarization induced displacement current[5]. Ongoing efforts in the field of PENG are primarily focused on improving energy conversion by further enhancing the materials' piezoelectric properties[38, 41-43] and demonstrating proof-of-concept application[44]. Progress in these fields combined with the emerging methods for deterministic production and assembly of nanomaterials[42], leads to exciting research opportunities. Nevertheless, significant roadblocks exist for realizing the technological potential of existing piezoelectric nanomaterials. For instance, the sophisticated process for synthesizing wurtzite-structured piezoelectric nanowires with orientation control limit the potential device integration and applications[45-47]. Obstacles concerning scalable, economic production of piezoelectric nanomaterials with desired piezoelectric and mechanical properties continue to prevail.

Here we demonstrate for the first time scalable synthesis and integration of selenium (Se) nanowires into wearable piezoelectric devices, and explore the feasibility of such devices for self-powered sensing applications, e.g., physiological monitoring. The ultrathin device can be conformably worn onto the human wrist, effectively converting the imperceptible time-variant mechanical vibration from human body into distinguishable electrical signals through straining the piezoelectric Se nanowires.

The trigonal-structured selenium (t-Se) has an anisotropic crystal lattice where individual chiral chains of Se atoms are stacked together by weak bonding[48-49] (Figure 2.1). Each Se atom is covalently bonded with its two nearest neighbors on the same chain. t-Se has the same non-centrosymmetric structure to that of trigonal-structured tellurium (t-Te)[50-51]. Lee et al previously demonstrated the application of t-Te nanowires for piezoelectric nanogenerator[52]. The solution-synthesized t-Te nanowires are assembled horizontally on the flexible polyimide substrates, and can generate a power density up to 9 mW/cm^3 upon straining. However, the narrow bandgap[53] of metalloid tellurium may limit the piezoelectric application of t-Te nanowires. In contrast, selenium has a sizeable bandgap of 1.7 eV[54-55], and the nanostructured t-Se is expected to exhibit strong piezoelectric property[56], leading to a potential high volume-power-density in integrated devices. Similar to t-Te nanowire, the radial distribution of the piezoelectric polarization in t-Se nanowire, due to the strain-induced relative displacement of the electron distribution against the Se atoms cores[57], facilitates its integration into ultrathin laminated devices through economic manufacturing approaches, e.g. roll-to-roll (R2R) printing, onto various substrates[58].

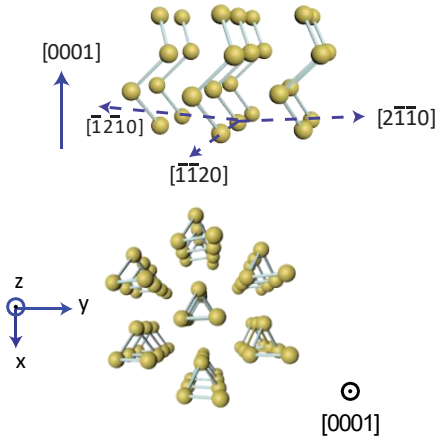

Figure 2.1 Schematic of the crystal structure of Se nanowires.

2.2 Materials Synthesis and Device Fabrication for Se-PENG

2.2.1 Synthesis of Se nanowires

The synthesis of Se nanowire follows procedures similar to previous report[59] with modified synthesis parameters to achieve uniform dimension of the as-synthesized nanowires. Specifically, selenium dioxide (SeO_2), glucose ($C_6H_{12}O_6$), and poly(vinylprrolidone) (PVP, MW ≈ 55 000) were

dissolved in a mixture of deionized (DI) water and ethanol (1:1 ratio). After constant stirring for 20 mins, 5 mL ammonia ($NH_3.H_2O$, 69%) was added into the solution to adjust the pH value. The mixture solution was then transferred to a Teflon-lined autoclave and heated to 160 °C for 20 h. After the reaction, the product was collected by centrifugation and washed several times with DI water to remove the impurities. All the chemicals were purchased from Sigma-Aldrich and used as received.

2.2.2 Assembly of Se nanowires

After obtaining the centrifuged Se nanowires products, N, N-dimethyformamide (DMF) was added to disperse the Se nanowires and form a homogeneous solution. Chloroform ($CHCl_3$) was then added into the homogeneous solution, which was ready for the subsequent Langmuir-Blodgett (LB) assembly and transfer of Se nanowires onto the various substrates for further characterization.

2.2.3 Materials characterizations

Morphology and structural characterization of the as-synthesized Se nanowires was performed using a field emission scanning electron microscope (Hitachi S-4800) and a wide-angle X-ray diffractomer in the 20-70° range (Bruker, D8 Advance Diffractomer).

The morphology of the as-synthesized Se nanowires can be seen in Figure 2.2. The length of the nanowires ranges from tens of μm to 100 μm, while the diameter is ~ 500 nm. Figures 2.2-1 and 2.2-3 present the morphology of the Se nanowires before the assembly, and Figures 2.2-2 and 2.2-4 show the Se nanowires after the LB assembly forming a close-packed film with oriented Se nanowires. X-Ray diffraction (XRD) was used to characterize the structure of the product. All the peaks in the XRD pattern (blue line) in Figure 2.3 can be assigned to the pure trigonal phase of Se with lattice parameters of a = 4.36 Å and c = 4.97 Å (JCPDS 86-2246). No XRD peaks arising from impurities could be detected, indicating that only elemental Se nanowires with high crystallinity and purity were derived. Compared with standard pattern of t-Se, it is found that the intensity of (hki0) reflection peaks of our synthesized Se nanowires is very strong, which suggests that the as-obtained t-Se crystals have a preferential growth orientation of [0001]. Interestingly, when the Se nanowires are assembled and transferred onto the substrate, some high-index peaks vanish in the XRD pattern (red line in Figure 2.3) with the two most prominent peaks arising from

the $(10\bar{1}0)$ and $(11\bar{2}0)$ planes. Such changes in the XRD patterns are consistent with the observed alignment of the Se nanowires in the horizontal plane after the LB assembly (Figure 2.2).

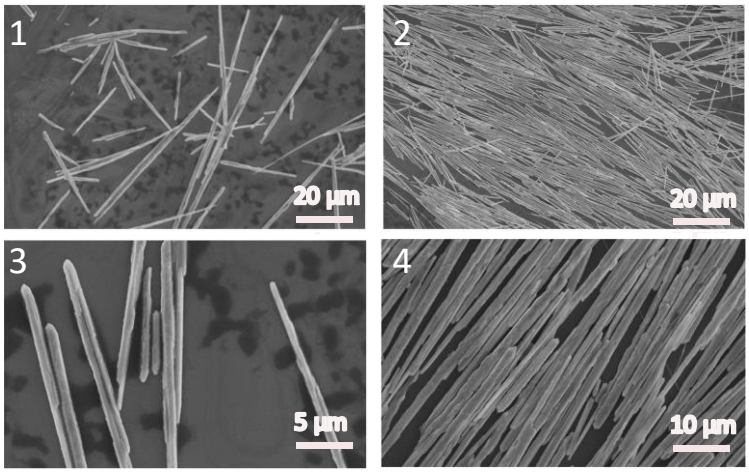

Figure 2.2 SEM images of the as-synthesized Se nanowires and the assembled Se nanowires film.

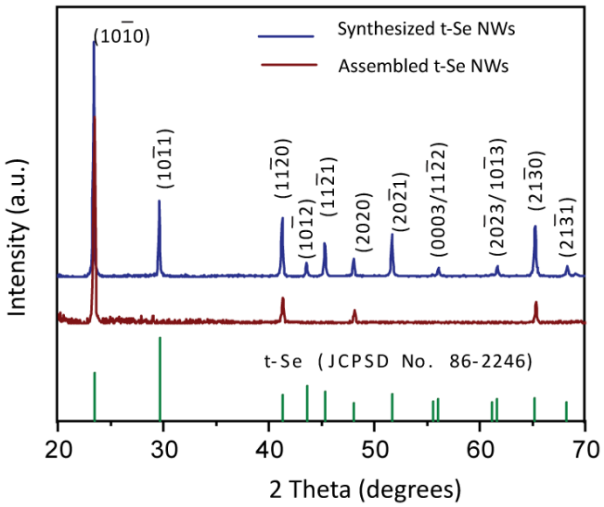

Figure 2.3 XRD patterns of the as-synthesized Se nanowires and assembled film.

2.2.4 Fabrication of the final Se-PENG device

Firstly, a thin layer of polydimethylsiloxane (PDMS) was spin-coated onto a PET substrate. After curing at 90 ℃, the PDMS layer was treated with oxygen plasma for deriving a hydrophilic surface. Afterwards, a layer of Ag nanowires network was spray-coated to function as the bottom electrode. Then, another layer of PDMS was deposited onto the Ag nanowire layer and cured.

Subsequently, the Se nanowires layer was transferred onto the polymer stack through the above LB method. A second layer of PDMS was spin-coated onto the Se nanowires layer, then cured and treated with oxygen plasma before the deposition of the top Ag nanowires electrode. To complete the device fabrication, the uppermost PDMS layer was prepared with the same spin-coating method to encapsulate the whole device. The schematic of the final prepared device was shown in Figure 2.4.

Our Se-PENG device consists of multiple layers stacking of PDMS, Ag nanowires electrodes, and piezoelectric Se nanowires, which are highly flexible and stretchable. Figure 2.4 shows the good deformability of our Se-PENG device which can withstand large degrees of mechanical deformation without fracture or cleavage. A cross-sectional SEM image of the layered device is demonstrated in Figure 2.5, and we find that the interface of Se nanowires/PDMS and Ag nanowires/PDMS are clearly visible.

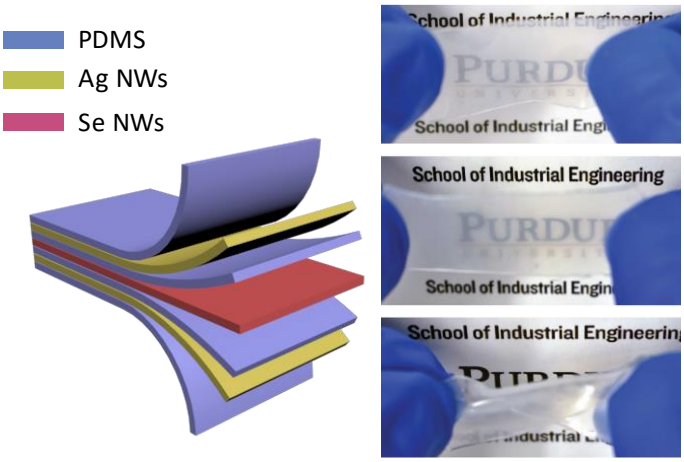

Figure 2.4 3D illustration of the Se-PENG device and the optical images of the device at the original state, being stretched and twisted, respectively.

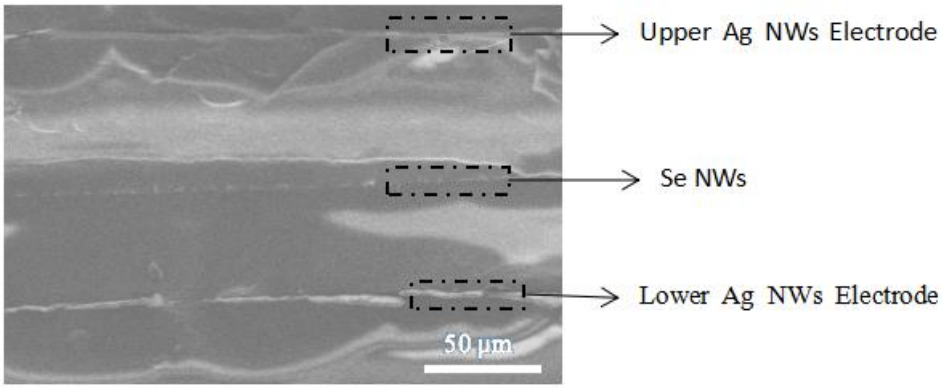

Figure 2.5 The cross-sectional SEM image of the piezoelectric nanodevice with layered structure.

2.2.5 Mechanical property of the Se-PENG device

To better quantitatively characterize the mechanical properties of the fabricated device, a tensile test is applied here (Figure 2.6), the tensile strength and the maximum strain of the device that can withstand are nearly 1.78 MPa and 200%, respectively. Here the PDMS layers not only serve as the insulating layers between the Se and Ag nanowires, but also encapsulate the Ag nanowires from oxidation and performance deterioration.

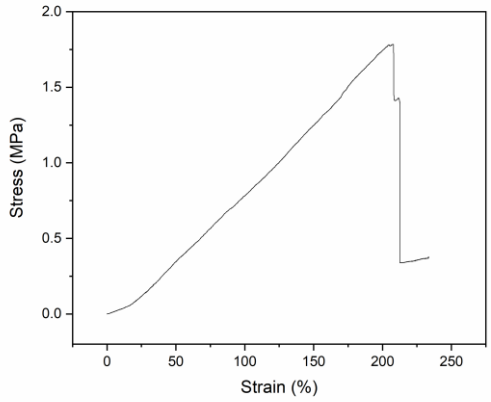

Figure 2.6 The stress-strain curve of the as-fabricated Se-PENG device.

2.2.6 Stability of the resistance change of the Se-PENG device

In our device, the sprayed Ag nanowires form an interconnected conducting network (Figure 2.7). The entanglement of these long Ag nanowires (lengths ~ 50-100 μm) is expected to lead to a good

conductivity and stretchability in the electrodes structure desirable for the PENG application[60]. We also characterized the reliability of our stretchable Ag nanowires electrodes by measuring their resistance after cyclic straining (Figure 2.8). A slight increase in electrode resistance was observed after the device being subjected to cyclic large-degree straining, and no observable increase in the electrode resistance can be seen after an initial "burn-in" period of 150-cycle straining. The increase in the Ag nanowire electrode resistance is negligible compared to the internal impedance of the PENG devices (from several hundred MΩ to GΩ)[61-63], and is expected to not affect the output of Se-PENG devices.

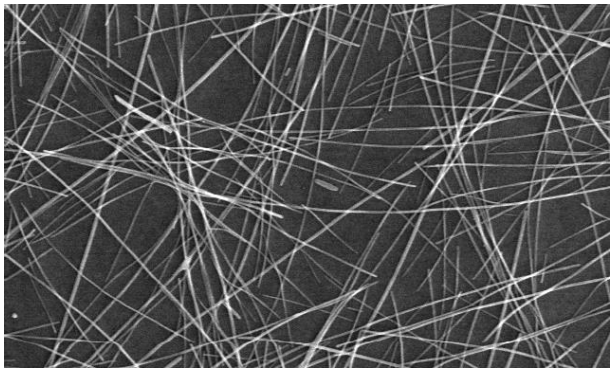

Figure 2.7 The SEM image of the Ag NWs network.

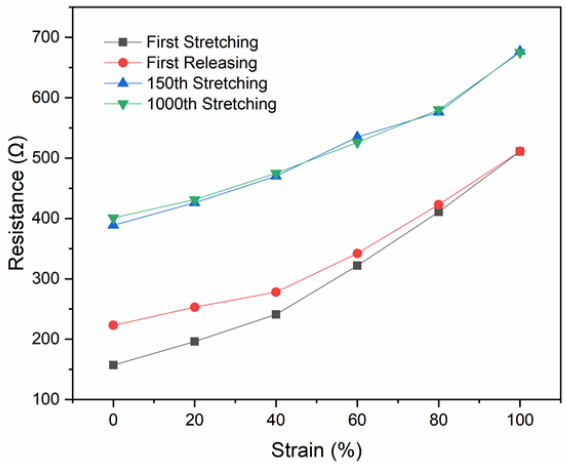

Figure 2.8 The resistance of Ag NWs electrode as a function of strain after different stretching-releasing cycles.

2.3 Characterization of the piezoelectric performance of the Se-PENG

2.3.1 Piezoelectricity origin analysis

The piezoelectricity origin can be analyzed from the crystal structure and point group of the material that belongs to. Trigonal selenium belongs to point group of 32, and the space group is either $P3_121$ or $P3_221$. The single crystal material belonging to group 32 do only have two independent piezoelectric components, d_{11} and d_{14}. The crystal structure of the selenium is demonstrated in Figure 2.1. Two adjacent Se atoms in one spiral are nearest neighbors and stronger bound than adjacent Se atoms of two neighboring spirals (Upper part in Figure 2.1). The hexagonal cross-section of the t-Se NW and its two-dimensional hexagonal-lattice structure with equilateral triangles resulting from the projection of the helical turns of Se atoms onto (0001) planes are illustrated in the lower part of Figure 1a. We draw a schematic here showing how the selenium atoms in one chain are distorted when they are subject to an external stress (Figure 2.9). We use a right-hand coordinate system x, y, z in which x, and z correspond to the crystallographic a- and c-axes, respectively. When a longitudinal stress is applied along the x-axis, an internal displacement of the Se atom and displacement of the electronic charge against the Se cores will occur, which would give rise to a piezoelectric polarization parallel to x axis. This polarization is described by the piezoelectric coefficient d_{11}. As presented in Figure 2.9(ii) and 2.9(iii), when the selenium nanowire is stretched vertically, a piezoelectric polarization pointing upward would be generated, and similarly a vertically compressed selenium nanowire would give rise to a downward-pointed piezoelectric polarization. As reported elsewhere, the piezoelectric components, d_{11} is found to be $(0.41 \pm 0.03) \times 10^{(-10)}$ m/V[64]. Although the piezoelectricity of selenium bulk crystal has already been reported in the prior work[56, 64-66], this is our first time to report the piezoelectricity in selenium nanowire and fabricate wearable devices for energy harvesting and sensor applications.

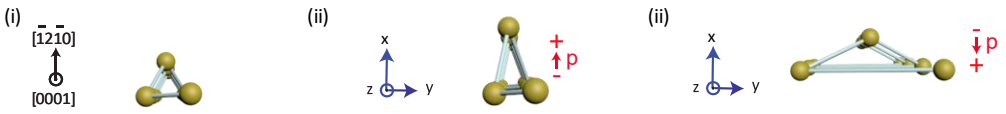

Figure 2.9 Schematic showing the deformed Se nanowire chain and the origin of the piezoelectric polarization.

2.3.2 Basic piezoelectricity characterization

Devices with a dimension of 1 cm × 2 cm was used in our experiment for characterizing the piezoelectric output of Se-PENGs. When the devices are subjected to periodic strains with controlled magnitudes, which are applied through a linear motor, the strain-induced piezoelectric polarizations in the Se nanowires will electrostatically induce an electrical field between the top and bottom electrodes. Such a time-variant piezoelectric field due to the periodic strain leads to the displacement current in the circuit and hence the measured electrical outputs[5]. With a compressive strain of 0.74% along the alignment direction of Se nanowires, the measured open-circuit voltage (V_{oc}) and short-circuit current (I_{sc}) present to be 0.45 V and 1.67 nA, respectively (Figures 2.10(a) and 2.10(b)).

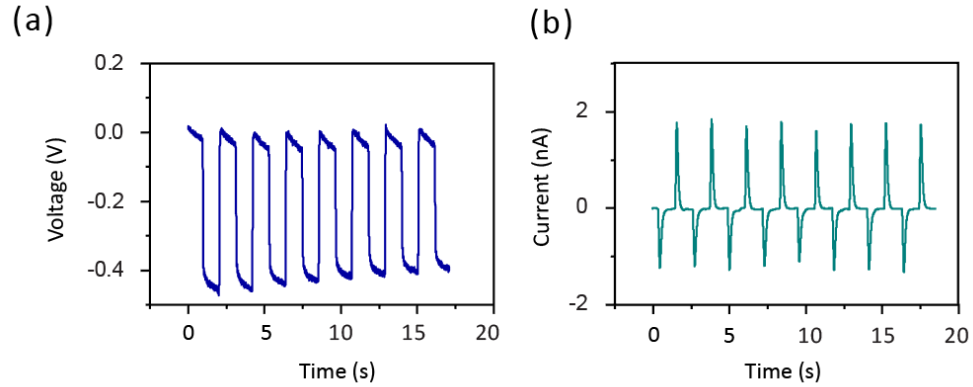

Figure 2.10 (a) open-circuit voltage (V_{oc}) and (b) short-circuit current (I_{sc}) of Se-PENGs.

2.3.3 Validation of the piezoelectricity

The switching-polarity test was further performed to verify that the measured electrical outputs are caused by the intrinsic piezoelectric properties of the assembled Se nanowires[67] (Figure 2.11). Additional sets of characterizations were also carried out when the Se-PENGs were subjected to a tensile strain along the alignment direction of Se, showing that the electric outputs were reversed when the strain was switched from compressive to tensile.

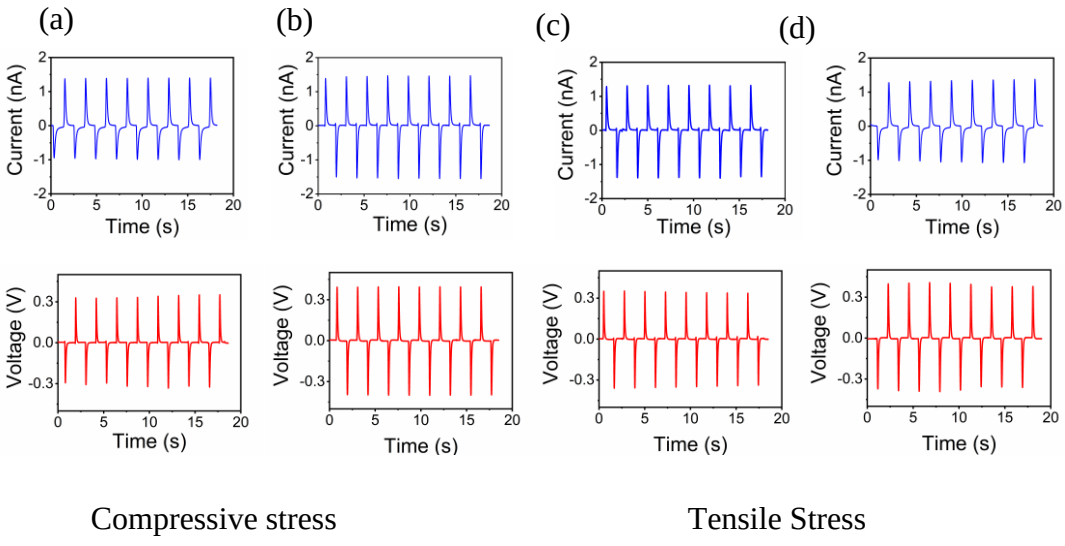

Figure 2.11 (a) Electric outputs when the NG devices are under (a)(b) compressive stress and (c)(d) tensile stress periodically. Devices are forwardly connected in (a)(c), and reversely connected in (b)(d), indicating that the output signals are based on piezoelectric response.

2.3.4 Piezoelectric output as a function of the applied strain

The strain-dependent piezoelectric outputs were also characterized for the Se-PENG devices when the strain increased from 0.74% to 2.59% (Figure 2.12). Both the V_{oc} and I_{sc} increase with the strain. The monotonic dependence of the piezoelectric outputs with the magnitudes of the applied strains suggest that the Se-PENG has a good strain resolution and can function as a self-powered mechanical sensor[68]. The small variance seen for each data point in Figure 2.12 is likely due to the variations in the electrode resistance.

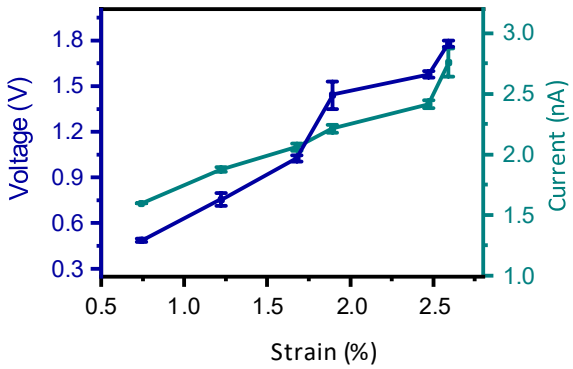

Figure 2.12 The V_{oc} and I_{sc} of the Se-PENG as a function of applied strain.

2.3.5 Piezoelectricity output as a function of the active Se layers

The unique crystal structure of Se nanowires and the corresponding radial distribution of the piezoelectric field in strained Se nanowires facilitates the integration of multiple Se-PENGs into ultrathin laminated devices with enhanced outputs. Figures 2.13(a) and (b) show that both the output voltage and current increase when the assembled Se layers scale up. Here the number of selenium nanowire layers can be controlled by the assembly and the following transfer times to the substrate.

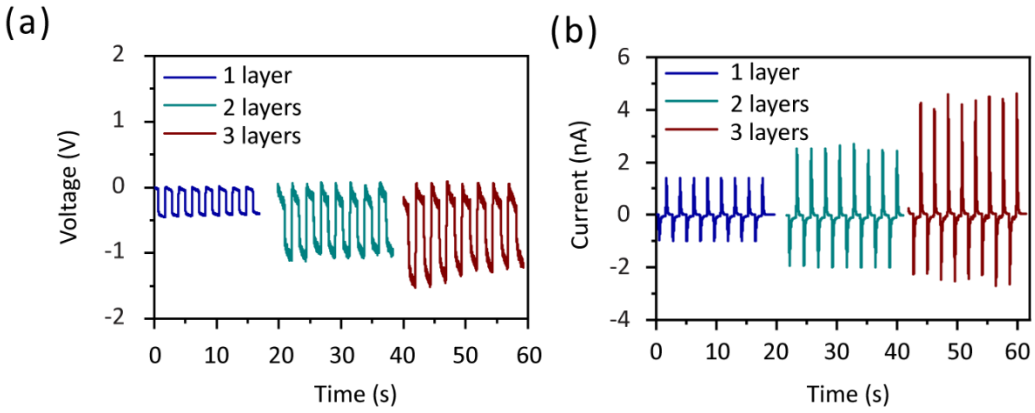

Figure 2.13 The piezoelectric output (a) voltage and (b) current from devices with 1, 2 and 3 layers of assembled Se nanowires.

2.3.6 Power output of the Se-PENG device

The output power of Se-PENG delivered to external loads is characterized by varying the load resistance connected in the circuit. Figure 2.14 shows the resistance-dependent output voltage and current when the load resistor was swept from 100Ω to 1.88 GΩ. The instantaneous output power can then be calculated and plotted as a function of the load resistance, with a maximum output power determined to be 0.135 nW/cm^2 at a load resistance of 1 GΩ.

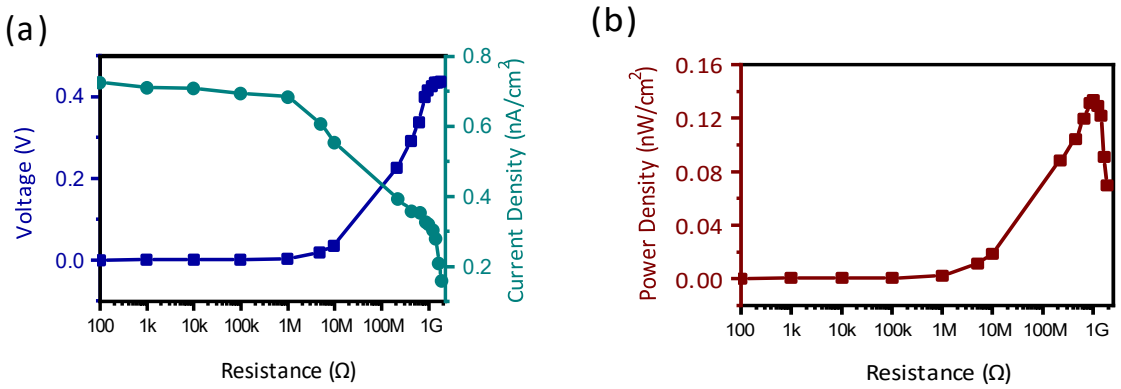

Figure 2.14 The (a) output voltage/current and (b) power of Se-PENG device versus the load resistance.

2.3.7 Stability of the device

Taking advantage of the superior mechanical deformability and stability of the Se nanowire active layer, the Ag nanowires electrodes, and the PDMS layer, Se-PENG shows good long-term stability after being subjected to cyclic straining and release for a period of more than two hours (Figures 2.15). And also, the morphology of the Se NW encapsulated in the PDMS are not seriously affected after repeated large deformation and recovery of the device (Figure 2.16).

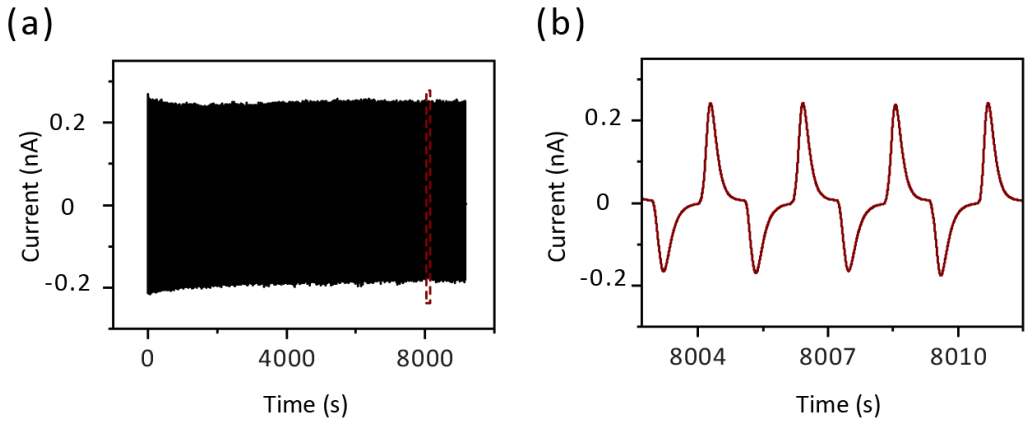

Figure 2.15 The cyclic output of Se-PEND during a stability test. (a) The magnified view of the output signals highlighted in (b). Only one layer of Se nanowires is adopted in the device and the applied mechanical strain is 0.74% for the measurement.

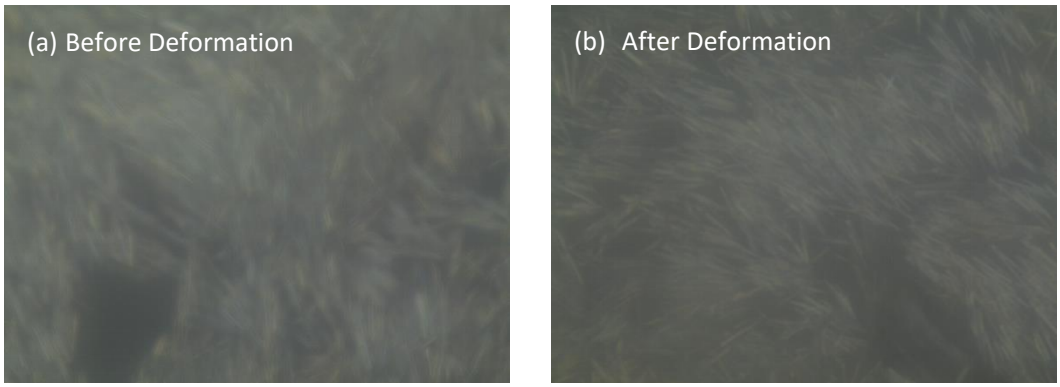

Figure 2.16 The optical images of the Se nanowires encapsulated in the PDMS (a) before and (b) after large deformation.

2.4 Self-powered human-integrated application of the Se-PENG

Finally, we explore the feasibility of Se-PENG device for potential self-powered human-integrated applications, e.g., gesture recognition and cardiovascular monitoring. The wearable Se-PENG device can be attached to different parts of human body compliable with minimum deformation. Figure 2.17 shows the application of the Se-PENG device attached to the joint of a finger for detecting and recognizing the finger movement[69]. During the test, the finger was bent to different degrees, and the corresponding outputs were recorded. A larger bending angle gives rise to a stronger piezoelectric output. The Se-PENG device can also be attached to the throat for identifying different vocal activities, e.g., coughing, gargling, and swallowing (Figure 2.18). Furthermore, the Se-PENG device can be used to sense the radial artery pulses in real-time (Figure 2.19). The device was attached to the wrist of a healthy 24-year-old male for the non-invasive detection of pulse without using an external power source. The real-time piezoelectric current output from the device for 30 s shows the reliable detection and measurement of the human pulse signals, with distinct three-peak characteristics for the cardiac cycle (Figure 2.19). Such a pattern is consistent with the reported results[70-71], and manifests important information for the health diagnostics. Here we attempted to analyze the acquired signals. Three distinguishable determinants could be obtained from one typical pulse cycle[72-74]: namely, early systolic peak pressure ($P_1(t_1)$: percussion wave (P-wave)), late systolic augmentation shoulder ($P_2(t_2)$: tidal wave (T-wave)), and diastolic pulse waveform ($P_3(t_3)$: diastolic wave (D-wave)). These peaks can be used to quantify the augmentation index ($AI_r = P_2/P_1$) and the time delay between the first and second peaks

($\triangle t = t_2 - t_1$), which provide valuable information for evaluating the physiological conditions of the human cardiovascular system[73-75]. The calculated AI_r and $\triangle t$ using Se-PENG are 0.57 and 0.26 s, respectively, which fall in a normal and healthy range[73-75]. The demonstrated self-powered sensing capability to detect the small-scale biomechanical signals from the human body, together with the facile and low-cost fabrication process, can potentially lead to broader applications of our devices for wearable self-powered biomedical devices.

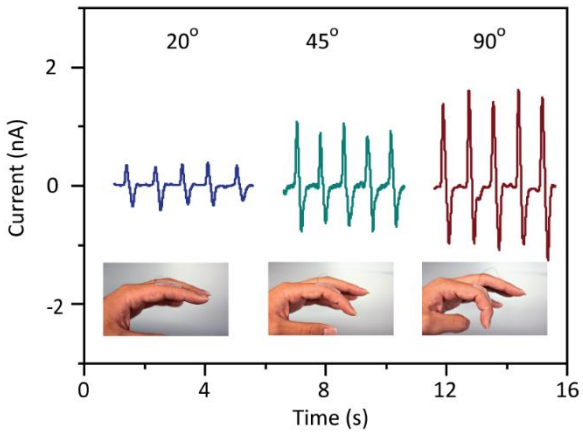

Figure 2.17 The output current of the NG attached on the human fingers and bent with different angles.

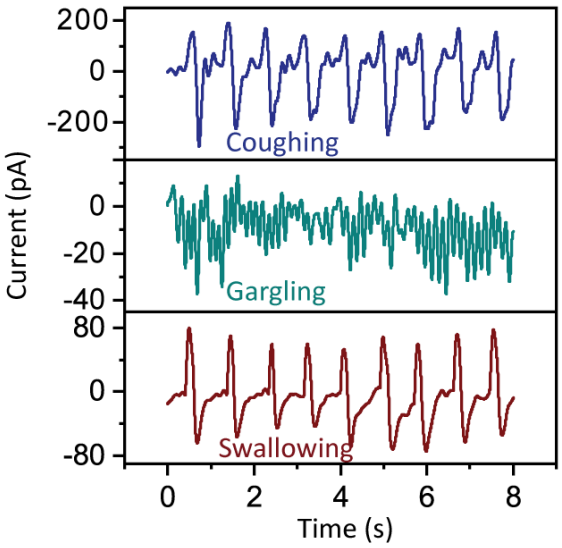

Figure 2.18 The output current of the Se-PENG attached on the human throat when the subject is coughing, gargling and swallowing.

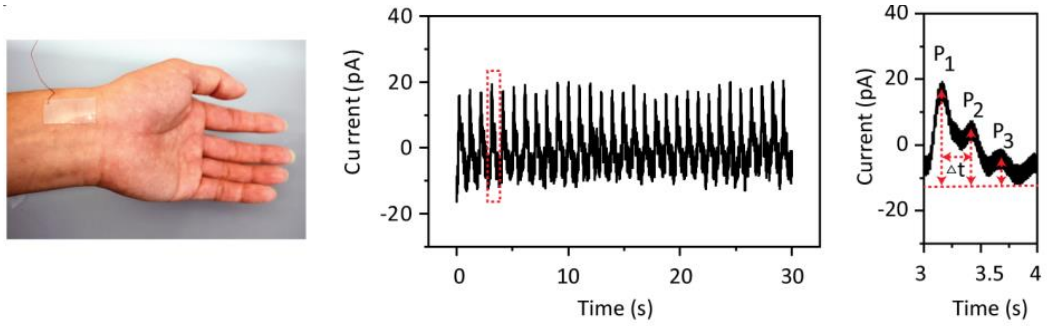

Figure 2.19 The real-time artery pulse signal monitored by the Se-PENG.

2.5 Conclusion

In summary, Se nanowires synthesized by a hydrothermal method are explored as a new class of piezoelectric nanomaterial. The assembled Se nanowires by an LB approach are integrated into a wearable piezoelectric device for PENG application and sensing the small-scale biomechanical signals from the human body. A monolayer of assembled Se film can generate a V_{oc} and I_{sc} up to 0.45 V and 1.7 nA, respectively, when being subjected to a strain of 0.75%, with the maximum power density ~ 0.135 nW/cm^2. The performance and efficiency of such Se-PENG can be optimized by scaling up the number of the active Se layer through the integration of laminated devices. The Se-PENG demonstrated here shows great potential for self-powered biomedical devices, and opens doors to new technologies in energy, electronics, and sensor applications.

3. 3D PRINTING OF FUNCTIONAL PIEZOELECTRIC DEVICE WITH CHIRAL CHAIN VAN DER WAALS NANOMATERIALS FOR WEARABLE ENERGY DEVICES AND SENSORS

3.1 Introduction

Recently, piezoelectric nanogenerators (PENGs), first reported by Wang's group[1], which can generate electricity when subject to an external strain, have emerged as a new paradigm for harvesting mechanical energy from human body motions and monitoring physiological activities[47, 68]. PENGs are generally composed of multiple independent layers, including one piezoelectric sensing layer and two end electrodes. Currently, a variety of materials endowed with piezoelectric properties have been found and applied in the PENGs[24, 27, 33, 39], and also many efforts are paid on boosting the device's piezoelectric performance[38, 41-42], or enhancing the device's flexibility and stretchability to adapt them to wearable electronics[47, 62, 76]. However, the complex structures and thus sequential assembly steps make it challenging to achieve scalable fabrication, which is highly desired for emerging wearable electronic devices.

Nowadays, 3D-printing has been recognized as a revolutionary manufacturing technology and received significant attention from both industry and academia[77]. This computer-aided additive manufacturing technology can readily customize complex 3D geometries with well controlled micro- and macrostructure from diverse materials. Due to its clear advantages, 3D-printing has been widely used in the manufacturing of a variety of electronic and biomedical devices[78-80]. Among the various 3D-prininting method, direct ink writing (DIW), which count on extruding the filament directly through a nozzle by a patterned path and then forming a free-standing 3D structure in a layer-by-layer sequence, have attracted much attention due to its economy and feasibility[11]. Lately, Bodkhe et al reported the DIW of piezoelectric polyvinylidene fluoride (PVDF) nanocomposite structures. In their study, a layer-by-layer and self-supporting piezoelectric structure is realized by a solvent evaporation-assisted 3D printing approach[81]. However, the whole process consists of multiples steps, in which the piezoelectric sensing layer and electrode layers are prepared separately, and further assembly and integration procedures are still inevitable. As such the realization of large-scale fabrication of PENG devices is still greatly limited.

To address the aforementioned challenges in PENGs, we develop a simple, scalable, and facile strategy to fabricate PENG devices. Hereby in our experiment, SE 1700 PDMS is blended with tellurium (Te) nanowires, and the composite is endowed with piezoelectric property due the inherent piezoelectricity of Te nanowires. The rheological property of Te/PDMS composite is carefully tuned to make it suitable for 3D-printing. Carbon grease (CG) is selected as the electrode layer as we consider its conductivity, printability, and flexibility. The entire layered structure is composed of one central sensing layer, i.e., Te/PDMS composite, and two CG electrode which are closely attached on the top and bottom of the layer of Te/PDMS. The whole device can be readily fabricated in one-step DIW process without further assembling procedure. The resultant 3D printed PENG has a layered structure, which is hardly achieved through traditional molding method. Based on the 3D-printing technologies, the new developed PENG devices can be processed into variable 3D shapes to meet different requirements or serve in diverse environment, especially useful for wearable electronics. The PENG device can effectively generate electricity when it is applied with a periodic strain by repetitive stretching and releasing process. Furthermore, the whole device shows good transformability and can be attached to the wrist of human body, to work as a sensor to sense different gestures. Results reveal that the PENG-based sensor are eligible to deliver different waveforms of piezoelectric signal when stimulated by various strain generated from movement of flexor tendons. Combined with the machine learning approach, the 3D printed PENG can effectively discern the movement of different fingers, indicating its promising applications in gesture recognition for remote sensing and controlling.

3.2 Materials synthesis and device fabrication

3.2.1 Te nanowires synthesis

Te NWs was synthesized based on a previously reported way, while a few parameters have been adjusted in our experiments[82]. Specifically, 0.0922 g Na_2TeO_3, 1g poly(vinly pyrrolidone) (M.W. = 58000) were dissolved in 33 ml DI water/Ethylene Glycol mixture (50%/50% w/w%), 3.35 ml aqueous ammonia solution (25%-28%, w/w%) and 1.65 hydrazine hydrate (80%, w/w%) were then added to form a homogeneous solution. After that, the solution was transferred into a 50 ml Teflon-lined stainless-steel autoclave and maintained at a temperature of 180 ^oC for 4 hours to complete the reaction. After the reaction, the autoclave was taken out and rapidly cooled by water.

3.2.2 Te nanowires characterization

The morphology of the Te NWs was identified by a field-emission scanning electron microscope (Hitachi S-4800 Field Emission SEM). XRD measurement was carried out using a Bruker AXS D8 Advance X-ray diffractometer equipped with a LynxEye 1-dimensional linear Si strip detector. High-resolution STEM/TEM imaging and SAED has been performed using a probe-corrected JEM-ARM 200F (JEOL USA, Inc.) operated at 200 kV.

Here the methods taken for the synthesis of Te nanowires are mainly adopted from the previous reports while a slight variation is included[82]. Detailed methods are depicted in the experimental section. As presented in Figure 3.1, Te nanowires are composed of a series of helical chains which are stacked together by van der Waals (vdW) force. In each chain, every Te atom is connected by two neighboring atoms via covalent bonds by a degree of 120^{o} and thus a periodic chain is formed accordingly. Figure 3.1(b) is the projection of Te atoms from the viewpoint along c axis. Figure 3.2-3.4 are the characterization results, including X-ray diffraction (XRD), scanning electron microscopy (SEM), transmission electron microscopy (TEM) of our as-synthesized Te nanowires. XRD results obtained from Figure 3.2 agree well with the powder diffraction file of trigonal Te (#36-1452), which confirms the perfect crystalline structure of our synthesized products. SEM images of Te nanowires (Figure 3.3) exhibit that the Te NWs products are quite uniform with a diameter of ~ 1 μm and a length of approximately 20 μm. Further TEM results in Figure 3.4 also demonstrate the crystal nature of as-synthesized products, the value of 0.59 nm corresponds well to the spacing of (0001) planes. Figure 3.4(b) is the selected-area electron-diffraction (SAED) pattern taken along the $[10\bar{1}0]$ axis. The combination of these characterization results would be strong evidence to prove the good purity and crystallinity of our synthesized trigonal Te nanowires.

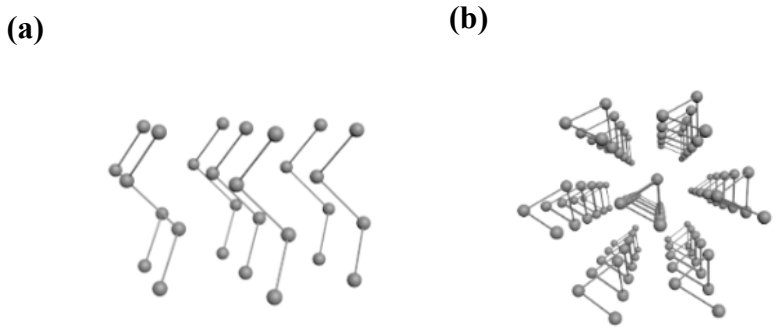

Figure 3.1 Schematic of the crystal structure of Te nanowires.

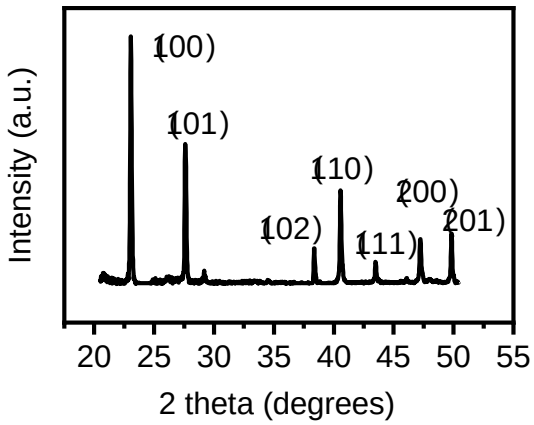

Figure 3.2 XRD patterns of the as-synthesized Te nanowires.

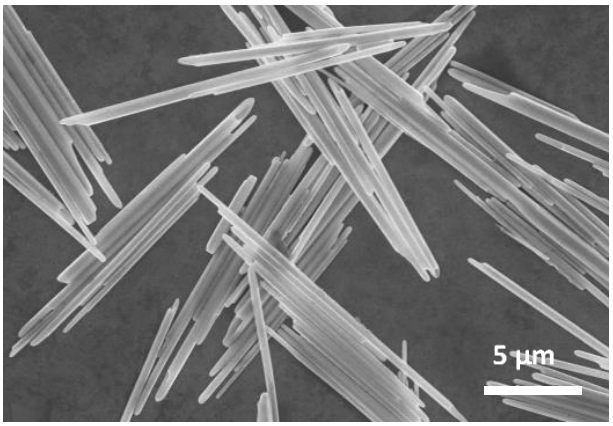

Figure 3.3 SEM images of the as-synthesized Te nanowires.

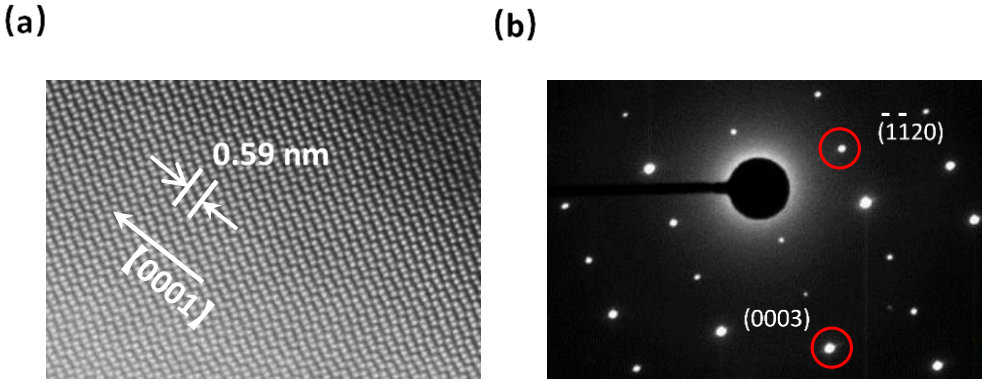

Figure 3.4 (a) TEM images and (b) SAED patterns of the as-synthesized Te nanowires.

3.2.3 Inks preparation and rheological properties characterization

The synthesized Te nanowires are firstly blended into the PDMS matrix to form a highly viscous ink for the further 3D-printing procedure. The detailed steps of ink preparation are described as follows. Firstly, the Te nanowires products in the suspensions were precipitated by centrifugation at 5,000 r.p.m for 5 min and washed for three times with distilled water. 1 ml DI water was then added to dissolve the products. The concentrated solution was blended with 6 g PDMS (SE 1700, Dow Corning) by constant stirring to form a composite ink. To enable a successful DIW with prepared ink, the rheological behaviors of Te/PDMS composite are firstly characterized. Rheological properties of the composite ink were measured using a rheometer (Anton Paar MCR 302) with a 40-mm-flate plate geometry a gap of 500 μm. A stress sweep from 10^{-1} to 10^{3} Pa at constant frequency of 1Hz was conducted to record the storage and loss modulus variations as function of weep stress. The yield stress (τ_y) was defined as the stress where storage modulus falls to 90% of the plateau value. A strain sweep from 10^{-1} to 10^{2} s^{-1} was also performed to record the apparent viscosity at varying shear rates. Figure 3.5(a) displays that the viscosity of our prepared ink decreases with the shear rate, which is a typical shear-thinning non-Newtonian fluid behavior[83]. This ensures that the ink can be extruded from the nozzle in a continuous flow and a clogging is avoided. In Figure 3.5(b), the magnitude of storage modulus (G') and loss modulus (G'') are compared when the shear stress is ranged from 0.01 to 1000 Pa. Specifically, the Te/PDMS composite ink shows plateau values of a storage modulus of ~ 40000 Pa, and a loss modulus of ~ 10000 Pa. The phenomenon that G' plateau exceeding G'' plateau across a wide shear stress range conveys the information that the extruded ink from nozzle would maintain a solid structure, and the prior printed layer would be strong enough to support the subsequent printing layer[11, 83-84].

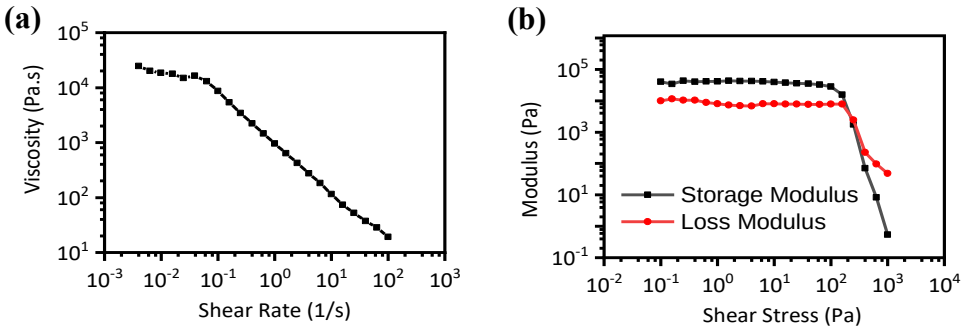

Figure 3.5 Rheological property of the Te/PDMS ink.

3.2.4 Process of 3D printing for device fabrication

The additive manufacturing technique, which is the so-called 3D printing, was applied here to directly fabricate a piezoelectric device with our desired shape, equipment taken in our experiment is Cellink Bioprinter (Inkredible +). The as-prepared Te/PDMS composite ink was loaded into a 3 ml syringe, which is able to be extruded out through the nozzle by an air pressure exerted by mechanical pump. Another syringe loaded with carbon grease was applied to print electrodes for the device. By designing the CAD pattern and editing the corresponding G-code, a dual-head printing technique was successfully adopted to print a device. Figure 3.6 presents the schematic process of the ink preparation and device preparation. Firstly, the synthesized Te are blended with the PDMS to form a viscous composite, the so-called Te/PDMS. Then the composite was transferred into a syringe for the further piezoelectric layer printing. Another syringe loaded with CG is also ready for the electrode layer printing. The two syringes are then mounted into a 3D printer, and their movement are carefully controlled by a customized G-code. As the two syringes move along a designed trace, Te/PDMS ink composite ink and CG ink are extruded from the nozzle by a pressure brought from a mechanical pump, in such a way, the extrude ink will lay down on the substrate and stack into a pre-planned structure in a layer-by-layer sequence. The printed device was then transferred into an oven and heated in an environment of 80 ^{o}C for several hours for solidification.

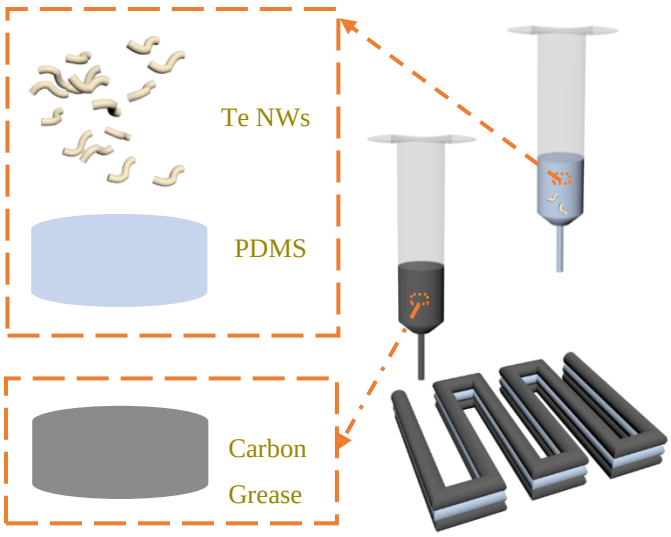

Figure 3.6 Schematics of the ink preparation and 3D-printing process for the piezoelectric devices fabrication.

Photographs in Figure 3.7 demonstrate the printing process for our piezoelectric nanogenerator (NG) device. Figure 3.7-i shows the equipment setup, firstly a layer of CG is directly written on the substrate (Figure 3.7-ii), then several layers of Te/PDMS composite ink are directly printed on top of the CG layer (Figure 3.7-iii), after that an another CG layer is written on the Te/PDMS layer (Figure 3.7-iv), finally the printed device is carefully transferred to an atmosphere of 80 ℃ to make it solidify, hereby a complete device is fabricated. The printed Te/PDMS composite here serves as the piezoelectric layer, detailed illustration of its piezoelectric origin and performance are discussed in the latter part. Carbon grease (CG) is selected as the electrode layer for the whole NG device as we consider its conductivity, stretchability, and printability. It has already been reported elsewhere that the CG can work as a good electrode layer for the 3D-printed devices[85]. The final device photography is presented in Figure 3.8, the as-obtained device is composed of three layers, namely a piezoelectric layer of Te/PDMS (Grey one) sandwiched by two CG layers (Black ones), and it can be found that the interfaces between CG layer and Te/PDMS layer are clearly visible. The CG layers here serve as electrodes for the further characterization of the device's piezoelectric properties.

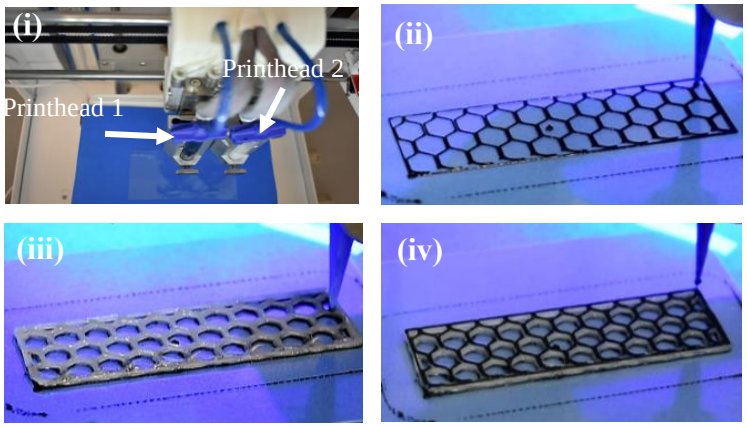

Figure 3.7 Photographs demonstrating the different stages of 3D-printing process.

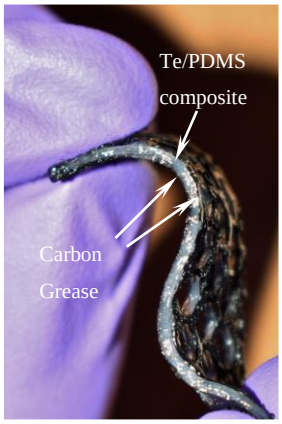

Figure 3.8 Photographs of the fabricated PENG device via 3D-printing.

3.3 Mechanical properties characterization of the 3D printed device

3.3.1 3D printing of device with different structures

By adjusting the CAD pattern and corresponding G codes, a variety of devices with different morphologies and 3D shapes can be made via 3D printer. In Figure 3.9(a) we designed four different porous and layered structures for our piezoelectric devices which can be realized by the DIW technique. Photographs in Figure 3.9(b) demonstrate the four printed devices, which are with a honeycomb structure, lattice structure, mesh structure and solid structure, respectively. The lengths and the thickness of all these four devices are 36 mm and 1 mm, respectively. The wall widths (w) of the honeycomb, lattice and mesh structures are 1mm as shown in the figure. This demonstration confirms that 3D printing technique would offer us a great many of possibilities to fabricate devices with our desired shapes, and further adapt them to different situations.

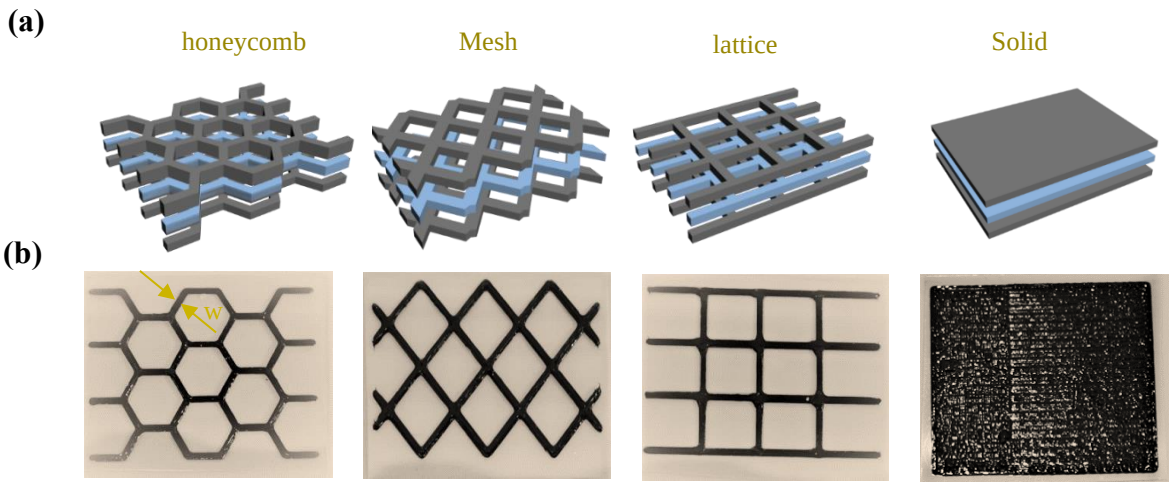

Figure 3.9 (a) schematic showing the designed porous and layered structure of the 3D printed device. (b) Photographs of the devices with four different patterns fabricated via 3D-printing.

3.3.2 Mechanical properties of the printed device with different structures

These porous structures are known to be particularly useful for enhancing the mechanical properties of stretchable devices, because the deformation of pores effectively mitigates the strains of the overall devices[86]. Finite Element Analysis (FEA) is carried out to assess the local strain distribution when devices with different patterns are stretched by a deformation of 50%. The details of FEA models of these devices in uniaxial tension are illustrated here. The commercially available FEA software Abaqus 6.10 (Dassault Systems, Waltham, MA, USA) was used to evaluate the strain distributions in porous device in uniaxial tension. In view of the highly elastic nature of, a second order Ogden hyperelastic material model was used to calculate the strains. The size of elemental meshes was set at 0.02 mm using a two-dimensional, four-node bilinear stress quadrilateral, reduced integration, hourglass control (CPS4R) element type. About 150,000 elements were used. All composite device share the same boundary conditions, namely the left edge was fixed, and a 50% tensile strain was applied on the right edge. Figure 3.10 gives the simulation results of strain distribution for these four different structures under 50% overall engineering strain. Obviously, in this case most regions in the honeycomb and mesh structures are subjected to a relatively small local strains as compared to the solid structure, which would result in less possibility of being snapped. As for the lattice structure, the lines along the stretch direction sustain a strain nearly 50%, while the lines which are vertical to the stretching direction are subjected a trivial strain.

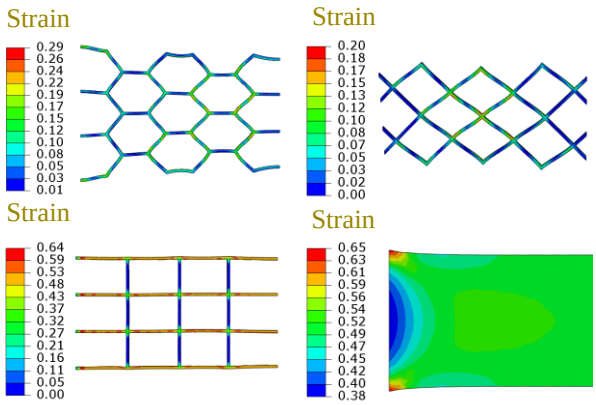

Figure 3.10 Simulation of local strain distributions in the four devices when being stretched by 50%.

The tensile test was conducted on a universal test machine (MTS) with a at a loading rate of 60 mm/min. The tensile nominal stress (σ) was obtained through dividing the force (F) by the cross-sectional area (A). The tensile strain (Ɛ) was obtained through dividing stretched length (△l) by the original length (l_0). Figure 3.11 presents the stress-strain curves for the four structures, it is noted here that the stress-strain relations are almost always keeping linear until final structure ruptures. A few slight fluctuations in the curve can be noticed, these are attributed to the emerging and extending of those small cracks and voids in the device when being stretched. The maximum tensile strains that the honeycomb, mesh, lattice, and solid structures can withstand are 200%, 256%, 130% and 131%, respectively, which agree well with our expectations and simulation results. Young's modulus for the honeycomb, lattice, mesh, and solid structures are calculated to be approximately 0.49, 0.43, 2.62, and 2.61 MPa, respectively, further proves that the porous structures can be stretched by a smaller force. This characteristic is very critical to the wearable devices, as in most cases the devices are subject to a large strain with the movement of human body, so a high flexibility and stretchability is anticipated[87].

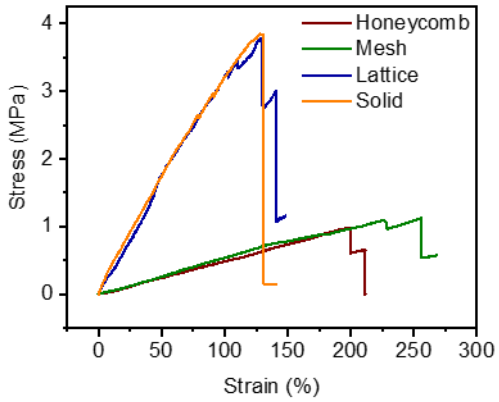

Figure 3.11 Stress-strain curve of the four afore-mentioned devices when being stretched until fracture.

3.4 Characterization of the piezoelectric performance of the printed device

3.4.1 Shear alignment of Te nanowires in the PDMS matrix during the extrusion-based process

The piezoelectric properties of printed devices are characterized in Figure 3.12. For our prepared ink, the Te nanowires are uniformly blended in the PDMS matrix, and when the composite ink is extruded from the nozzle, a shear force will impact on the Te NWs, thereby the NWs would preferentially align horizontally in the PDMS matrix, which is demonstrated in the schematic of Figure 3.12. The preferred orientation of Te nanowires in the PDMS matrix is confirmed by optical images. A solid layer of Te/PDMS is solely printed without the presence of the two CG layers to help us view the distribution of Te nanowires in the PDMS matrix (Figure 3.13). It can be found that the Te nanowires are distributed in the PDMS matrix in a horizontally way, which provide the possibility for the further exhibition of piezoelectric performance. Figure 3.13 also reveals that the distribution of Te nanowires in the PDMS matrix becomes denser when the fill up ratio increases from 2% to 8%.

Figure 3.12 Schematic showing the extrusion of Te/PDMS composite from nozzle and shear-force induced alignment process.

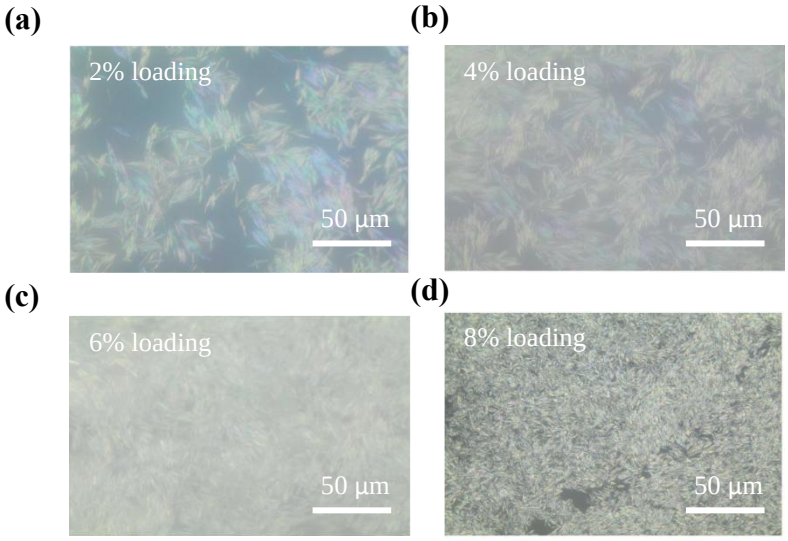

Figure 3.13 Optical images showing the distribution of Te nanowires with different concentrations in the PDMS matrix.

3.4.2 Electrode resistance measurement of the device

We firstly characterized the reliability of our stretchable CG electrodes by measuring their resistance after cyclic straining (Figure 3.14). The device we take for measurement here is the one with the honeycomb structure. A slight increase in electrode resistance was observed after the device being subjected to cyclic large-degree straining, and no observable increase in the electrode resistance can be seen after an initial “burn-in” period of 150-cycle straining. The increase in the CG electrode resistance is negligible compared to the internal impedance of the PENG devices

(from several hundred MΩ to GΩ)[61-63], and is expected to not affect the output of 3D printed PENG devices.

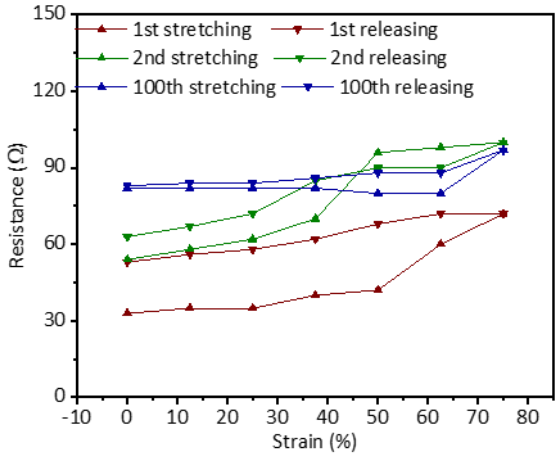

Figure 3.14 The resistance of the carbon grease electrode after being stretched for a couple of times.

3.4.3 Origin analysis of the piezoelectricity from Te nanowires and the working principle of the device

The inherent piezoelectric property of Te nanowires have already been demonstrated in previous works[52, 88]. The piezoelectricity origin can be analyzed from the crystal structure and point group of the material that belongs to. Trigonal Te belongs to point group of 32, and the space group is either $P3_121$ or $P3_221$. The single crystal material belonging to group 32 do only have two independent piezoelectric components, d_{11} and d_{14}. The crystal structure of Te nanowire is demonstrated in Figure 3.1. Two adjacent Te atoms in one spiral are nearest neighbors and stronger bound than adjacent Te atoms of two neighboring spirals (Figure 3.1). The hexagonal cross-section of the t-Te nanowire and its two-dimensional hexagonal-lattice structure with equilateral triangles resulting from the projection of the helical turns of Te atoms onto (0001) planes are illustrated in Figure 3.1(b). We draw a schematic here showing how the Te atoms in one chain are distorted when they are subject to an external stress (Figure 3.15). We use a right-hand coordinate system x, y, z in which x, and z correspond to the crystallographic a- and c-axes, respectively. When a longitudinal stress is applied along the x-axis, an internal displacement of the Te atom and displacement of the electronic charge against the Te cores will occur, which would give rise to a piezoelectric polarization parallel to x axis. This polarization is described by the piezoelectric coefficient d_{11}. As presented in Figure 3.15(ii) and 3.15(iii), when the Te nanowire is stretched

along its radial direction, a piezoelectric polarization pointing upward would be generated, and similarly a compressed Te nanowire would give rise to a downward-pointed piezoelectric polarization. As the piezoelectric polarization direction of Te nanowires are along their radial direction, thus when these nanowires are horizontally distributed in the PDMS matrix and subsequently the Te/PDMS composite is subject to an external strain, there will induce an piezoelectricity at the top and bottom electrodes, just like the case of piezoelectric $BaTiO_3$/PDMS composite from other research report[89].

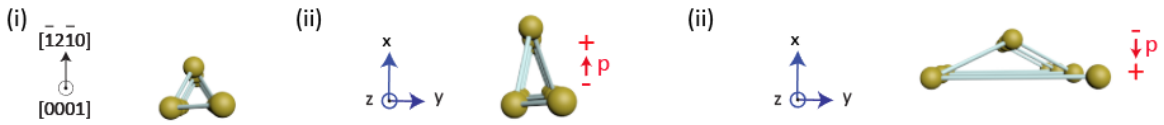

Figure 3.15 Analysis of the piezoelectricity origin of the horizontally aligned Te nanowires upon compression or stretching.

When the devices are subjected to periodic strains with controlled magnitudes, which are applied through a linear motor, the strain-induced piezoelectric polarizations in the Te nanowires will electrostatically induce an electrical field between the top and bottom electrodes. The I-t and V-t characteristics were measured by a low-noise current preamplifier (model No.SR570, Stanford Research Systems, Inc.) and an electrometer (Keithley 6514). A linear motor (LinMot PS01-23 × 80) was used for applying programmed strain inputs. A potential difference between the top and bottom electrodes causes the flow of piezoelectric potential-driven electrons from one electrode to another through an external load resistor. With releasing of the strain, the piezoelectric potential immediately vanished and the electrons accumulated near the electrode flow back to the other electrode through the external circuit, leading to an electric signal in opposite direction. Such a time-variant piezoelectric field due to the periodic strain leads to the displacement current in the circuit and hence the measured electrical outputs[5], as shown in Figure 3.16.

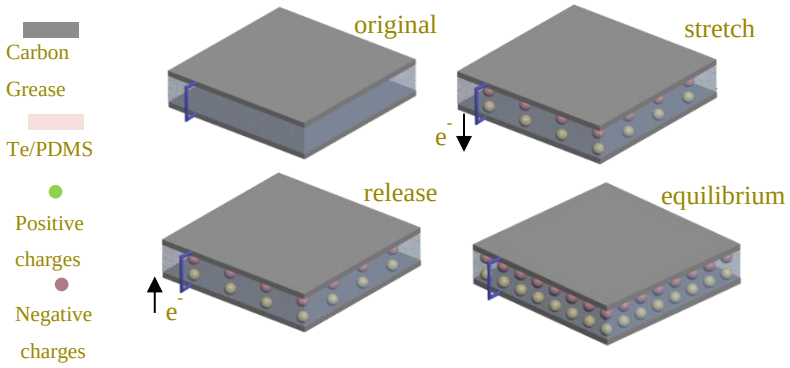

Figure 3.16 Schematic showing the working principle of our 3D printed device.

3.4.4 Basic characterization of the piezoelectric output

The voltage and current outputs of the device with different Te nanowires loading under periodic stretch and release are recorded as Figure 3.17. Under a stretch ratio of 12.5 %, the device with 2% Te nanowires loading would output an open-circuit voltage (V_{oc}) of nearly 1 V and a short-circuit current (I_{sc}) of nearly 2 nA, respectively, and alternatively negative and positive peaks of voltage signals as well as current signals are observed. The relationship between the Te nanowires concentration and its output performance was studied, and the results are shown in Figure 3.17. Output voltages around 1, 1.6, 2.1, 2.3 V from the 3D printed PENG, for Te nanowires fractions of 2, 4, 6 and 8 wt. %, respectively, could be obtained (Figure 3.17(a)). Similar to Figure 3.17(a), a difference of current peak values about 2, 3, 4, 4.2 nA could be observed when the concentration of Te nanowires proportionally increased from 2 wt.% to 8 wt.% (Figure 3.17(b)). It can be explained by the fact that the Te nanowires are well distributed in PDMS matrix except for slight agglomeration and the density of Te nanowires becomes larger with the rising concentration, which leads to an enhanced piezoelectric output accordingly.

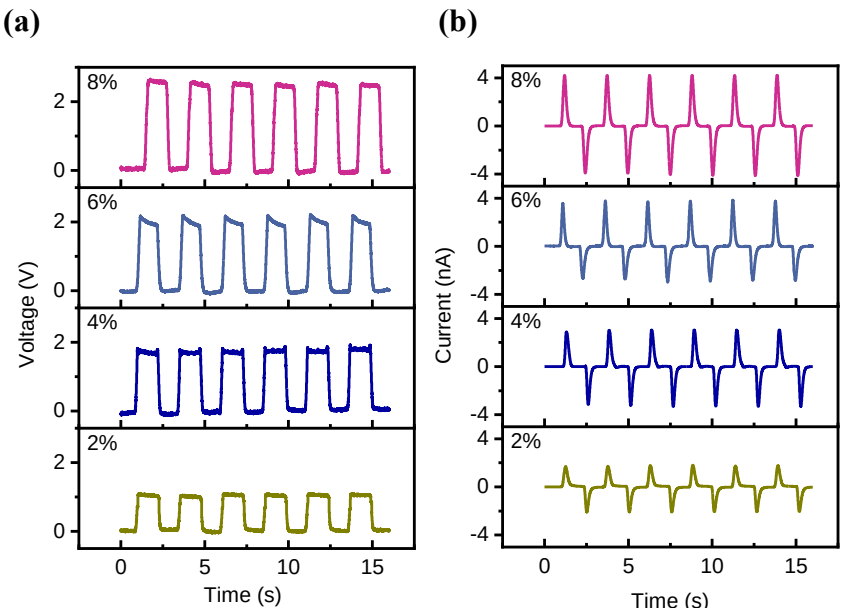

Figure 3.17 Open-circuit voltage (Voc) and (d) short-circuit current (Isc) of NG device with different concentration of Te nanowires in the PDMS matrix. Device taken for the measurement is the one with honeycomb structure, and the applied strain is 12.5%.

3.4.5 3.4.5 Validation of the piezoelectricity origin

The switching-polarity test was further performed to verify that the measured electrical outputs are caused by the intrinsic piezoelectric properties of the Te/PDMS composite (Figure 3.18). The output performance of the printed device fabricated by DIW of the PDMS matrix without the addition of Te nanowires is also measured. As shown in Figure 3.19, there is no reliable signal generated from the printed device containing only pure PDMS. The low electrical signals, which are presumably caused by several electrostatic charges at the electrodes, can be ignored in comparison with the device after Te nanowires incorporation.

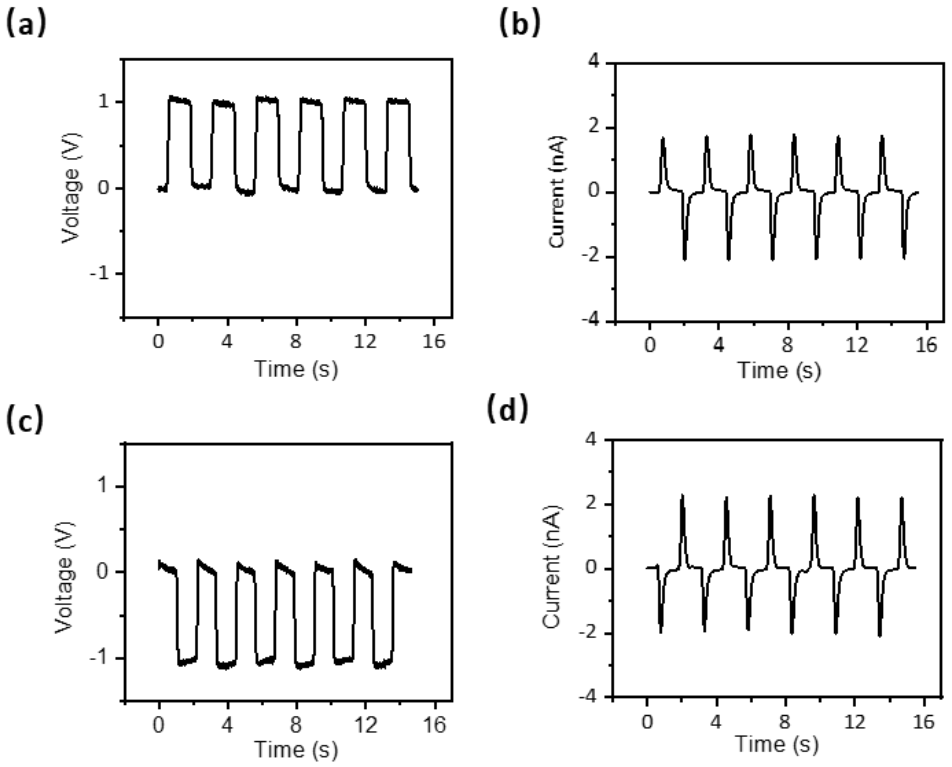

Figure 3.18 Electric outputs when the NG devices are positively connected in (a, b), and reversely connected in (c, d). The concentration of Te nanowires in the Te/PDMS composite is 2%, and strain applied is 12.5%.

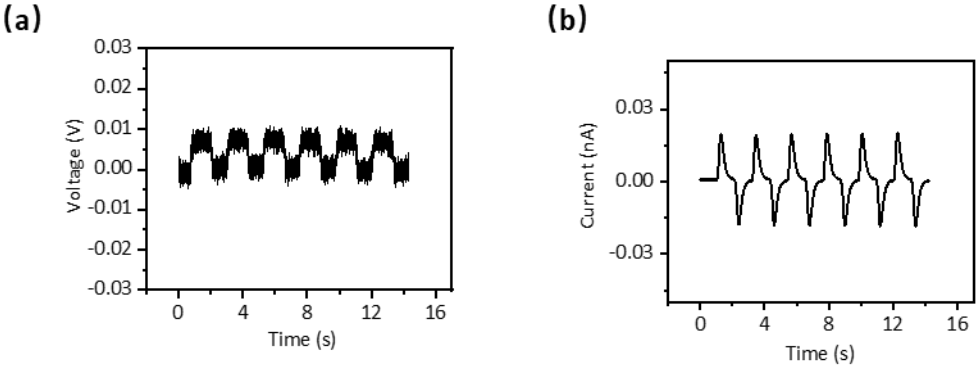

Figure 3.19 The (a) voltage and (b) current output of the device with the absence of Te nanowires, 12.5% strain applied.

3.4.6 Piezoelectric output as a function of the applied strain

The magnitude of the piezoelectric voltage and current outputs are greatly affected by the applied strain. Figure 3.20 shows the V_{oc} and I_{sc} as a relation to the applied strain for the device with

honeycomb structure of which the Te concentration in the Te/PDMS composite is 2%, apparently both the V_{oc} and I_{sc} increase with the strain, the voltage and current outputs of the device under a deformation of 75% are a few times larger than the state of 12.5%. This is because a larger deformation would lead to a stronger piezoelectric polarization and a larger piezoelectric potential, thus more charges would flow out and in between the two electrodes, therefore higher voltage and current outputs would be generated. The relationship between the strain variation and the piezoelectric outputs would provide us a platform to measure the strain by viewing the piezoelectric voltage and current.

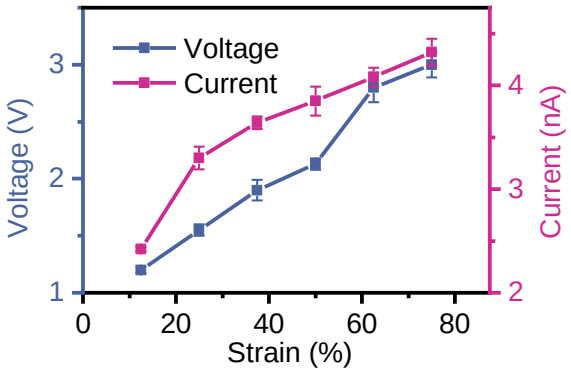

Figure 3.20 The V_{oc} and I_{sc} as a function of strain. Device taken for the measurement is the one with the honeycomb structure, Te fraction of Te in the Te/PDMS composite is 2%.

3.4.7 Piezoelectric output varied as the device structure

Here we also compare the electric signal outputs for the four printed devices with different patterns (Figure 3.21), the voltage and current outputs for these four devices under 50% engineering strain differs a lot (here the Te concentration in the Te/PDMS composite for all devices is 2%), which can be explained by the local strain variations in these structures and the corresponding differed piezoelectric potential. clearly seen from this figure, the device with mesh structure would give rise to the smallest output, while the solid structure would produce the largest output, this observation is in accordance with the mechanics analysis, as the strain distribution among the mesh structure is the most mild among the four ones, which would call the minimum piezoelectricity as a result. It should also be noted here the current output of the solid-structure devices is much higher than the ones from other devices, this is because the solid-structure device's working area is several times as much as the ones of other devices. In piezoelectric devices, the voltage output is not dependent on the working area but the current output is proportional to the working area.

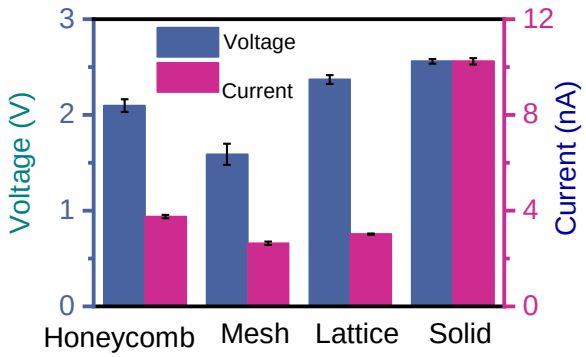

Figure 3.21 The output voltage and current from devices with different patterns, Te fraction of in the Te/PDMS composite is 2%, and the applied strain is 50%.

3.4.8 Power output of the piezoelectric device

The output power of 3D printed PENG delivered to external loads is characterized by varying the load resistance connected in the circuit. Figure 3.22 shows the resistance-dependent output voltage and current when the load resistor was swept from 1MΩ to 1.88 GΩ. The instantaneous output power can then be calculated and plotted as a function of the load resistance, with a maximum output power determined to be 4.11 nW at a load resistance of 0.88 GΩ.

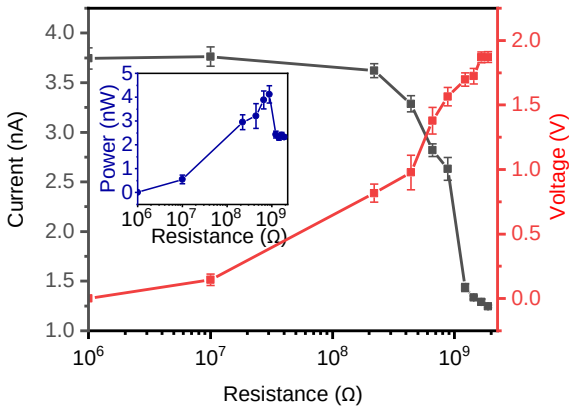

Figure 3.22 The output voltage/current and power (inset) versus the load resistance.

3.4.9 Stability of the piezoelectric device

To demonstrate the real application of the device in external environment, the durability and stability must be considered. As presented in Figure 3.23, even under a periodic stretching and releasing for over 1000 times, the amplitude of the voltage and current output would not degrade

apparently, which is a good sign to prove the long-term stability of our device and its potential application in real situations.

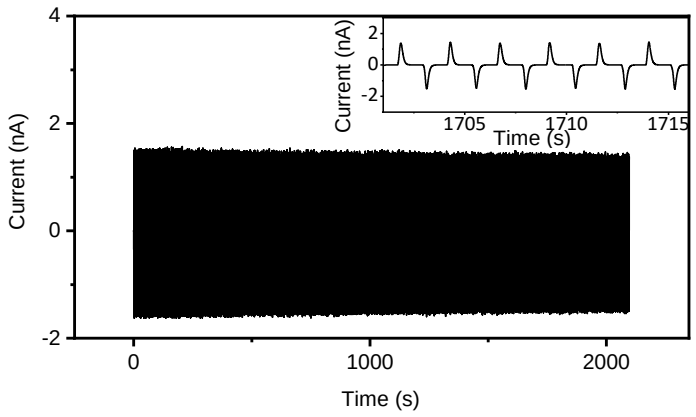

Figure 3.23 The cyclic output of NG device during a stability test, inset is the magnified view of the output signals highlighted. The device under measurement is the one with mesh structure, the default applied strain on device is 12.5% for the afore-mentioned tests, and the default Te nanowires concentration is 2%.

3.5 Gesture recognition based on the piezoelectric device and machine learning technique

3.5.1 Data collection with the piezoelectric device

Finally, we explore the feasibility of 3D-printed PENG device for potential self-powered human-integrated application, e.g., gesture recognition. The wearable 3D-printed device can be attached to a human wrist to detect movement of the underlying tendons as shown in Figure 3.24. Specifically, each finger was bent and released in sequence starting with the thumb (Figure 3.24(a)), since the movement of different fingers can induce various movement of the underlying tendons, as such the piezoelectric device attached on the human wrist can produce various and discernible electrical signals (Figure 3.24(b))[69]. Clearly, the disparate peak forms and magnitudes from the piezoelectric device stimulated by the movement of different fingers can help us recognize the gesture of the participants. This characteristic is very crucial in the current field of human-machine interface and remote sensing.

Here in our study, with the aid of piezoelectric device, we then adopt a currently popular machine learning method to optimize the function of gesture recognition. To collect enough data for the further analysis, we kept the piezoelectric device attached on the human wrist, and each finger was

bent and released for more than 500 times. Figure 3.24 shows the electrical signal as induced by the finger movement for a few cycles, it can be seen that the repetitive bending and releasing of finger would give rise to numerous positive and negative peaks. Here we take advantage of a customized python script to extract the magnitudes of these positive and negative peaks, and then utilize these values for the classification of the movements from different fingers. Specifically, the magnitudes of the positive and negative peaks are refereed as two features for the further classification task. We draw a 2D diagram, in which the horizontal axis (peak 1) and vertical axis (peak 2) correspond to values of the positive and negative peak, respectively.

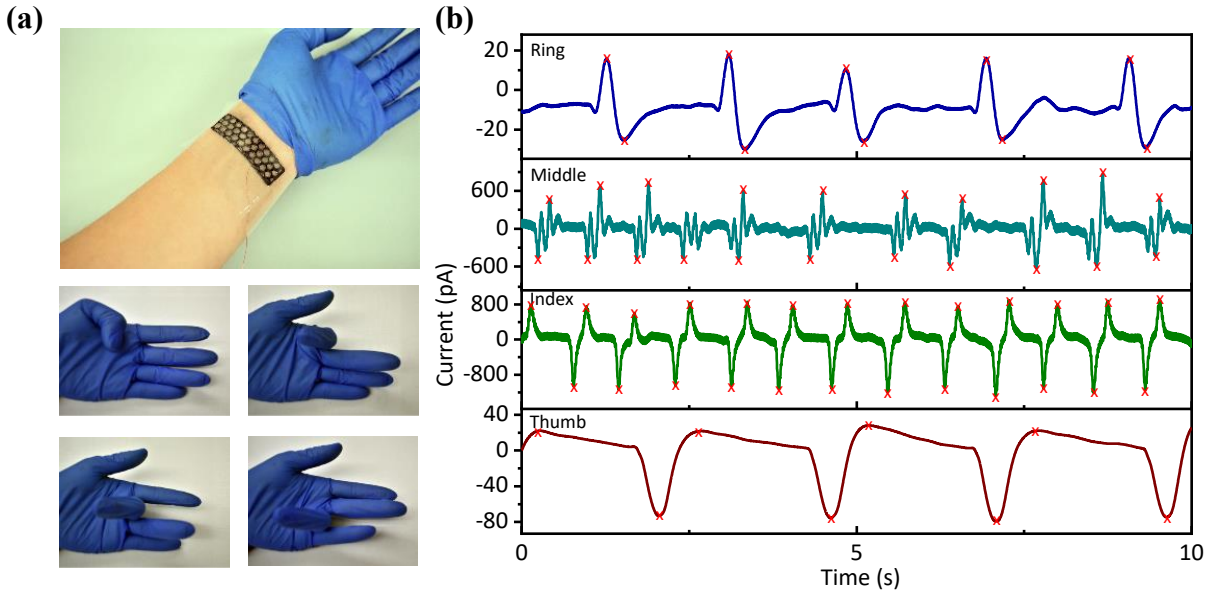

Figure 3.24 (a) Schematic showing the NG device attached on human wrist, and then the thumb, index, middle and ring finger are bent in sequence. (b) The output voltage and current when the four fingers are bent in sequence.

3.5.2 Classification of the data from finger movement and gesture prediction

Then we utilize three popular models for the classification of the finger movement, namely the Logistic Regression model, Support Vector Machine (SVM) model, and the Decision Tree Model. The classification results using these three models are shown in Figure 3.25(a), 3.25(b) and 3.25(c). The regions marked with different colors are the tentative results for the classification task. It is clearly seen that all of these models would have a satisfactory performance, as in both of the

training set and set, the dots from different groups (thumb, index, middle, ring) could be easily distinguished. The Figure 3.26 gives the confusion matrix of these models, we can see that the logistic regression model and decision tree model could yield a 100% accuracy, while the SVM model could give rise to 94% accuracy. These excellent classification results demonstrate the possibility of using the piezoelectric output from our 3D printed PENG as features for the gesture recognition when combined with machine learning approach.

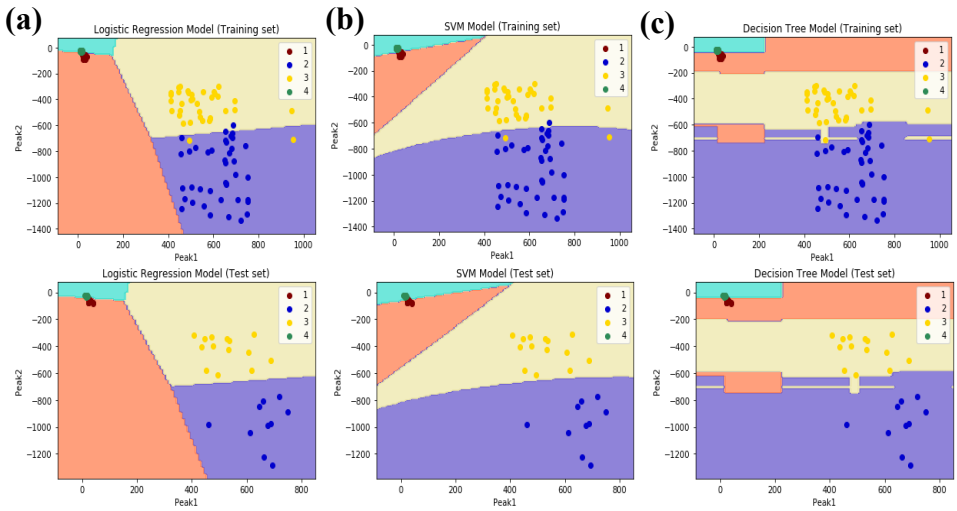

Figure 3.25 Classification result of the electrical output from different fingers using (a) logistic regression, (b) supported vector machine (SVM) and (c) Decision Tree models, respectively.

(a)

		Predicted			
		Thumb	Index	Middle	Ring
Actual	Thumb	13	0	0	0
	Index	0	10	0	0
	Middle	0	0	14	0
	Ring	0	0	0	13

(b)

		Predicted			
		Thumb	Index	Middle	Ring
Actual	Thumb	10	0	0	3
	Index	0	10	0	0
	Middle	0	0	14	0
	Ring	0	0	0	13

(c)

		Predicted			
		Thumb	Index	Middle	Ring
Actual	Thumb	13	0	0	0
	Index	0	10	0	0
	Middle	0	0	14	0
	Ring	0	0	0	13

Figure 3.26 The confusion matrix of the classification results for the different finger movement using (a) Linear Regression Model, (b) Support Vector Machine (SVM) Model, (c) Decision Tree Model, respectively.

3.6 Conclusion

In conclusion, we have demonstrated the fabrication of PENG by a direct writing method, which acquires both patterned structure and aligned piezoelectric nanowires simultaneously. The piezoelectric elements, i.e., Te nanowires, are blended with PDMS matrix and the as-formed Te/PDMS composite serve as piezoelectric sensing layer in the printed device. The whole fabrication process is done in one step, complicated molding and assembling procedures are thus avoided here. Thanks to the efficiency of 3D-printing method, a variety of distinct structures can be easily manufactured, and show different mechanical properties under uniaxial tension. The 3D printed PENG can stably generate electricity when stretched and released periodically, and its piezoelectric performance is highly related to the concentration of Te nanowires in the PDMS matrix and the applied strain. Furthermore, the presented wearable piezoelectric device is capable of detecting small-scale subdermal movement from the tendons in the human wrist and distinguishing different motions and hand gestures. Combined with the machine learning method, the output signals from our devices may make possible the control of embedded electronics and sensors for intelligent and adaptive operations in human-electronics interfacing, bioprobes, and therapeutic devices.

4. 3D PRINTED CHITOSAN HYDROGEL WITH LONG-LASTING MOISTURE AND EXTREME TEMPERATURE TOLERANCE FOR ENERGY HARVESTING AND SELF-POWERED PHYSIOLOGICAL MONITORING

4.1 Introduction

Recently, wearable devices have attracted enormous interest among the researchers from a variety of fields, owing to the devices' conformability to human body and the eligibility to transmit out various in-situ physiological information from wearers[90-92]. Nevertheless, one urgent issue needing to be addressed is to seek an appropriate power source to drive these human-integrated wearable devices[92], or to design and fabricate wearable devices which are intrinsically equipped with self-powering characteristic[88, 93-95].

Based on the coupling effect of contact electrification and electrostatic induction, the triboelectric nanogenerator (TENG) is capable of converting the ubiquitous mechanical energies, which are dissipated among the ambient environment, into our desirable electricity[3]. It has been demonstrated that the TENGs are good candidates in green energy harvesting[96]. In addition, due to the fact that the TENG devices are eligible to deliver distinct electric outputs when they are triggered with diverse mechanical stimulus, the TENGs exhibits great potential as being utilized as human-integrated self-powered sensors[97]. To better realize this aim, many efforts are paid on the optimization of device design for augmenting electric output[98-101], and also rendering the device more flexibility to make them better adapt to human body and deform accordingly with human motions without deterioration of device performance[102-104]. Moreover, it is also highly necessary to develop novel TENGs with environmental friendliness to meet the demand of green electronics. Quite a lot of researches have been made on exploring the natural biopolymers as components in TENG devices and investigated their effect on the TENG's output and practical application[105-108]. All of these efforts help pave a way in applying the TENGs as self-powered and human-integrated wearable devices.

Hydrogel, a three-dimensional network of hydrophilic polymer chains with water as the dispersion medium, has attracted tremendous research interest in recent years in the field of bioelectronics, owing to their inherent properties like high flexibility, transparency, and biocompatibility[18, 109].

There are a couple of studies in which the electrically or ionically conductive hydrogels are encapsulated within soft rubbers and serve as flexible/stretchable electrodes for TENG devices[110-112], realizing a stable and robust triboelectric output. However, very few researches about utilizing the hydrogel as triboelectric layers has been reported yet, since hydrogel is unstable and very susceptible to the externally environmental change like humidity or temperature[113]. The dehydration would cause the morphology change and function failure of hydrogel-based device. To solve this challenge, introducing glycerol into hydrogels network may provide a feasible method[114]. This is due to the fact that the glycerol could form strong hydrogen bonds with water molecules in the hydrogel network, further preventing the formation of ice crystals at low temperatures and attenuating the evaporation of water at high temperatures[115], which are beneficial for diminishing the hydrogel dehydration and enhancing the device's stability. Several research reports published before have confirmed the functionalities of glycerol for the water loss prevention in hydrogel network[115-116].

Another challenge associated with the device fabrication is the hydrogel preparation technology. The general hydrogel-based device process relies on the mold casting and the further manual assembly of cast segments. Additive manufacturing, also called 3D printing, provides us a different and facile strategy to construct arbitrary, delicate, and continuous structures from bottom-up method[79, 117]. Among the various 3D printing methods, direct ink writing (DIW), which count on extruding the filament directly through a nozzle by a patterned path and then forming a free-standing 3D structure in a layer-by-layer sequence, have attracted much attention due to its economy and feasibility[11]. A wide variety of hydrogel-based devices have been fabricated via DIW methods[79] and their applications in the field of biomedicine[118-119], flexible electronics[120], and actuators[121-122] have been demonstrated.

Here in our current experiment, we prepared a highly flexible chitosan hydrogel with long-lasting moisture and extreme temperature tolerance via 3D printing, and utilized it as a new kind of positive electrification layer integrated in TEND devices. Chitosan was anticipated to be an ideal triboelectrically positive materials due to the low cost, tremendous existences of amino group on its monomer[106, 123-124]. In our previous work, we have demonstrated that chitosan dried film is able to generate a TENG output with open-circuit voltage (V_{oc}) of ~1.6 V and short-circuit current (I_{sc}) of ~10 nA[106]. Through a molecular surface engineering, the output could be promoted to 16.2 V

and 125 μA/m^2, respectively[124]. However, the lack of flexibility of chitosan dried film limits its further application, thus their hydrogel counterpart is under investigation in this current work. Here in our experiment, the chitosan hydrogel is crosslinked with the assistance of Cu^{2+} in an alkaline water/glycerol mixture environment. The participation of glycerol greatly enhances the anti-freezing and anti-heating properties of hydrogels, which enables its use in an environment with a temperature ranging from -20 ℃ to 60 ℃. Furthermore, we adopted the DIW method to fabricate hydrogels with various shapes, for an attempt to enhance its elasticity, stretchability as well as the TENG output. The TENG device can effectively generate electricity when it is applied with a periodic contact-separation process, and a long-term stability is also revealed. Furthermore, the whole device shows good transformability and can be attached to the human body for self-powered physiological monitoring, by converting the imperceptible time-variant mechanical vibration from human body into distinguishable electrical signals.

4.2 Pre-gel ink preparation and 3D printing for device fabrication

4.2.1 Chitosan pre-gel and hydrogel preparation

Solution with the final chitosan concentration as 5 wt.%, was prepared by dissolving chitosan powder in a water/glycerol mixture (50%/50% v/v) with 2 vol.% acetic acid. Protonation of amino groups ($-NH_2$) on the chitosan chains would occur once the power gets contact with acetic acid, and thus the as-formed positively charged group ($-NH_3^+$) would render the chitosan powder a good solubility in weak acid solution, then a paste-like product could be obtained[45]. A photograph of our prepared chitosan paste is shown in Figure 4.1.

A chitosan hydrogel can be prepared by simply placing the chitosan paste into an alkaline environment, the neutralization of $-NH_3^+$ groups and the further entanglement of chitosan chains can give rise to the formation of a physically crosslinked hydrogel. However, the mechanical strength of the physically crosslinked chitosan hydrogel is extremely weak, especially under hydrated conditions[125]. To address this issue, we introduce Cu^{2+} to assist the chemical crosslinking of chitosan hydrogels. Here in our experiment, $CuSO_4$ powder was used as the source of Cu^{2+} in the system, which was added to pure chitosan solution to form a mixture paste, as the photograph shown in Figure 4.1(b). Once the $-NH_3^+$ groups are neutralized and transformed into $-NH_2$ groups, Cu^{2+} ions will be bonded to the $-NH_2$ groups from neighboring chitosan chains[126]. As such a

chemical crosslinking process is involved, which contributes to the enhancement of the mechanical properties of the hydrogel.

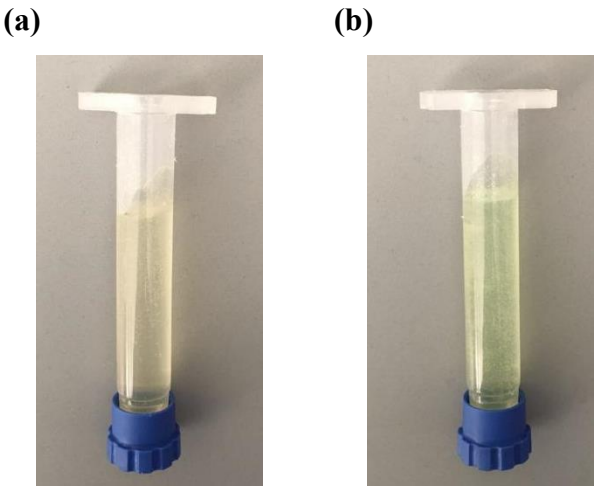

Figure 4.1(a) Pure chitosan paste and (b) Cu^{2+}-chitosan paste dissolved in water/glycerol mixture with the aid of acetic acid and then loaded in syringes.

4.2.2 3D printing process for the chitosan hydrogel fabrication

Chitosan hydrogel was prepared as the schematics shown in Figure 4.2. For the 3D printing process, the as-prepared Cu^{2+}-chitosan paste ink was loaded into a syringe for the direct-ink-writing (DIW), during this process the ink filament was extruded out from a nozzle under an applied pressure controlled by an air-powered dispensing system. A 3D pattern is printed by depositing Cu^{2+}-chitosan paste filaments in a layer-by-layer manner, the nozzle movement and the filament dispensing path is fully controlled by a three-axis positioning platform, in such a way a paste skeleton with our designed and desired structure can be successfully fabricated. The gelation of the printed Cu^{2+}-chitosan paste skeleton was then conducted in an alkaline environment, which hereby is a coagulation bath with 10 wt.% NaOH aqueous solution. Detailed experimental setup was presented as in Figure 4.3.

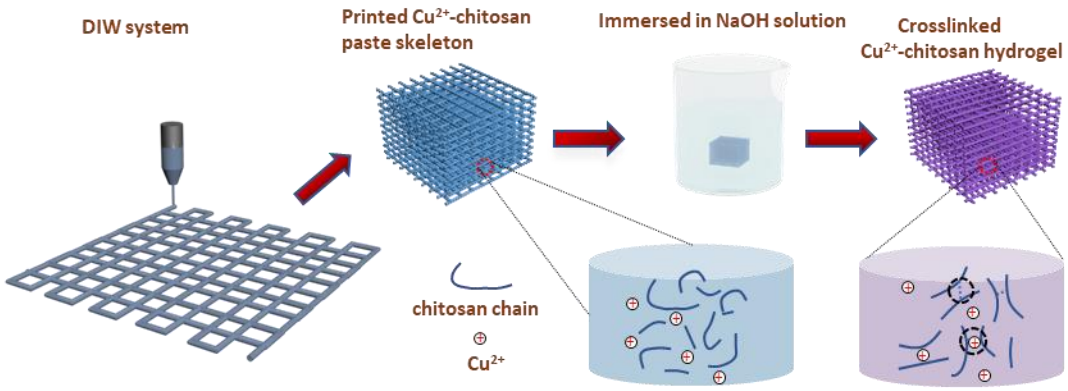

Figure 4.2 Schematics for the 3D printing and further crosslinking process of Cu^{2+}-chitosan hydrogel.

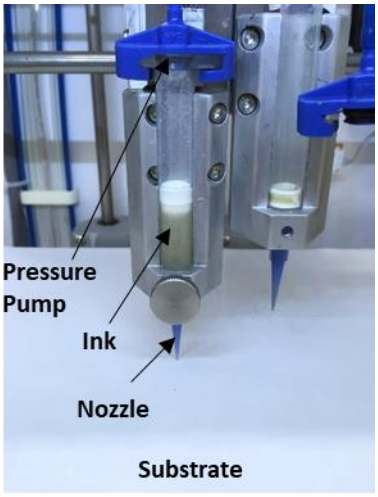

Figure 4.3 Experimental set up for the 3D printing process.

4.2.3 Crosslinking mechanism of the hydrogel

The volume of coagulation bath was much larger than that of chitosan solution, so the c(OH-) could be considered as constant. In the gelation process, with the rises of pH, the entanglement of the chitosan molecules and the hydrogen bonds greatly holds back the movement of chitosan molecule chains. Moreover, as we illustrated above, each Cu^{2+} ions will form covalent bonds with two chitosan molecules[126], the as-formed coordinated complex significantly loses its fluidity, thus a stable hydrogel is successfully obtained. The coupling of the physical linking and crosslinking mechanism would give rise to the formation of a stable Cu^{2+}-chitosan hydrogel. A schematic of the crosslinking mechanism was depicted in Figure 4.4.

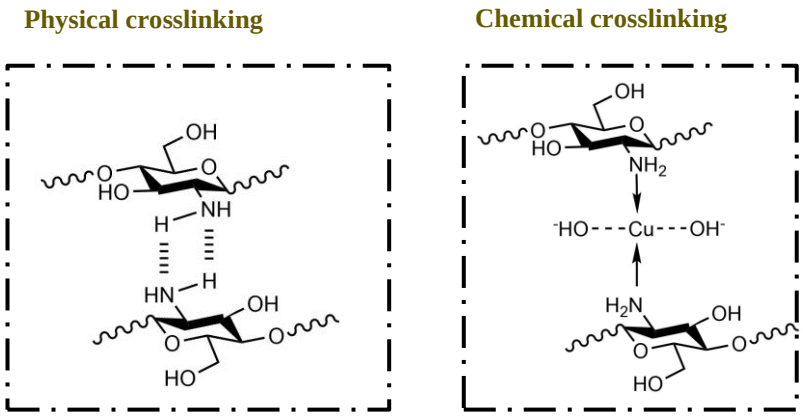

Figure 4.4 Schematics for Cu^{2+}-chitosan hydrogel gelation mechanism.

4.2.4 Characterization of the rheological properties of the materials ink

Here in order to better elucidate the printability of the pre-gel ink, the rheological properties of the Cu^{2+}-chitosan ink was characterized initially. Figure 4.5(a) and 4.5(b) provided the viscosity and storage modulus, loss modulus results of Cu^{2+}-chitosan pre-gel. With the increase of shear rate, viscosity of pre-gel declines gradually (Figure 4.5(a)), which confirms its shear-thinning properties[11], thus the pre-gel ink can be successfully extruded out from the syringe. Elastic/storage modulus (G') and viscous/loss modulus (G'') are compared when the shear stress is ranged from 0.1 to 1000 Pa (Figure 4.5(b)). Specifically, the pre-gel ink shows a plateau value of a storage modulus of 800 Pa, and a loss modulus of 400 Pa. The fact that G' plateau exceeding G'' plateau conveys the information that the printed ink would immediately turn into a rigid filament and maintain a solid structure after the shear stress disappears, prior printed layer would be strong enough to support the subsequent upper printing layer[84].

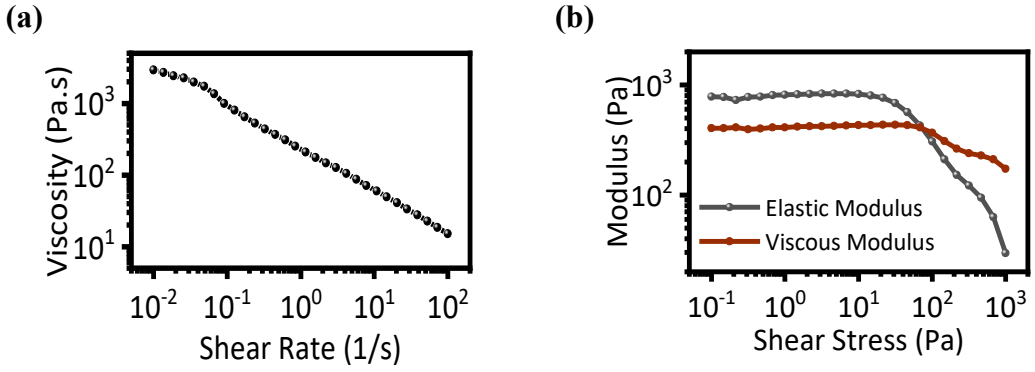

Figure 4.5(a) Viscosity versus shear rate, (b) Elastic/viscous modulus versus shear stress for the Cu^{2+}-chitosan pre-gel.

4.2.5 Demonstration of the printability of the pre-gel ink

Figure 4.6 presented a printed Purdue mascot with the Cu^{2+}-chitosan filament, further proving the printability of the paste ink. We also took advantage of the DIW technique to fabricate a cubic structure and a ring structure with the ink, and the result in Figure 4.6 demonstrated that 3D structures could also be realized facilely.

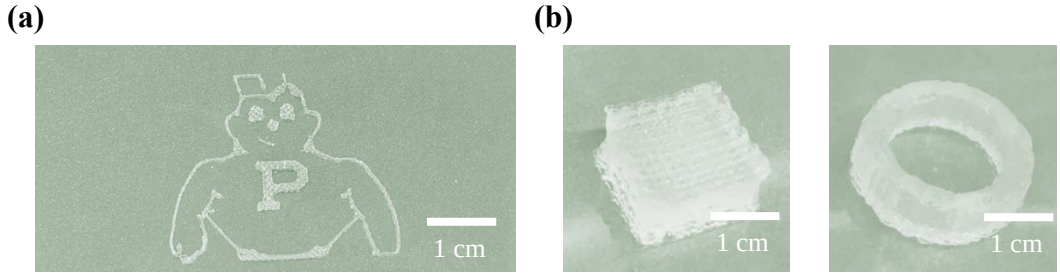

Figure 4.6 (a) Printed Purdue mascot, (b) 3D cubic and ring structure with the Cu^{2+}-chitosan paste ink.

4.3 Cu^{2+}-chitosan hydrogel characterization

In order to better elucidate the formation mechanism of the Cu^{2+}-chitosan hydrogel, a couple of characterization techniques are utilized here. SEM image indicated that the freeze-dried hydrogel sample is quite uniform, and no particles are adhered to the surfaces, indicating that the Cu^{2+} are involved in the hydrogel formation process rather than simply precipitate out as $Cu(OH)_2$ when coming into contact with OH^- (Figure 4.7). XRD curve shown in Figure 4.8(a) proved that the chitosan hydrogel formed in water/glycerol mixture with the participation of metal ions are short-order crystalline to some extent, as there is a broad peak available peak located at ~20^o [127]. It should be noted here that the profile of the sample only show characteristic diffraction peak of chitosan ($2\theta=20^o$), no diffraction peaks of $Cu(OH)_2$ or other inorganic components are present, which is another sign that all the Cu^{2+} participated in the formation of the Cu^{2+}-chitosan hydrogel complex. In Figure 4.8(b), we examined the Fourier-transform infrared spectroscopy (FTIR) of the Cu^{2+}-chitosan hydrogel sample. Broad peaks at 3365 cm^{-1} and at 2967 cm^{-1} were related to –OH and C–H stretching, respectively. A peak found around 1585 cm^{-1} indicated the presence of N–H group. A peak at 1442 cm^{-1} was ascribed to the $–CH_3$ symmetrical deformation mode. Another two peaks found around 1152 and 1067 cm-1 can be assigned to the C–O stretching vibration in chitosan. A characteristic peak of Cu^{2+}-chitosan hydrogel is found at 1623 cm^{-1}, corresponding to the formation

of coordinate-covalent bonds from reactions between amino groups of chitosan and copper metal ions[128].

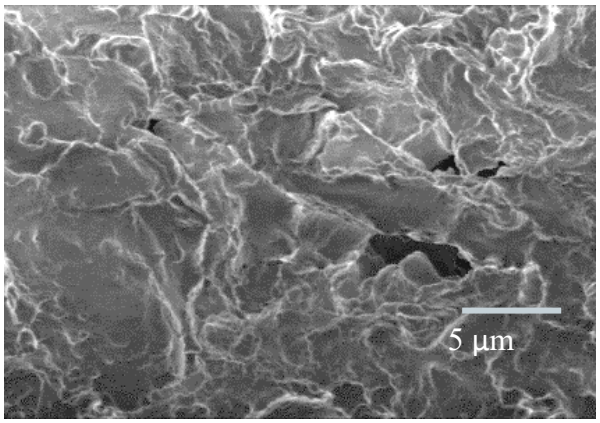

Figure 4.7 SEM images of the freeze-dried Cu^{2+}-chitosan hydrogel.

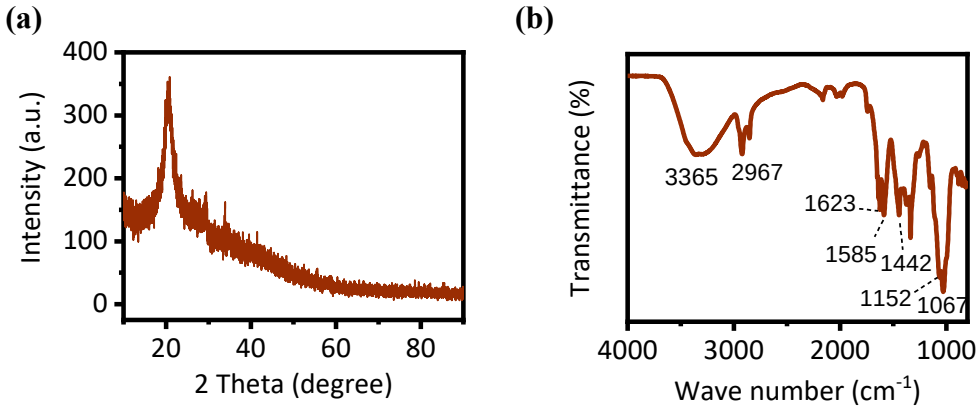

Figure 4.8 (a) XRD pattern, and (b) FTIR spectra of the freeze-dried Cu^{2+}-chitosan hydrogel.

4.4 Demonstration of the long-lasting moisture and extreme temperature tolerance of Cu^{2+}-chitosan hydrogel

4.4.1 Weight percentage remaining for the hydrogel under hot and cold environment

As demonstrated above, in our experiment, the Cu^{2+}-chitosan hydrogel is crosslinked in a 3D network of water/glycerol mixture. Based on our assumption, when the Cu^{2+}-chitosan hydrogel is formed in a medium of water/glycerol binary system, the ability of glycerol maintaining water would provide a stable environment for the hydrogel to prevent the potential water loss. To verify this viewpoint, we compare the anti-freezing and anti-heating properties of Cu^{2+}-chitosan hydrogel as formed in pure water or water/glycerol mixture, respectively. Here we prepare a few cylinders hydrogel samples with diameters of 1 cm and heights of 1 cm. From the photographs in Figure 4.9

and 4.10, it can be clearly seen that the hydrogel formed in pure water is very susceptible to the external environment, after being exposed at room temperature (25 ℃) for one day, the hydrogel would undergo a severe shrinkage process, the remaining weight percentage is only half of the fresh one. While for the hydrogel formed in water/glycerol mixture, its weight and morphology would not shift too much (over 90% retained). Even being exposed to hot or cold environment, i.e., 60 ℃ and -20 ℃ respectively in our experiment, the hydrogel can still maintain its weight well, leaving 85.6% and 87.5% of its original weight after one day. The relative humidity of the test environment was also under constant monitoring to be kept at 55%. This experimental result reveals that the Cu^{2+}-chitosan hydrogel formed in the water/glycerol mixture is quite stable across a wide temperature range from -20 ℃ to 60 ℃, which almost cover the usual working temperature range of the bioelectronics.

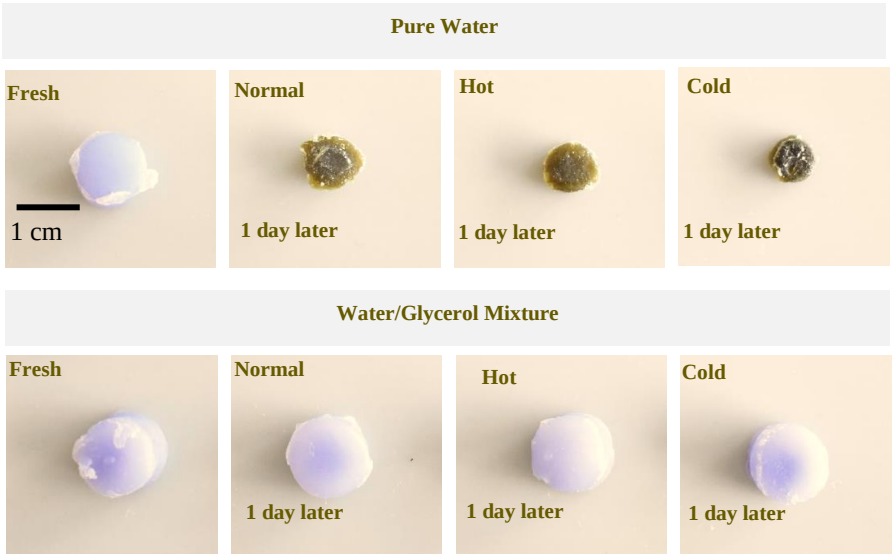

Figure 4.9 Photographs of Cu^{2+}-Chitosan hydrogel formed in water or water/glycerol mixture and exposed under normal (25 ℃), hot (60 ℃) and cold environments (-20 ℃) for one day.

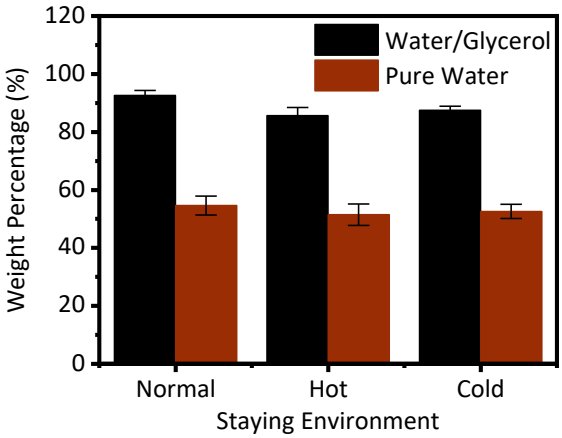

Figure 4.10 Remaining weight percentage of hydrogel under normal (25 °C), hot (60 °C) and cold environment (-20 °C) for one day.

4.4.2 Mechanism of the water-locking property in the water/glycerol binary solvent system

The detailed mechanism was further clarified in Figure 4.11. Glycerol molecules would form strong hydrogen bonds (dashed lines in the figure) with water molecules and compete with hydrogen bonds in water, thus disrupting the formation of crystal lattices of ice at low temperatures as well as prevents the evaporation of water at high temperatures. The strong hydrogen bonding between glycerol and water enable the hydrogel to firmly lock water molecules in the network. Therefore, the Cu^{2+}-chitosan hydrogel exhibits remarkable anti-dehydrating properties, which greatly extends its application area in a wide temperature range. Here we also investigated the water locking efficiencies of the hydrogels as a function of the proportion of glycerol in the water/glycerol binary system. The weight of the hydrogel samples are also measured at varying time to characterize their anti-dehydrating capacities. It can be seen from Figure 4.12 that the water locking efficiency of the hydrogel proportionally increases with the glycerol content in the water/glycerol mixture. However, an excessively high glycerol proportion (75% v/v) in the water/glycerol mixture would lead to a very viscous Cu^{2+}-chitosan paste, which could cause trouble on the handling of hydrogel fabrication process. Therefore, for the subsequent device fabrication, we adopt the 50%/50% v/v water/glycerol mixture as the binary solvent system for the preparation of Cu^{2+}-Chitosan hydrogel.

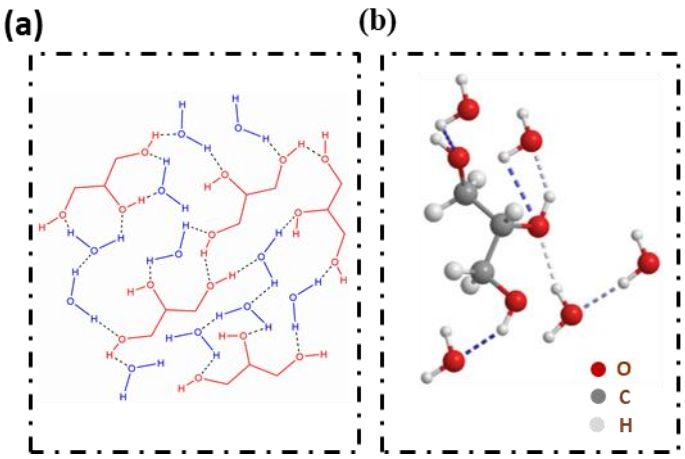

Figure 4.11 Mechanism of the water-locking property in the water/glycerol binary solvent system.

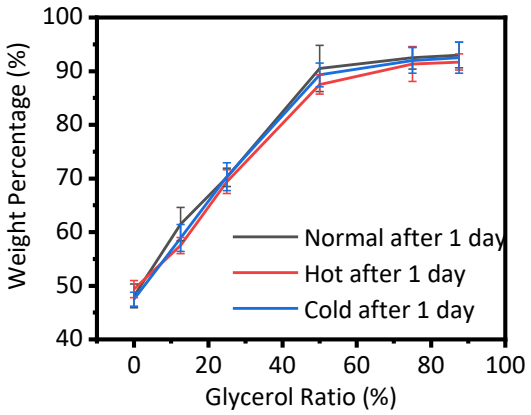

Figure 4.12 The remaining weight percentage of the Cu^{2+}-chitosan sample formed in a water/glycerol mixture with different glycerol ratios and exposed to normal (25 ℃), hot (60 ℃) and cold environment (-20 ℃) for one day. Relative humidity was kept at 55%.

4.4.3 4.4.3 Mechanical properties of the hydrogel under hot and cold environment

Compression test was done to test the mechanical properties of Cu^{2+}-chitosan hydrogel. Detailed parameters are shown in the Methods section and supporting information. As shown in Figure 2d, the Young's modulus and compression strength for the hydrogel formed in water/glycerol mixture were ~180 kPa and ~400 kPa, respectively. These measured results indicated that the Cu^{2+}-chitosan hydrogel as formed in water/glycerol binary system is relatively stiff as compared to the conventional pure chitosan hydrogel (Young' modulus of ~2 kPa, compression strength of ~30 kPa)[129]. This is due to the fact pure chitosan hydrogel without the presence of Cu^{2+} is crosslinked

only by the physical entanglement of the polymer chains. While for the Cu^{2+}-chitosan hydrogel, an ionically cross-linking process is involved due to the covalent bonding between the Cu^{2+} and chitosan molecules, resulting in a higher mechanical strength of the hydrogel accordingly, which would be advantageous for the application in soft bioelectronics. It should be noted that even after being exposed at hot (60 ℃) or cold (-20 ℃) environment for one entire day, no obvious changes had been observed from the compression stress-strain curve, further demonstrating that the hydrogel samples possess a great anti-freezing and anti-heating capability.

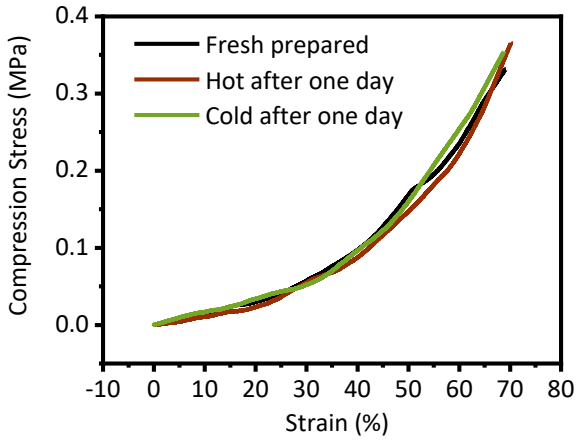

Figure 4.13 Compression stress-strain curve of fresh prepared hydrogel and the ones exposed to hot (60 ℃) and cold (-20 ℃) environment for one day.

4.5 3D printing for the manufacturing of hydrogel device with different structures

In previous part, we have already proven that the as-prepared Cu^{2+}-chitosan paste in the water/glycerol mixture is suitable for 3D printing. Here we further demonstrate the possibility of utilizing DIW method and Cu^{2+}-chitosan paste filament to fabricate device with different morphologies, shapes according to our design. In a typical hydrogel extrusion-based 3D printing process, a structure is plotted with Computer-Aid-Design (CAD) software firstly, and then the pattern was translated into a language which can be read by the 3D printer, which is the so-called G-code. As displayed in Figure 4.14, a couple of different patterns can be directly fabricated using the DIW technique, such as honeycomb structure, grid structure, and triangle structure (The left ones are the plotted design, and the right ones are the optical images of the printed structure). The final prepared hydrogel shapes slightly differ from the plotted design, this is because there exists a certain degree of shrinkage in paste-hydrogel transformation process.

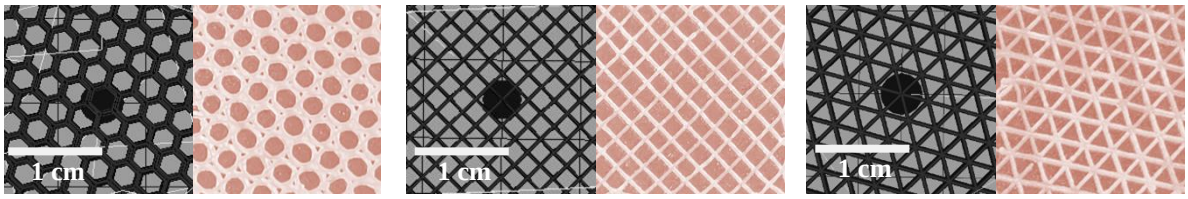

Figure 4.14 3D printed hydrogel film with different shapes, patterns and geometries.

4.6 Triboelectric properties characterization of the chitosan TENG

4.6.1 Device fabrication of the Chitosan-based TENG

Then the possibility of the printed hydrogel sample working as a component in TENG devices was investigated. Due to the abundant existence of -NH_2 on chitosan chains[130], it is anticipated that Cu^{2+}-chitosan hydrogel would exhibit strong triboelectrically positive properties as the -NH_2 group tends to donate electrons easily when contacting with other objects. Therefore, here we attempted to utilize our prepared Cu^{2+}-chitosan hydrogel as a triboelectrically positive layer for the further assembly of a TENG device. Here a flat layer of Cu^{2+}-chitosan paste was printed on the surface of an ITO-coated PET film, then the paste was gelated in NaOH solution and a semi-transparent hydrogel layer is formed accordingly. The anti-dehydrated hydrogel layer would work as a positive friction layer and the bottom ITO layer serves as an electrode for the charges collection, an as-made device was presented in Figure 4.15.

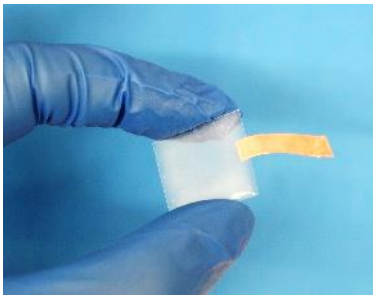

Figure 4.15 Photographs of as-made hydrogel TENG sample.

4.6.2 Working mechanism of the chitosan-based TENG

Figure 4.16 illustrates the working mechanism of our TENG device. In our experiment, the TENG device is based on a contact-separation mode, Kapton film attached on another PET/ITO layer is selected as the negative friction layer. According to the triboelectric series, Kapton and Cu^{2+}-chitosan hydrogel can be considered as triboelectrically negative and positive materials,

respectively, due to their different electronegativity[5]. Tribo-electrification together with the electrostatic induction effect contributes to the energy generation of the TENG. Initially, the hydrogel keeps in contact with the Kapton layer, charges transfer from the hydrogel to the Kapton, making the Kapton layer negatively charged, and the hydrogel positively charged. When the hydrogel is moved away from the Kapton, an electrical potential difference is built between the two separated oppositely charged surfaces. Then a transient charge flows between the two electrodes, generating a current pulse. An electrostatic equilibrium is achieved when the hydrogel layer and the Kapton layer reach the maximum separation distance. As the hydrogel moves back again, the process is reversed, and a charge flow along the opposite direction appears. Thus, the continual contact-separation motion described above produces an alternative current. The detailed mechanism of the triboelectric charges generation and the origin of nanogenerators are discussed in the recent research paper reported by Wang et al, which is highly related to the Maxwell's displacement current[5].

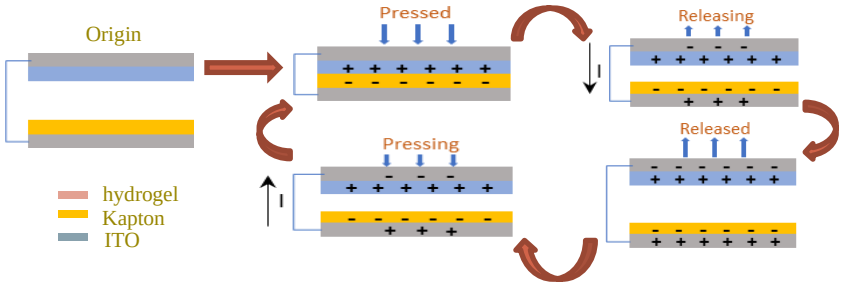

Figure 4.16 Schematics of the working mechanism of the hydrogel TENG.

4.6.3 Triboelectric output of the hydrogel-based TENG

Here in our experiment the hydrogel film is with a size of 2 cm × 1 cm × 1 mm. By tapping the hydrogel layer with Kapton repetitively through a linear motor, a periodically voltage, current and charge signal can be detected. The Cu^{2+}-chitosan hydrogel was capable of generating an approximate open-circuit voltage (V_{oc}) of 4.5 V (Figure 4.17(a)), short-circuit current (I_{sc}) of 20 nA (Figure 4.17(b)) and short-circuit transferred charges (Q_{sc}) of 1.75 nC (Figure 4.17(c)), respectively.

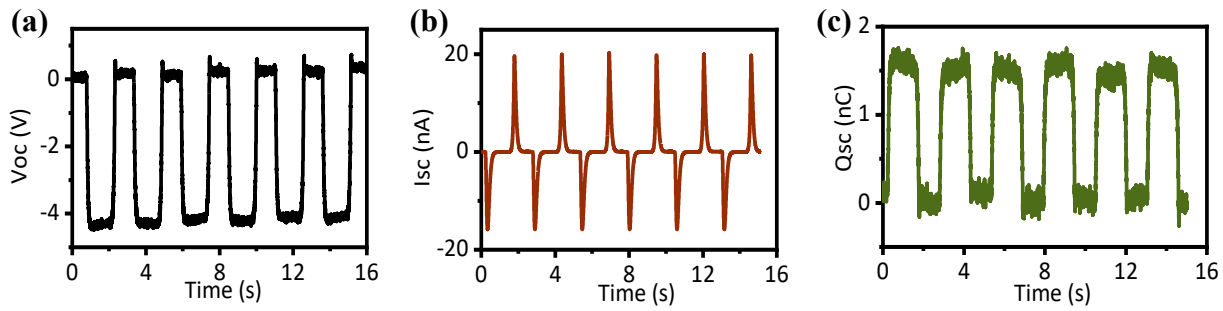

Figure 4.17 (a) V_{oc}, (b) I_{sc} and (c) Q_{sc} of a hydrogel TENG.

4.6.4 Power output of the TENG device

By connecting the TENG device with external resistor, power output as a function of external resistors was examined and presented in Figure 4.18. The voltage output increases with the resistance, while the current output decreases with the resistance. The power is expressed as the product of the voltage and current outputs, thus the power would reach a peak of 194 μW/m^2 when the external resistance is equal to 400 MΩ.

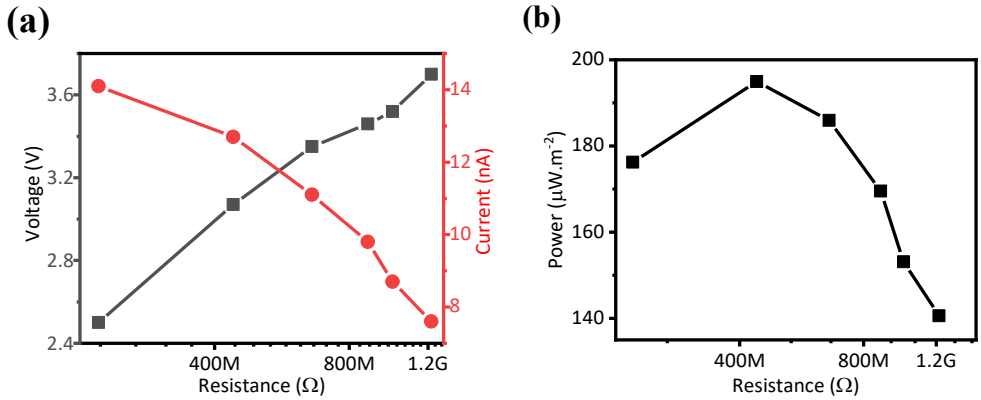

Figure 4.18 (a) The output voltage and current and (b) the output power of the hydrogel TENGs with the varying resistance of external loads.

4.6.5 Stability of the TENG device

In addition, the stability of the TENG was characterized by the tapping the hydrogel for a long time. As shown in Figure 4.19, even after working for 2300 cycles, nearly 1.3 hours (test environment: 25 ℃, 55% RH), there was still no obvious degradation of the current output, which was a good sign to demonstrate the long-term stability of the device. The TENG output

demonstrated that our as-made hydrogel exhibits a high potential for the energy harvesting devices or self-powered sensors.

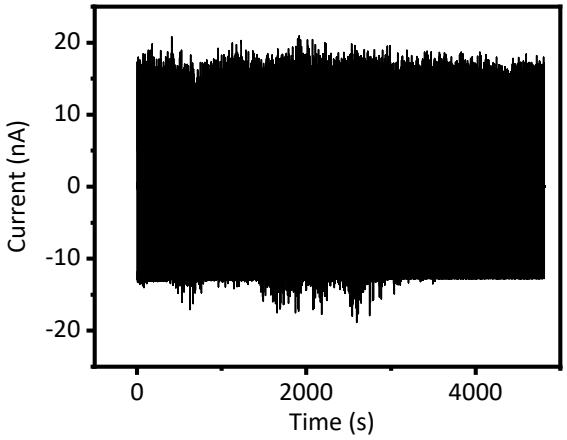

Figure 4.19 The output current of a hydrogel TENG with an external load that lasted for 2300 cycles of contact-separation motions (1.3 hour). The test temperature is 25 ℃ and RH is 55%.

4.6.6 Triboelectric output of the TENG device after being stored in different environment

To better demonstrate the anti-dehydration properties of Cu^{2+}-chitosan hydrogel and its suitability as a positive friction layer in TENG device, we tested the performance of hydrogel TENG device being placed in varying environment. Apparently, as confirmed in Figure 4.20, the triboelectric output of the device was quite stable, other than a small decrease for the device at high temperature around 60 ℃ after one day. This is in accordance with the observance from Figure 4.9(a) and 4.9(b), in which an appropriate 15% weight loss was measured when the hydrogel samples were put into hot environment (60 ℃) for over one day.

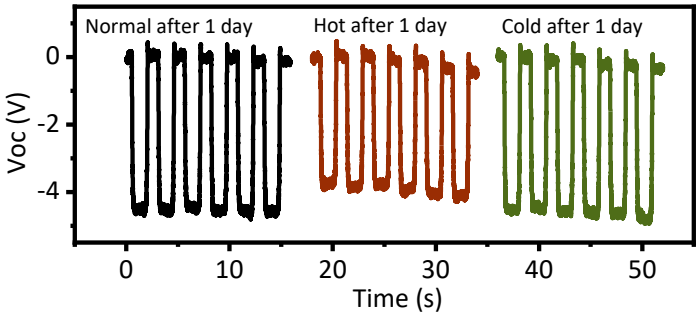

Figure 4.20 The triboelectric output of the hydrogel TENG after setting in normal, cold and hot environment for one day.

4.6.7 Triboelectric output of the TENG device with different structures

The electric output of the TENG device is largely dependent on its morphologies, here by changing the morphologies and shapes of our TENG device via the aforementioned DIW approach, we successfully realized tuning the triboelectric output by a facile way. Clearly shown in Figure 4.21, the hydrogel layer with honeycomb, grid, and triangle structures are able to generate Isc of 8.5, 9.2 and 8.7 nA respectively , which are relatively small as compared to the output from the previous 100% filled solid sample (~20 nA). This agrees with our expectation as the effective contact areas of these porous structures are smaller than the 100% filled one. However, the Voc of these four structures are almost the same as the solid one, since the voltage output of a typical TENG device based on contact-separation mode would not be altered by the contact area[131-132].

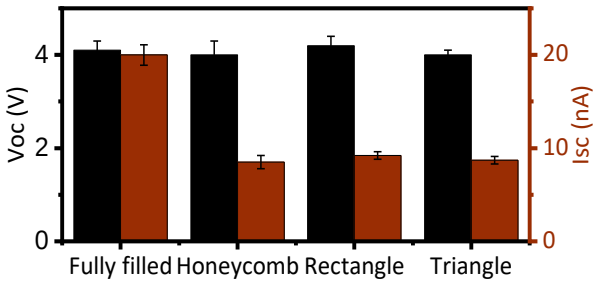

Figure 4.21 The triboelectric output of the hydrogel TENGs with different shapes.

4.7 Human-integrated application of the hydrogel-based TENG device

4.7.1 Device Fabrication

To further demonstrate the application of hydrogel as energy harvesting or tactile sensing devices, we fabricated a TENG device using the hydrogel as the schematics shown in Figure 4.22. Here we firstly fabricated a patterned hydrogel layer with a series of spacers with the DIW method, then another PDMS layer with an embedded Ag nanowires layer is covered on the top. The spacers on the hydrogel would separate and support the top PDMS layer. Figure 4.23 depicts the schematics of the designed patterned hydrogel layer and also the optical images of the real fabricated one, while Figure 4.23(c) shows the final TENG device, here the gap between the top PDMS layer and the bottom hydrogel layer could be clearly seen. For this device, it is anticipated that the contact area between the PDMS layer and the hydrogel layer would be shifted to some extent when an external mechanical stimulus is triggered, further generating a triboelectric signal per the mechanism as we illustrated in Figure 4.16. The reason why we choose the PDMS as the counter

layer lies on two facts. Firstly, PDMS is endowed with a great biocompatibility, which assures the sensor's application for human-integrated purpose. Secondly, PDMS has a strong tendency to absorb electrons when contacted with other materials, as evidenced in the triboelectric series chart, therefore the TENG device made of PDMS and chitosan hydrogel could output a relatively large triboelectric current even when a trivial mechanical stimulus is in presence, which ensures the high sensitivity of the device and paves a way for the sensor's use for capturing small mechanical signals.

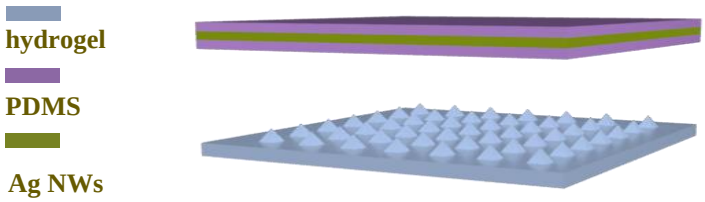

Figure 4.22 Schematic of the TENG sensor fabricated with Ag nanowires-embedded PDMS and chitosan hydrogel.

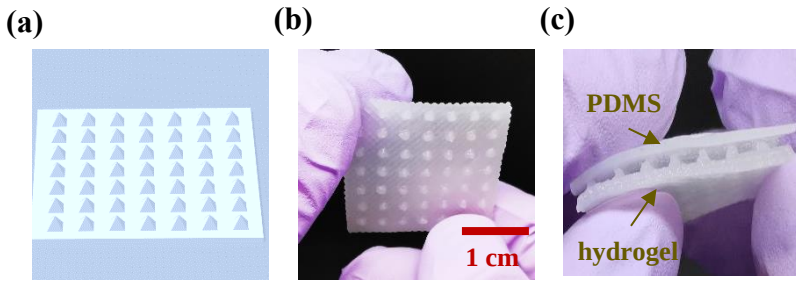

Figure 4.23 (a) Schematics and photograph of the patterned hydrogel layer with pyramid structure; (b) Photograph of the final assembled TENG sensor.

4.7.2 Human-integrated application of the TENG sensor

To validate our assumption, the TENG device was then attached to different parts of human body, and worked as a self-powered sensor for physiological monitoring. The TENG device can be attached to the throat for identifying different vocal activities, e.g., coughing, gargling, and swallowing (Figure 4.24).

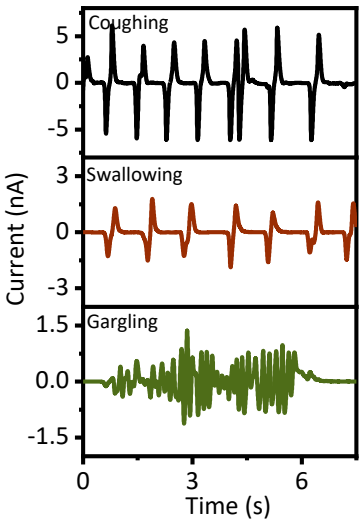

Figure 4.24 TENG sensor adhered on throat for identifying different vocal activities.

In addition, we attached our device on the wrist of a 27-year-old participant for an attempt to detect the heart pulse in a self-powered and non-invasive way (Figure 4.25). The sensor utilized here is quite flexible and conforms to the wrist well, so very minor pulse vibration can be captured and shown in the electric signal output. It could be easily observed from Figure 4.25(b) that the electric signal generated from the wrist pulse varied a lot at two different states, before and after exercise. In addition, we find that the real-time triboelectric current output from the device adhered on wrist for 30 s shows the reliable detection and measurement of the human pulse signals, with distinct three-peak characteristics for the cardiac cycle (Figure 4.25(c)). Such a pattern is consistent with the reported results[70-71], and manifests important information for the health diagnostics. Here we attempted to analyze the acquired signals. Three distinguishable determinants could be obtained from one typical pulse cycle[72, 74, 133]: namely, early systolic peak pressure ($P_1(t_1)$: percussion wave (P-wave)), late systolic augmentation shoulder ($P_2(t_2)$: tidal wave (T-wave)), and diastolic pulse waveform ($P_3(t_3)$: diastolic wave (D-wave)). The characteristic pulse pressure shape (PPS) was developed from superposition of ejected blood wave by the left ventricular contraction and the reflected blood wave from the lower limb. These peaks can be used to quantify the radial artery augmentation index ($AI_r = P_2/P_1$), and the time delay between the first and second peaks ($\triangle t = tp_2 - tp_1$), which provide valuable information for evaluating the physiological conditions of the human cardiovascular system like arterial stiffness and pulse wave velocity (PWV)[73-75]. The calculated AI_r and $\triangle t$ using hydrogel TENG are 0.39 and 0.19 s, respectively, which fall in a

normal and healthy range for an adult of 27 years old[73-75]. The demonstrated self-powered sensing capability to detect the small-scale biomechanical signals from the human body, together with the facile and low-cost fabrication process, can potentially lead to broader applications of our devices for wearable self-powered biomedical devices.

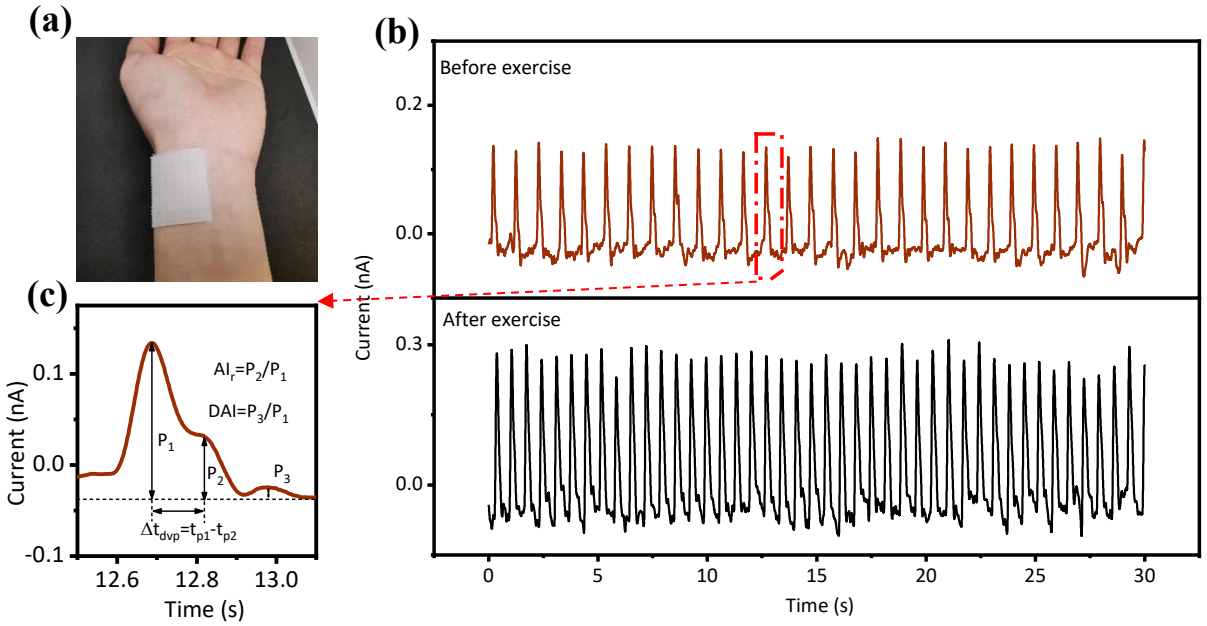

Figure 4.25 TENG sensor attached on human wrist for heart pulse rate monitoring.

4.8 Conclusion

In conclusion, we have successfully prepared a hydrogel-based TENG via a facile 3D printing method, and the inclusion of glycerol would greatly enhance the anti-dehydration properties of the Cu2+-chitosan hydrogel under natural (25 ℃) or even extreme temperatures (60 ℃ or -20 ℃). The 3D printing method offers opportunities to fabricate a device with our desired shapes. The hydrogel works as a good positive triboelectrification layer and continuously deliver voltage and current outputs during contact-separation process. Furthermore, the hydrogel TENG is utilized as a self-powered sensor to detect bio signals as attached to human body. The hydrogel TENG demonstrated here shows great potential for energy harvesting and self-powered physiological monitoring, and opens doors to new technologies in energy, electronics, and sensor applications.

5. 3D PRINTED CONDUCTIVE HYDROGEL FOR RAPID-RESPONSE ELECTRICAL HEATER AND INFRARED CLOAKING

5.1 Introduction

Flexible electric heaters have attracted much attention and caused enormous research interest in recent days, for their wide potential applications in the field of medical device, defogging films, outdoor displays, etc[134-136]. Indium tin oxide(ITO) is a good candidate for the fabrication of electrical heater due to its good conductivity and transparency, but its high cost and lack of flexibility limits its further applications[137]. Recently, there are quite a lot of research reports on the investigation of Ag nanowires, in which the Ag nanowires are generally sprayed onto the surface of fabrics, transparent PET or other polymer substrate for the manufacturing of Ag nanowires-based electrical heater[135, 138-141]. A good Joule heating performance has been demonstrated. However, for this approach, the conductive network only forms at the surface, so it is very fragile to abrasion, corrosion, and other damages. Therefore, it is highly urgent to develop a counterpart for which the whole volume is conductive. For this attempt, Choi et al[134] developed a stretchable heater using Ag nanowires/elastomer nanocomposite for wearable articular thermotherapy, the device shows characteristics of light-weight, high elasticity, superior heating performance. However, for an uniformity of Ag nanowires dispersion in the nanocomposite, the Ag nanowires have to be preprocessed and ligand-exchanged[134], also the whole device fabrication and assembly process is cumbersome as molds are required during the pattern process.

With the advancement of current technologies, additive manufacturing, also called 3D printing, provides a different strategy which make it possible for us to obtain a desired structure from bottom-up method[79, 117]. Among the various 3D printing methods, direct ink writing (DIW), which count on extruding the filament directly through a nozzle by a patterned path and then forming a free-standing 3D structure in a layer-by-layer sequence, have attracted much attention due to its economy and feasibility[11]. A wide variety of devices have been fabricated via DIW methods and their applications in the field of biomedicine[118-119], flexible electronics[120], and actuators[121, 142] have been demonstrated.

Infrared cloaking device also becomes a hot research topic currently. All objects with a surface temperature above absolute zero(-273.15 oC) would emit an electromagnetic radiation, which is proportional to their intrinsic temperature[143]. In general, objects at room temperature emit infrared wavelengths of 8-25 μm, which is invisible to human eyes but can be captured by an infrared camera[144]. Even at night, the infrared camera can still clearly distinguish all the objects in the surrounding environment. Therefore, to make the objects invisible under the detection of infrared camera, it is of great importance to come up with ways to regulate the objects' infrared radiations. Common ways to conceal objects with higher temperatures than their surroundings under IR camera involve two approaches. One is to cover the object with a low-thermal-conductivity film, therefore the outer temperature would be much lower and even similar to the its surrounding environment[145]. However, this approach will cause a heat build-up and increase the temperature inside the hidden area. The second way is to block or lessen the IR radiation emitted from the hot objects. To be more specific, a low-IR-emissivity film is covered over the hot object, as such the majority part of the IR radiation from the inner hot object would be reflected back, only a small amount of IR radiation could be absorbed by the covering film or transmitted out. In such a way, the hot object would look much cooler than its actual temperature. To realize this aim, researchers have attempted several ways including patterning surface micro/nanostructures[146], applying metallic reflectors[147], or building up an assembled colloidal micro or nano-particle three-dimensional arrays over the top surface[148]. All of these methods are beneficial for lessening the IR radiation, but constructing such delicate surface needs much effort, and also these structures are very fragile and can be easily damaged by an external environment. Recently, researchers found that metallic nanowires network could contribute to IR radiation regulation[23], and they already took advantage of this attribute to tune the inside temperature of an area covered by metallic nanowires network[149-150], but its function as infrared stealth and IR camera defeating has not been clearly clarified.

Here we propose a method to prepare a hydrogel-based electric heater via 3D printing process, in which the Ag nanowires are homogeneously dispersed in the nanocomposite system and a good conductivity is achieved. Thanks to the feasibility of 3D printing, it is facile for us to fabricate some stretchable structures which would offer the device much flexibility, stretchability, and conformability to human body. The devices exhibit high electric heating performance, owing to its low-triggering voltage, short-response time, superior cyclability and resistance to a

mechanically stretched ratio up to 50%. In addition, the printed hydrogel composite shows a property of infrared cloaking, as the low-infrared-emissivity Ag nanowires network in the hydrogel system would reflect the majority of the incident infrared light, making the underneath hot objects look cooler or even become invisible under the scope of IR camera.

5.2 Ink preparation and 3D printing for the composite hydrogel fabrication

5.2.1 Preparation of CMC/SA/Ag ink and 3D printing process illustration

Firstly, certain amounts of CMC, SA and Ag nanowires were added and then dissolved DI water in sequence. Then the blend was stirred intensely for nearly 10 mins and then heater at 60 ^{o}C for 30 mins to make sure a complete dissolving.

The schematic shown in Figure 5.1 presented the ink preparation and hydrogel fabrication process. In general, the carboxymethyl cellulose(CMC) and sodium alginate (SA) powers were blended in a certain ratio and then dissolved in DI water. CMC is a high-molecular-weight water-soluble polysaccharide used for viscosity modifier or thickener[151]. SA is a seaweed-extracted naturally derived polysaccharide and has been widely used in bio-printing thanks to its good biocompatibility[152]. Then a certain amount of Ag nanowires were added into the composite. The CMC/SA/Ag composite ink was endowed with a suitable rheological property for the following 3D printing procedure. The experimental setup was presented as in Figure 5.2. In short, the composite ink was firstly loaded into the syringe of a bioprinter. Then the syringe would move along a route which has been carefully designed before. During the syringe movement process, the composite ink would be extruded from the nozzle uniformly and continuously, as there is an internal pressure applied in the syringe. Thanks to desirable rheological properties, the extruded ink would stack in a layer-by-layer sequence and form into a self-supporting three-dimensional structure. The printed object was then transferred into a solution of calcium chloride($CaCl_2$) for the crosslinking purpose.

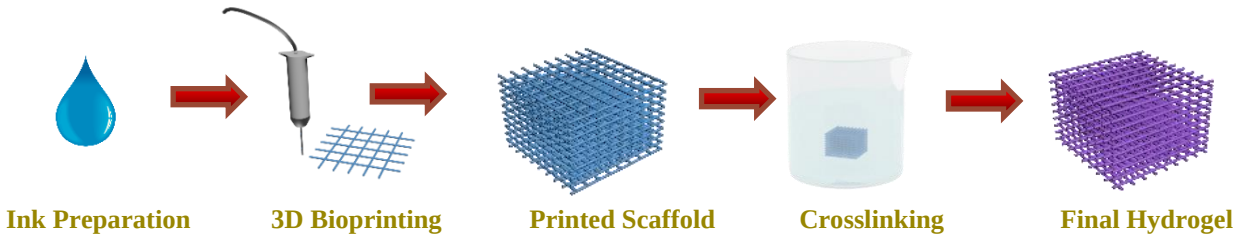

Figure 5.1 Schematic of the 3D printing process for the hydrogel manufacturing.

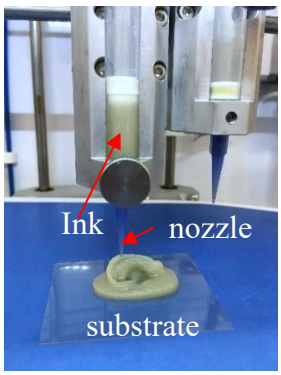

Figure 5.2 Experimental setup of the direct-ink-writing process for the object printing.

5.2.2 Crosslinking mechanism of the hydrogel

In the solution, every Ca^{2+} would form covalent bonds with two carboxylate ions from neighboring CMC or SA chains, in such a way the printed object would be crosslinked into a hydrogel[153], as the schematic shown in Figure 5.3. It is also noted here that the Ag nanowires does not participate the crosslinking process, so the Ag nanowires are simply dispersed and locked in the composite network. This hypothesis has been raised and already confirmed in previous report of a chitosan hydrogel research[154]. Here in the composite, the introduced Ag nanowires would entangle with each other and form a joined network, leading the composite to be conductive correspondingly. Similar approach of using Ag nanowires as conductive fillers in the composite has been taken in previous reports[155].

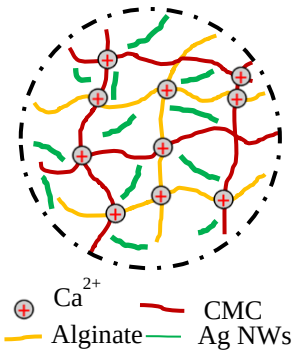

Figure 5.3 Crosslinking mechanism of the CMC/SA/Ag composite hydrogel.

5.2.3 Demonstration of the printed hydrogel film

Figure 5.4 shows the photos of the printed and then crosslinked hydrogel thin films. It can be noted that, a higher Ag nanowires weight percentage in the initial composite ink would be accompanied by a darker as-prepared hydrogel film. Enhancing the hydrogel's conductivity by introducing Ag nanowires would inevitably sacrifice the hydrogel film's transparency. The prepared hydrogel film is pretty flexible and can be bent, twisted, or rolled without any fracture as shown in Figure 5.5.

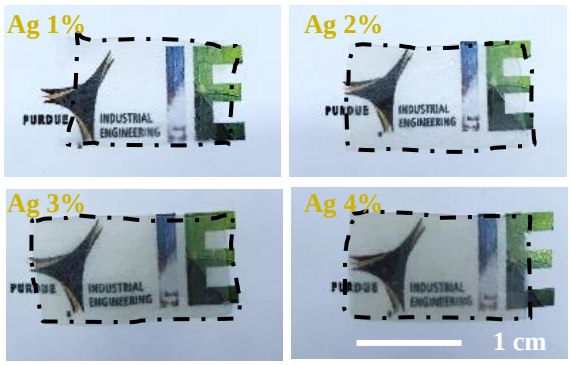

Figure 5.4 Photographs of the CMC/SA/Ag hydrogel with different Ag nanowires amount (wt.%).

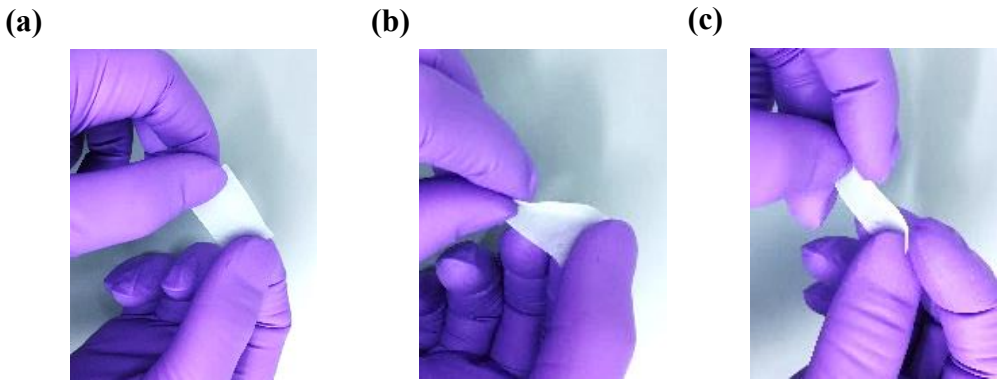

Figure 5.5 Photographs of the hydrogel film (a) original state, (b) twisted, and (c) rolled.

5.3 Materials characterization for the freeze-dried hydrogel

The hydrogel was firstly freeze-dried and then grinded into fine particles. The morphology of the freeze-dried hydrogel was identified by a field-emission scanning electron microscope (Hitachi S-4800 Field Emission SEM). XRD measurement was carried out using a Bruker AXS D8 Advance X-ray diffractometer equipped with a LynxEye 1-dimensional linear Si strip detector. The chemical structures of the films were investigated using a Fourier Transform Infrared Spectrometer (Thermo Nicolet 6700).

The Scanning Electron Microscope(SEM) image of the final hydrogel was presented in Figure 5.6. From that we can find that the freeze-dried hydrogel is with a porous structure, this is easily understood as in hydrogel water matrix would take up the majority space. In order to investigate the hydrogel crosslinking mechanism, Fourier-transform infrared spectroscopy(FTIR) was used and the results are shown in Figure 5.7. For a pure CMC/SA hydrogel with the absence of Ag nanowires, the peak in 3342 cm^{-1} is due to O-H stretching of the non-substituted hydroxyl groups of cellulose, and the band found in 2915 cm^{-1} is caused by C-H stretching and C-O stretching of the ether group of the carboxymethylation of cellulose. The strong band located in 1592 cm^{-1} and 1421 cm^{-1} are assigned to the symmetric and antisymmetric COO stretching vibration of the free carboxylate groups, respectively. Finally, the FTIR bands around 1309 cm^{-1} and 1008 cm^{-1} are referred to C-O stretching C-O-C stretching, respectively, of the saccharide structure. All of the above-mentioned characteristic matches with the information provided in the previous report[156-157]. In addition, it can be seen that, the blending of Ag nanowires into the CMC/SA composite

would not affect the crosslinking mechanism, as the characteristic peaks in the FTIR profiles are not evidently shifted, which is in accordance with our assumption as presented in Figure 5.3[154].

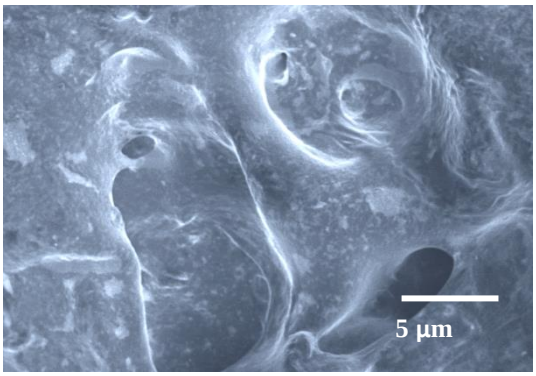

Figure 5.6 SEM images of the freeze-dried hydrogel.

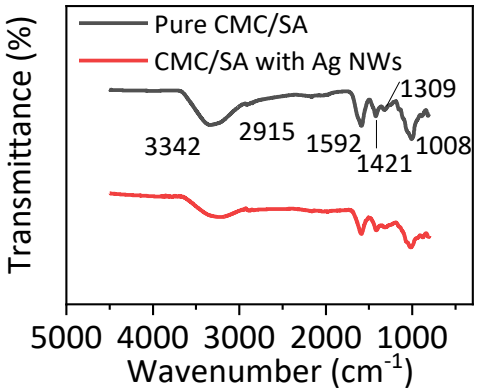

Figure 5.7 FTIR profiles of the CMC/SA and CMC/SA/Ag hydrogel.

5.4 Conductivity measurement of the printed hydrogel pad

Due to the presence of the Ag nanowires, the composite hydrogel film would have a good conductivity. Here we investigated the relation between the sheet resistance of a hydrogel film (thickness ~ 0.5 mm) and its composition. At a constant CMC (8 wt.%) and SA (4 wt.%) concentration, the conductivity of the hydrogel film would increase monotonically with the Ag nanowires amount. From Figure 5.8, it can be seen that the sheet resistance of the film would decrease from ~900 ohm/sq to ~60 ohm/sq when the Ag nanowires concentration varies from 1 wt.% to 4 wt.%.

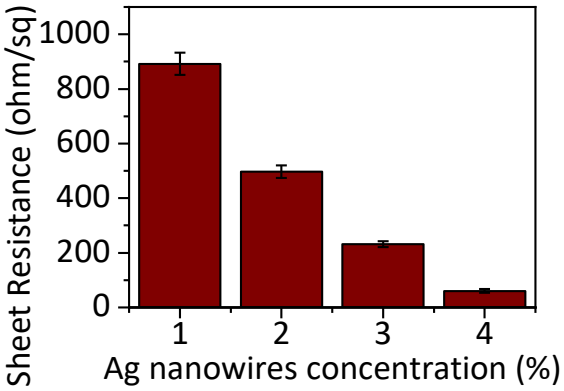

Figure 5.8 Sheet resistance of the CMC/SA/Ag hydrogel with different Ag nanowires amount.

5.5 Rheological properties characterization of the ink pre-gel and printing quality evaluation

5.5.1 Rheological properties characterization of the ink

In Figure 5.1, we have already demonstrated the basic hydrogel printing and crosslinking process, here we continue to investigate some important parameter which may affect the print efficiency. CMC here is working as a thicker agent in the CMC/SA/Ag composite, so its amount would significantly affect the rheological properties of ink and the following printing quality. Rheological properties of the composite ink were measured using a rheometer (Anton Paar MCR 302) with a 40-mm-flate plate geometry a gap of 500 μm. A stress sweep from 0.1 to 500 Pa at constant frequency of 1 Hz was conducted to record the storage and loss modulus variations as function of weep stress. The yield stress was defined as the stress where storage modulus falls to 90% of the plateau value. A strain sweep from 0.1 to 20 s^{-1} was also performed to record the viscosity at varying shear rates.

As shown in Figure 5.9(a) and 5.9(b), with the increase of the CMC amount from 4 wt.% to 10 wt.%, the viscosity and also storage/loss modulus of the composite would go up correspondingly, which means the composite ink would be thicker. It is worth noting that the CMC concentration and Ag nanowires concentration are steadily kept as 4 wt.% here. In Figure 5.9(a), for the inks with different CMC contents, namely 4 wt.%, 6 wt.%, 8 wt.%, 10 wt.%, their viscosities always declines with the shear rate, which means that all of these four inks have shear-thinning properties and can be successfully extruded from the nozzle when a suitable pressure is given[120]. In addition,

in Figure 5.9(b) we find that for all of these four inks, their storage modulus plateau are always higher than their loss modulus plateau, indicating the extruded inks are able to keep a self-supporting structure when they are stacked layer by layer[84]. The information given by Figure 5.9(a) and Figure 5.9(b) implies that all of these inks can be applied for the 3D bioprinting process.

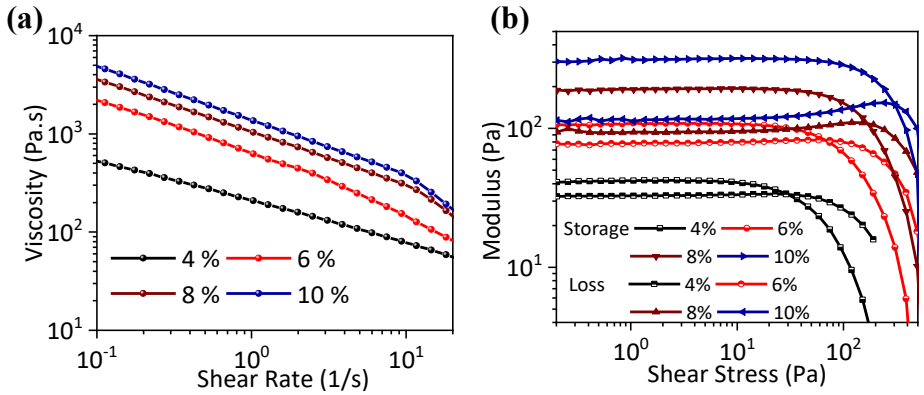

Figure 5.9 (a) Viscosities, (b) Storage/loss modulus of the CMC/SA/Ag ink with different CMC amount (wt.%).

5.5.2 Printing quality evaluation

We then tested the printability of the four inks with different CMC content. A grid-like structure was designed as the one shown in Figure 5.10, then CMC/SA/Ag composite inks with different CMC content were applied for this structure realization, and the printing results are shown in Figure 5.11. Along the structure's diagonal direction, we would get several squares with the size ranging from 1 x 1, 2 x 2, 3 x 3, to 4 x 4, 5 x 5 mm. The square was designed to be perfect as shown in Figure 5.12(a), but in real situation due to the diffusion of the extruded ink, the shape of square would be irregular and its actual area(Aa) would be smaller than the theoretical area (At), as shown in Figure 5.12(b). Here we define a notion diffusion rate (Dfr), which can be expressed by (At - Aa) / At * 100%, to measure the printability of these four inks. Obviously, the more viscous of the ink, the less it would diffuse, and the lower Dfr it would have. In Figure 5.11, it can be found that with the increase of the CMC content increase, the printed line width would be smaller and the structure would have a sharper edge. Figure 5.12(c) illustrated the relation between the diffusion rate and the CMC content in the composite ink. At every pore size, the diffusion rate of lower-CMC-content ink would be always higher than larger-CMC-content ink. Besides, with the increase of the pore size, the diffusion rate would rapidly decline, and for a 5 x 5 mm square,

the Dfrs of all four inks are all around or even below 10%. This is because for a large square, the diffusion distance of the ink would become negligible when compared with the side length of the square. In order to realize a higher resolution for our 3D printing process, in the following context, the composition of the ink is set as 10 wt.% CMC + 4 wt.% SA + 4 wt.% Ag nanowires.

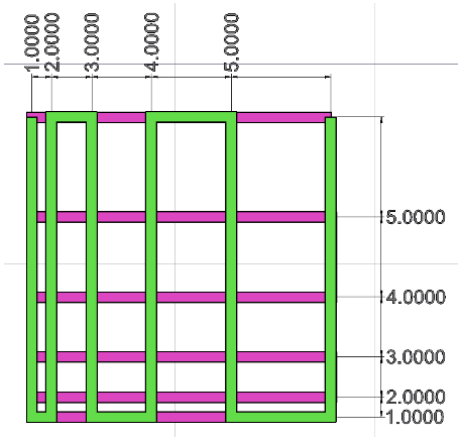

Figure 5.10 Designed grid for printing realization.

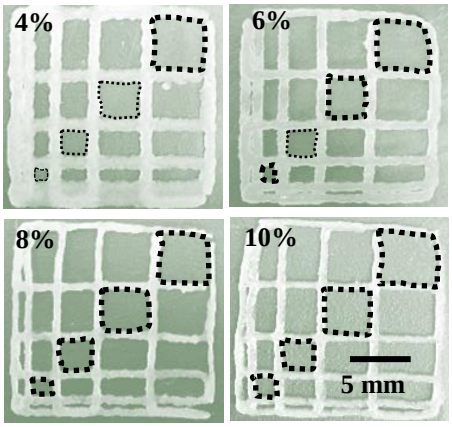

Figure 5.11 Photographs of the printed grid structure using CMC/SA/Ag ink with different CMC amount.

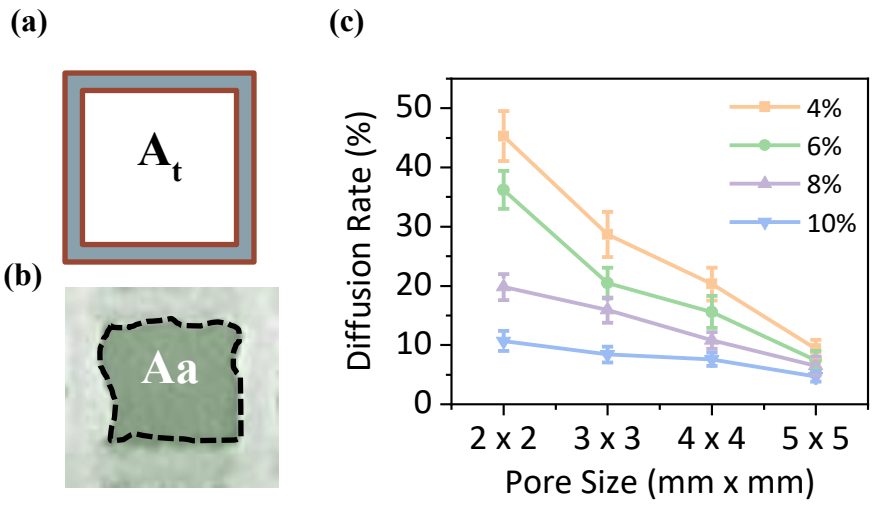

Figure 5.12 (a) Theoretical shape of the printed grid; (b) Actual shape of the printed grid; (c) Diffusion rate of the CMC/SA/Ag ink as a function of the ink composition and the grid size length.

5.5.3 Demonstration of the three-dimensional objects printed with CMC/SA/Ag hydrogel

Here we printed an ear-like structure and an octopus-like structure, further proving the good printability of the CMC/SA/Ag composite ink (Figure 5.13(a) and Figure 5.13(b)). These 3D structures may help find applications in the biomedical field like tissue engineering, implantable organs.

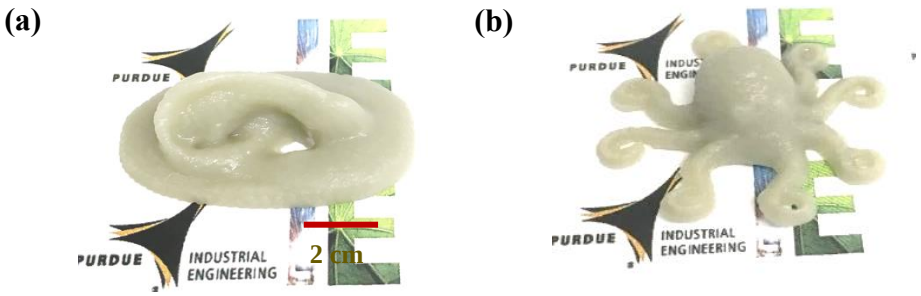

Figure 5.13 Octopus-like structures printed using the CMC/SA/Ag ink. The concentration of SA and Ag nanowires, CMC are 4%, 4%, and 8%, respectively. The concentration of SA and Ag nanowires, CMC are 4%, 4%, and 8%, respectively.

5.6 Electrical heater performance of the hydrogel pad

The conductive hydrogel here was connected in an electric circuit and it could be seen that a LED could be lighted on (Figure 5.14). The IR images were obtained by an IR camera (FLIR-E6390).

The temperatures were measured by a thermocouple (OMEGA H911T). Devices' resistances were recorded and calculated by a function generator (Stanford DS345) and a current amplifier (Stanford SR570).

Figure 5.14 conductivity validation of the hydrogel pad by connecting it in a circuit with LED light.

5.6.1 Mechanism for the hydrogel working as electrical heater

We then evaluated the heating performance with a typical CMC/SA/Ag hydrogel part which has dimensions of 2 x 2 cm excluding the width of the Cu tapes, and its sheet resistance here is ~60 ohm/sq. A voltage was applied onto the two ends of the Cu tape electrodes, due to the Joule heating effect, the applied voltage would cause the temperature of the hydrogel part to be increased as the electric energy is converted to thermal energy here, as the schematic illustrated in Figure 5.15.

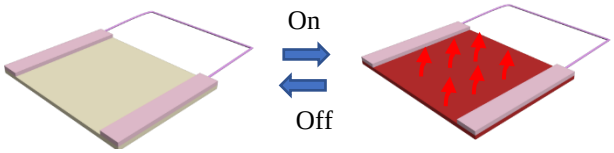

Figure 5.15 Illustration for the heating and cooling cycles of the electrical heaters.

5.6.2 Basic heating performance of the hydrogel heater device

Figure 5.16 shows the photographs of the hydrogel pad captured by an IR camera. At the initial moment, the temperature of the hydrogel pad is around is around 20 ℃, very close to the environment temperature in our experiment (21 ℃). Then we connect the hydrogel pad with an external circuit and load a 5V voltage, the temperature of it would quickly rise, final it would reach to a steady plateau after a certain time (~ 60 s).

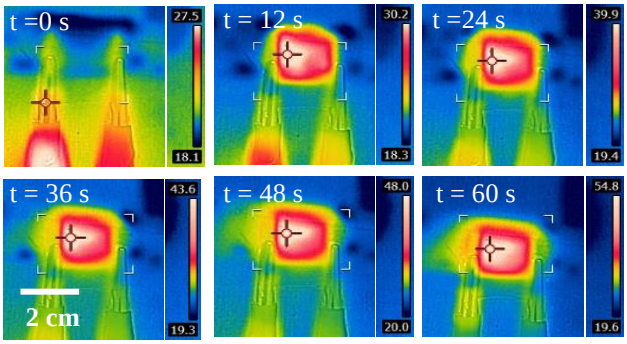

Figure 5.16 Change of the IR images of a hydrogel pad captured by an IR camera when a voltage of 5V is applied.

In Figure 5.17 we found that a higher voltage applied would leads the hydrogel pad to have a faster temperature increase rate and a higher steady-state temperature (ultimate temperature), generally the ultimate temperature would be reached within one minute.

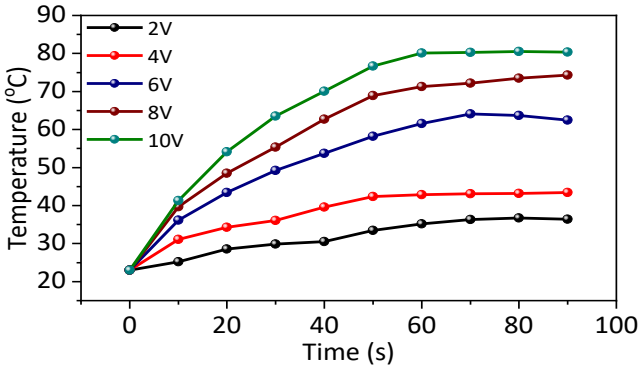

Figure 5.17 Temperature variance of the hydrogel when different voltage is applied onto it.

5.6.3 Cyclability and stability of the hydrogel heater device

We also tested the cyclic performance of the hydrogel pad as a heater and the results are shown in Figure 5.18. Every time once the voltage is applied, the temperature would reach to its maximum within a minute, and then after we revoke the applied voltage, it would get back to its original state. This process is repeated for several times and we have not found any noticeable heating performance decline, which is a good sign for proving its long-term-use stability. In addition, the hydrogel pad is flexible and can bent, rolled, or twisted into different forms, but its heating performance would not be negatively affected since the maximum temperature would always keep steady, just as illustrated in Figure 5.18(b).

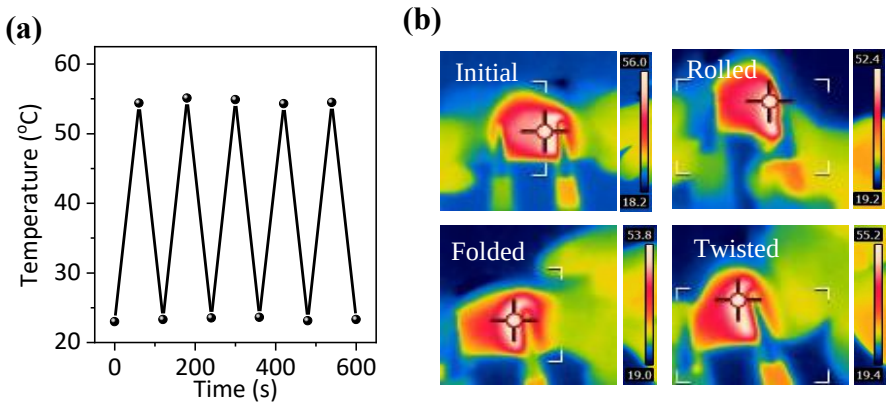

Figure 5.18 (a) Temperature of the hydrogel when the voltage is applied and revoked repeatedly, applied voltage is 5V. (b) IR images of hydrogel at its original state, and then rolled, folded and twisted, applied voltage is 5V.

5.6.4 Performance evaluation for a 3D printed hydrogel heater with serpentine structure

Thanks to the feasibility of 3D printing, we can easily process our hydrogel into various shapes adaptable for use in different scenarios. In order to maximize the system-level softness, we adopt fully serpentine mesh design as shown in Figure 5.19. The serpentine designs are widely used in stretchable electronics as it can provide a higher stretchability when compared to flat plain ones[158].

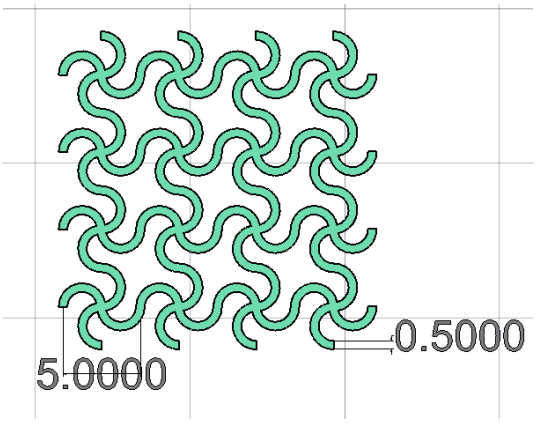

Figure 5.19 Designed serpentine structure for stretchable electronics.

Figure 5.20 showed the printed serpentine structure using CMC/SA/Ag hydrogel as constituents , and it is clearly seen that the device can be stretched in bi-directions.

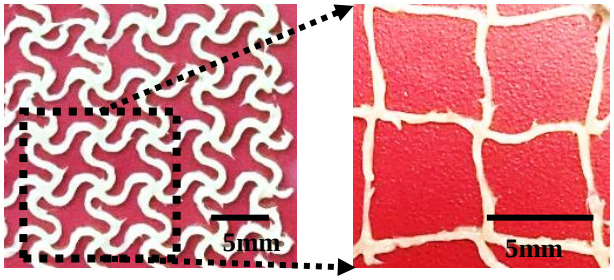

Figure 5.20 Photographs of the printed hydrogel with serpentine structure for initial state and bi-stretched state.

As the device has a superior in-plane stretchability, its resistance change would be very minimal when applied with a strain up to 60% (Figure 5.21(a)). In contrast, for a flat design, the resistance would rapidly increase by several times of its original value when subject to a small strain, also the flat-design device is susceptible to the external strain and it would be snapped at a strain of ~ 10%. The serpentine-mesh device also showed a superior heating performance once an external voltage was triggered, and more interestingly, its heating performance would not be significantly influenced at a stretched state, which was confirmed in Figure 5.21(b). When applied with a certain voltage and coupled with strain from 0 to 60%, its maximum temperature can always be kept at a constant value and no obvious decline had been found.

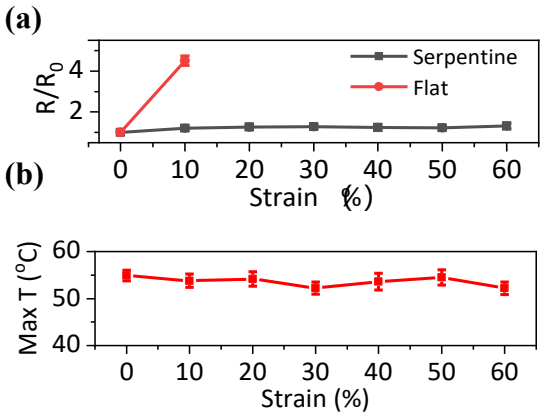

Figure 5.21 (a) Resistance change of the hydrogel with flat structure or serpentine structure as a function of stretch ratio. (g) Max temperature change of the hydrogel with flat structure or serpentine structure as a function of stretch ratio.

Figure 5.22 were the IR images of our device when applied with a certain voltage at original state and stretched states, respectively. Cyclic stability of the device was also proven as shown in Figure

5.23, even after repetitive stretch-releasing cycles for over 3000 times, the device's resistance and maximum temperature upon certain voltage triggering would not shift too much.

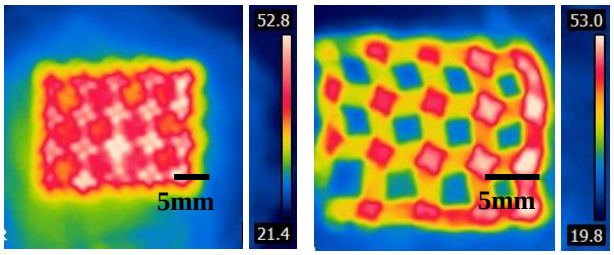

Figure 5.22 IR image of the serpentine-structure device for initial state and bi-stretched state.

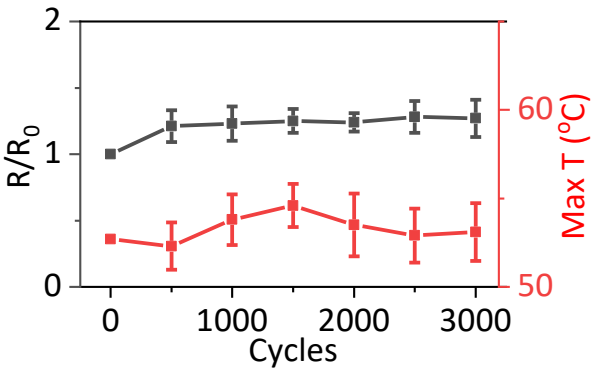

Figure 5.23 Cyclic performance of the device under stretch/release cycles for over 3000 times.

5.6.5 Application as wearable device for the hydrogel heater

Thanks to device's high stretchability, it can be used as a wearable device. Here we attached our device onto a human wrist, and we could find that the device would be able to strongly conform to human body, after voltage triggering the device's temperature would be increased to a certain value which is dependent on the applied voltage (Figure 5.24). As such, our device may find wide application in stretchable and adaptable human-integrated therapeutic electronics.

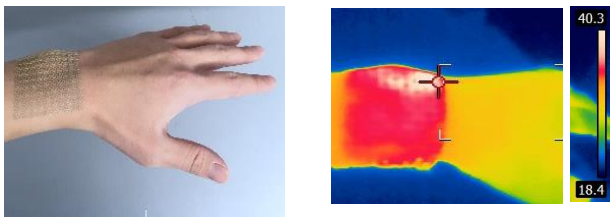

Figure 5.24 IR images of the device as it is conformed to a human wrist and applied with a voltage of 4V.

5.7 IR cloaking performance of the hydrogel pad

5.7.1 5.7.1 Mechanism for the IR cloaking of the hydrogel pad

Due to the abundant existence of Ag nanowires in the CMC/SA/Ag composites, the hydrogel pad might also be able to work as an infrared stealth device. The mechanism was shown in Figure 5.25. For an hot object, it would automatically emit infrared radiations to the surrounding environment, when the infrared radiation reaches to the hydrogel film, due to the high reflectivity of the Ag nanowires network, the majority of the IR radiation would be blocked and reflected back, only a small part of it can be absorbed by the hydrogel pads or transmitted out. This mechanism has also been illustrated in previous reports[23].

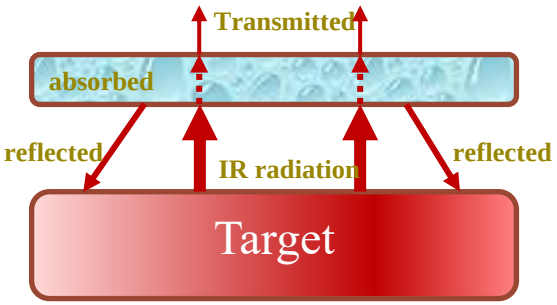

Figure 5.25 Schematic of the IR cloaking mechanism for the hydrogel pad.

5.7.2 Measurement of the IR transmittance of the hydrogel pad

Here we test the transmittance of the hydrogel pad for wavelengths ranging from 2 to 12 μm, it can be seen from Figure 5.26 that with the increase of hydrogel pad thickness, the transmittance of mid-infrared radiation would decrease correspondingly, which indicates that a thicker hydrogel pad would reflect more IR radiation.

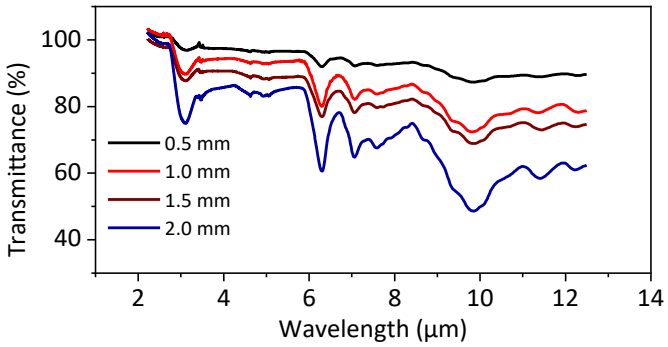

Figure 5.26 IR transmittance of the hydrogel pad with different thickness for the infrared wavelength from 2 to 12 μm.

5.7.3 Basic evaluation for the IR cloaking performance of the hydrogel pad

Figure 5.27 showed the IR images of hydrogel pads with different thickness and being put in a hot plate with a surface temperature of ~35 ^{o}C, since the hydrogel pad would reflect a portion of IR radiation and less IR would be capture by the IR camera, the part covered by the hydrogel pad would look cooler than the surrounding environment. Higher hydrogel pad thickness is accompanied by a stronger IR reflectance, so a larger as-seen temperature difference between the hydrogel pad and surroundings will be noticed. As such, the low thermal conductivity coupled with the high IR reflectivity would offer the hydrogel pad with a strong ability of IR cloaking.

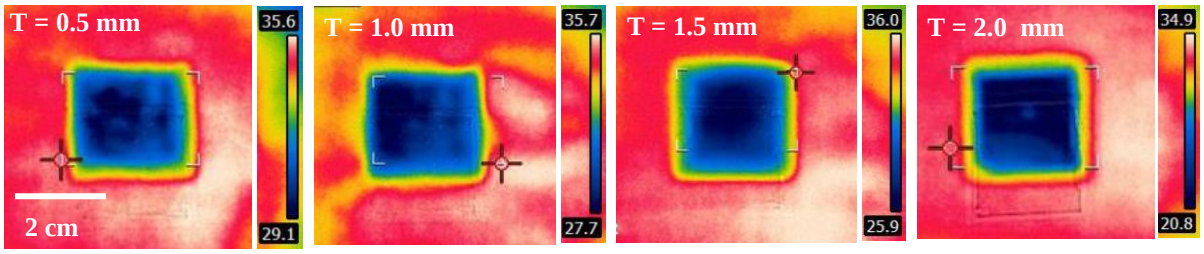

Figure 5.27 IR images of the hydrogel with different thickness on top of a hot plate with a constant temperature of 36 ^{o}C.

5.7.4 Application demonstration of the hydrogel pad as an IR cloaking device

We further conformed our hydrogel pad onto human wrist, and from Figure 5.28 we find that the part of human body covered by hydrogel would looks the same as the surrounding environment, which means that it is almost invisible under IR camera. Figure 5e showed a car model's IR image,

clearly the part covered by hydrogel pad would be invisible under IR camera as the radiation is mostly reflected.

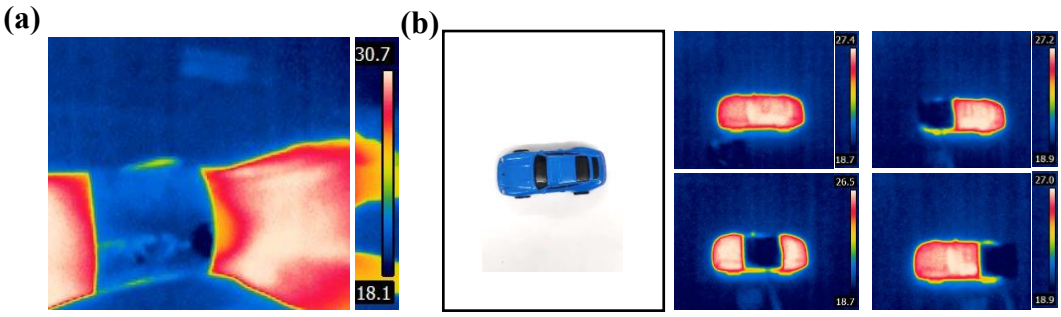

Figure 5.28 (a) IR images of human wrist when it is covered with a hydrogel pad, thickness here is 2 mm. (b) IR images of car model and when its different part is covered by a hydrogel pad, thickness here is 2 mm.

5.8 Conclusion

In conclusion, here in our study we fabricate a conductive hydrogel via a direct-ink printing way. The hydrogel can work as an electric heater due to its good conductivity. Great responsiveness, cyclic stability are demonstrated here. Thanks to the advantage of 3D printing, we design and fabricate some serpentine mesh device using the conductive hydrogel as constituents, and also find its application in stretchable human-integrated therapeutic electronics. The hydrogel also shows superior IR reflection property, is expected to be applicable in the wearable IR stealth technology in the future toward concealing people and objects from IR thermography cameras.

6. SUMMARY

In this dissertation, we firstly explored a new class of piezoelectric material, selenium nanowires, and systematically investigated the origin of the piezoelectricity as well as developed a facile device fabrication method via LB assembly. The piezoelectric properties of the selenium nanowires have been characterized detailed, and also its application for human-integrated applications have been illustrated like for gesture recognition and cardiovascular health status monitoring.

In the next part (chapter 3), we further implemented the state-of-the-art additive manufacturing into the piezoelectric device fabrication, the results delivered shows that manufacturing process of piezoelectric devices have been greatly simplified, which might pave a way for the future large-scale fabrication and application of piezoelectric devices. Combined with the machine learning method, it has been demonstrated that the piezoelectric devices could be effective in working as wearable sensors and collecting psychological signals, the data collected can be used for monitoring the wearer's motion state.

Then in chapter 4, we applied the hydrogel material as the triboelectric sensing layer, and the chitosan hydrogel layer was shown to be a good candidate as the triboelectrically positive material, which can effectively harvest the ambient mechanical energy and transfer it to electricity. Direct-ink-writing, one kind of the 3D printing method, has been involved in the device fabrication process, and could contribute to the optimization of the device performance. Besides that, our hydrogel device has a capacity of long-lasting moisture maintenance and extreme temperature tolerance, which would be extremely useful for the device's application in real-environment.

In chapter 5, we further extended the DIW method for the fabrication of a composite hydrogel which is capable of realizing an electricity-induced heating and infrared cloaking. The 3D printing method allows us to fabricate arbitrary, sophisticated device structures which greatly enhanced the stretchability, the conductive hydrogel with Ag nanowires as the filler could effectively work as an electric heater, and also the low emissivity of Ag nanowires would help the device shield a majority of the incoming infrared emission and help defeat the IR camara.

REFERENCES

1. Wang, Z. L.; Song, J., Piezoelectric nanogenerators based on zinc oxide nanowire arrays. *Science* **2006,** *312* (5771), 242-246.

2. Zheng, Q.; Shi, B.; Li, Z.; Wang, Z. L., Recent progress on piezoelectric and triboelectric energy harvesters in biomedical systems. *Advanced Science* **2017,** *4* (7), 1700029.

3. Fan, F.-R.; Tian, Z.-Q.; Wang, Z. L., Flexible triboelectric generator. *Nano energy* **2012,** *1* (2), 328-334.

4. Fan, F. R.; Tang, W.; Wang, Z. L., Flexible nanogenerators for energy harvesting and self-powered electronics. *Advanced Materials* **2016,** *28* (22), 4283-4305.

5. Wang, Z. L., On Maxwell's displacement current for energy and sensors: the origin of nanogenerators. *Materials Today* **2017,** *20* (2), 74-82.

6. Wang, Z. L., Triboelectric nanogenerators as new energy technology for self-powered systems and as active mechanical and chemical sensors. *ACS nano* **2013,** *7* (11), 9533-9557.

7. Wang, S.; Lin, L.; Wang, Z. L., Triboelectric nanogenerators as self-powered active sensors. *Nano Energy* **2015,** *11*, 436-462.

8. Li, Z.; Zheng, Q.; Wang, Z. L.; Li, Z., Nanogenerator-Based Self-Powered Sensors for Wearable and Implantable Electronics. *Research* **2020,** *2020*, 8710686.

9. Wang, H.; Cheng, J.; Wang, Z.; Ji, L.; Wang, Z. L., Triboelectric nanogenerators for human-health care. *Science Bulletin* **2020**.

10. Ligon, S. C.; Liska, R.; Stampfl, J. r.; Gurr, M.; Mülhaupt, R., Polymers for 3D printing and customized additive manufacturing. *Chemical reviews* **2017,** *117* (15), 10212-10290.

11. Lewis, J. A., Direct ink writing of 3D functional materials. *Advanced Functional Materials* **2006,** *16* (17), 2193-2204.

12. Awad, A.; Fina, F.; Goyanes, A.; Gaisford, S.; Basit, A. W., 3D printing: Principles and pharmaceutical applications of selective laser sintering. *International Journal of Pharmaceutics* **2020,** *586*, 119594.

13. Huang, J.; Qin, Q.; Wang, J., A Review of Stereolithography: Processes and Systems. *Processes* **2020,** *8* (9), 1138.

14. Pidge, P. A.; Kumar, H., Additive manufacturing: A review on 3 D printing of metals and study of residual stress, buckling load capacity of strut members. *Materials Today: Proceedings* **2020,** *21*, 1689-1694.

15. Mazzanti, V.; Malagutti, L.; Mollica, F., FDM 3D printing of polymers containing natural fillers: A review of their mechanical properties. *Polymers* **2019,** *11* (7), 1094.

16. Yuk, H.; Lu, B.; Lin, S.; Qu, K.; Xu, J.; Luo, J.; Zhao, X., 3D printing of conducting polymers. *Nature communications* **2020,** *11* (1), 1-8.

17. Lin, K.; Sheikh, R.; Romanazzo, S.; Roohani, I., 3D printing of bioceramic scaffolds—barriers to the clinical translation: from promise to reality, and future perspectives. *Materials* **2019,** *12* (17), 2660.

18. Yuk, H.; Lu, B.; Zhao, X., Hydrogel bioelectronics. *Chemical Society Reviews* **2019,** *48* (6), 1642-1667.

19. Fu, F.; Wang, J.; Zeng, H.; Yu, J., Functional Conductive Hydrogels for Bioelectronics. *ACS Materials Letters* **2020,** *2* (10), 1287-1301.

20. Barry III, R. A.; Shepherd, R. F.; Hanson, J. N.; Nuzzo, R. G.; Wiltzius, P.; Lewis, J. A., Direct-write assembly of 3D hydrogel scaffolds for guided cell growth. *Advanced materials* **2009,** *21* (23), 2407-2410.

21. Chen, C.; Ye, C., Metal Nanowires. *Transparent Conductive Materials: Materials, Synthesis, Characterization, Applications* **2018**, 105-131.

22. Hong, S.; Lee, H.; Lee, J.; Kwon, J.; Han, S.; Suh, Y. D.; Cho, H.; Shin, J.; Yeo, J.; Ko, S. H., Highly stretchable and transparent metal nanowire heater for wearable electronics applications. *Advanced materials* **2015,** *27* (32), 4744-4751.

23. Hsu, P.-C.; Liu, X.; Liu, C.; Xie, X.; Lee, H. R.; Welch, A. J.; Zhao, T.; Cui, Y., Personal thermal management by metallic nanowire-coated textile. *Nano letters* **2015,** *15* (1), 365-371.

24. Huang, C.-T.; Song, J.; Lee, W.-F.; Ding, Y.; Gao, Z.; Hao, Y.; Chen, L.-J.; Wang, Z. L., GaN nanowire arrays for high-output nanogenerators. *Journal of the American Chemical Society* **2010,** *132* (13), 4766-4771.

25. Lin, L.; Lai, C.-H.; Hu, Y.; Zhang, Y.; Wang, X.; Xu, C.; Snyder, R. L.; Chen, L.-J.; Wang, Z. L., High output nanogenerator based on assembly of GaN nanowires. *Nanotechnology* **2011,** *22* (47), 475401.

26. Minary-Jolandan, M.; Bernal, R. A.; Kuljanishvili, I.; Parpoil, V.; Espinosa, H. D., Individual GaN nanowires exhibit strong piezoelectricity in 3D. *Nano letters* **2012,** *12* (2), 970-976.

27. Lin, Y.-F.; Song, J.; Ding, Y.; Lu, S.-Y.; Wang, Z. L., Piezoelectric nanogenerator using CdS nanowires. *Applied Physics Letters* **2008,** *92* (2), 022105.

28. Lin, Y. F.; Song, J.; Ding, Y.; Lu, S. Y.; Wang, Z. L., Alternating the output of a CdS nanowire nanogenerator by a white-light-stimulated optoelectronic effect. *Advanced Materials* **2008,** *20* (16), 3127-3130.

29. Park, K.-I.; Xu, S.; Liu, Y.; Hwang, G.-T.; Kang, S.-J. L.; Wang, Z. L.; Lee, K. J., Piezoelectric BaTiO3 Thin Film Nanogenerator on Plastic Substrates. *Nano Letters* **2010,** *10* (12), 4939-4943.

30. Shin, S.-H.; Kim, Y.-H.; Lee, M. H.; Jung, J.-Y.; Nah, J., Hemispherically aggregated BaTiO3 nanoparticle composite thin film for high-performance flexible piezoelectric nanogenerator. *ACS nano* **2014,** *8* (3), 2766-2773.

31. Zhang, G.; Liao, Q.; Zhang, Z.; Liang, Q.; Zhao, Y.; Zheng, X.; Zhang, Y., Novel Piezoelectric Paper-Based Flexible Nanogenerators Composed of BaTiO3 Nanoparticles and Bacterial Cellulose. *Advanced Science* **2016,** *3* (2), 1500257.

32. Zhang, M.; Gao, T.; Wang, J.; Liao, J.; Qiu, Y.; Xue, H.; Shi, Z.; Xiong, Z.; Chen, L., Single BaTiO3 nanowires-polymer fiber based nanogenerator. *Nano Energy* **2015,** *11*, 510-517.

33. Wu, J. M.; Xu, C.; Zhang, Y.; Wang, Z. L., Lead-Free Nanogenerator Made from Single ZnSnO3 Microbelt. *ACS Nano* **2012,** *6* (5), 4335-4340.

34. Alam, M. M.; Ghosh, S. K.; Sultana, A.; Mandal, D., Lead-free ZnSnO3/MWCNTs-based self-poled flexible hybrid nanogenerator for piezoelectric power generation. *Nanotechnology* **2015,** *26* (16), 165403.

35. Lee, K. Y.; Kim, D.; Lee, J. H.; Kim, T. Y.; Gupta, M. K.; Kim, S. W., Unidirectional High-Power Generation via Stress-Induced Dipole Alignment from ZnSnO3 Nanocubes/Polymer Hybrid Piezoelectric Nanogenerator. *Advanced Functional Materials* **2014,** *24* (1), 37-43.

36. Wu, M.; Zheng, T.; Zheng, H.; Li, J.; Wang, W.; Zhu, M.; Li, F.; Yue, G.; Gu, Y.; Wu, J., High-performance piezoelectric-energy-harvester and self-powered mechanosensing using lead-free potassium–sodium niobate flexible piezoelectric composites. *Journal of Materials Chemistry A* **2018,** *6* (34), 16439-16449.

37. Huan, Y.; Zhang, X.; Song, J.; Zhao, Y.; Wei, T.; Zhang, G.; Wang, X., High-performance piezoelectric composite nanogenerator based on Ag/(K,Na)NbO3 heterostructure. *Nano Energy* **2018,** *50*, 62-69.

38. Chang, C.; Tran, V. H.; Wang, J.; Fuh, Y.-K.; Lin, L., Direct-Write Piezoelectric Polymeric Nanogenerator with High Energy Conversion Efficiency. *Nano Letters* **2010,** *10* (2), 726-731.

39. Cha, S.; Kim, S. M.; Kim, H.; Ku, J.; Sohn, J. I.; Park, Y. J.; Song, B. G.; Jung, M. H.; Lee, E. K.; Choi, B. L.; Park, J. J.; Wang, Z. L.; Kim, J. M.; Kim, K., Porous PVDF As Effective Sonic Wave Driven Nanogenerators. *Nano Letters* **2011,** *11* (12), 5142-5147.

40. Lee, M.; Chen, C. Y.; Wang, S.; Cha, S. N.; Park, Y. J.; Kim, J. M.; Chou, L. J.; Wang, Z. L., A hybrid piezoelectric structure for wearable nanogenerators. *Advanced Materials* **2012,** *24* (13), 1759-1764.

41. Qi, Y.; Jafferis, N. T.; Lyons Jr, K.; Lee, C. M.; Ahmad, H.; McAlpine, M. C., Piezoelectric ribbons printed onto rubber for flexible energy conversion. *Nano letters* **2010,** *10* (2), 524-528.

42. Hu, Y.; Zhang, Y.; Xu, C.; Zhu, G.; Wang, Z. L., High-output nanogenerator by rational unipolar assembly of conical nanowires and its application for driving a small liquid crystal display. *Nano letters* **2010,** *10* (12), 5025-5031.

43. Nguyen, V.; Zhu, R.; Jenkins, K.; Yang, R., Self-assembly of diphenylalanine peptide with controlled polarization for power generation. *Nature Communications* **2016,** *7*, 13566.

44. Hu, Y.; Zhang, Y.; Xu, C.; Lin, L.; Snyder, R. L.; Wang, Z. L., Self-powered system with wireless data transmission. *Nano letters* **2011,** *11* (6), 2572-2577.

45. Wang, X., Piezoelectric nanogenerators—Harvesting ambient mechanical energy at the nanometer scale. *Nano Energy* **2012,** *1* (1), 13-24.

46. Hansen, B. J.; Liu, Y.; Yang, R.; Wang, Z. L., Hybrid Nanogenerator for Concurrently Harvesting Biomechanical and Biochemical Energy. *ACS Nano* **2010,** *4* (7), 3647-3652.

47. Hu, Y.; Wang, Z. L., Recent progress in piezoelectric nanogenerators as a sustainable power source in self-powered systems and active sensors. *Nano Energy* **2015,** *14*, 3-14.

48. Cherin, P.; Unger, P., The crystal structure of trigonal selenium. *Inorganic Chemistry* **1967,** *6* (8), 1589-1591.

49. Mayers, B. T.; Liu, K.; Sunderland, D.; Xia, Y., Sonochemical Synthesis of Trigonal Selenium Nanowires. *Chemistry of Materials* **2003,** *15* (20), 3852-3858.

50. Wang, Z.; Wang, L.; Wang, H., PEG-Mediated Hydrothermal Growth of Single-Crystal Tellurium Nanotubes. *Crystal Growth & Design* **2008,** *8* (12), 4415-4419.

51. Li, Z.; Zheng, S.; Zhang, Y.; Teng, R.; Huang, T.; Chen, C.; Lu, G., Controlled synthesis of tellurium nanowires and nanotubes via a facile, efficient, and relatively green solution phase method. *Journal of Materials Chemistry A* **2013,** *1* (47), 15046-15052.

52. Lee, T. I.; Lee, S.; Lee, E.; Sohn, S.; Lee, Y.; Lee, S.; Moon, G.; Kim, D.; Kim, Y. S.; Myoung, J. M.; Wang, Z. L., High-Power Density Piezoelectric Energy Harvesting Using Radially Strained Ultrathin Trigonal Tellurium Nanowire Assembly. *Advanced Materials* **2013,** *25* (21), 2920-2925.

53. Junginger, H. G., Electronic band structure of tellurium. *Solid State Communications* **1967,** *5* (7), 509-511.

54. Reitz, J. R., Electronic Band Structure of Selenium and Tellurium. *Physical Review* **1957,** *105* (4), 1233-1240.

55. Kumar, S., Synthesis and characterisation of selenium nanowires using template synthesis. *Journal of Experimental Nanoscience* **2009,** *4* (4), 341-346.

56. Royer, D.; Dieulesaint, E., Elastic and piezoelectric constants of trigonal selenium and tellurium crystals. *Journal of Applied Physics* **1979,** *50* (6), 4042-4045.

57. Gao, S.; Wang, Y.; Wang, R.; Wu, W., Piezotronic effect in 1D van der Waals solid of elemental tellurium nanobelt for smart adaptive electronics. *Semiconductor Science and Technology* **2017,** *32* (10), 104004.

58. Bae, S.; Kim, H.; Lee, Y.; Xu, X.; Park, J.-S.; Zheng, Y.; Balakrishnan, J.; Lei, T.; Kim, H. R.; Song, Y. I., Roll-to-roll production of 30-inch graphene films for transparent electrodes. *Nature nanotechnology* **2010,** *5* (8), 574.

59. Xie, Q.; Dai, Z.; Huang, W.; Zhang, W.; Ma, D.; Hu, X.; Qian, Y., Large-scale synthesis and growth mechanism of single-crystal Se nanobelts. *Crystal growth & design* **2006,** *6* (6), 1514-1517.

60. Xu, F.; Zhu, Y., Highly Conductive and Stretchable Silver Nanowire Conductors. *Advanced Materials* **2012,** *24* (37), 5117-5122.

61. Niu, S.; Wang, Z. L., Theoretical systems of triboelectric nanogenerators. *Nano Energy* **2015,** *14*, 161-192.

62. He, X.; Zi, Y.; Guo, H.; Zheng, H.; Xi, Y.; Wu, C.; Wang, J.; Zhang, W.; Lu, C.; Wang, Z. L., A Highly Stretchable Fiber-Based Triboelectric Nanogenerator for Self-Powered Wearable Electronics. *Advanced Functional Materials* **2017,** *27* (4), 1604378.

63. Chen, X.; Parida, K.; Wang, J.; Xiong, J.; Lin, M.-F.; Shao, J.; Lee, P. S., A Stretchable and Transparent Nanocomposite Nanogenerator for Self-Powered Physiological Monitoring. *ACS applied materials & interfaces* **2017,** *9* (48), 42200-42209.

64. Bouat, J.; Thuillier, J., Electromechanical resonance in selenium determination of the piezoelectric coefficient d11. *Physics Letters A* **1971,** *37* (1), 71-72.

65. Shiosaki, T.; Kawabata, A.; Tanaka, T., Piezoelectric Properties of Se Film Deposited on Te Crystal. *Japanese Journal of Applied Physics* **1970,** *9* (6), 631.

66. Kunigelis, V.; Royer, D.; Dieulesaint, E.; Thuillier, J., Determination of the piezoelectric constant d14 of trigonal selenium crystals. *Physics Letters A* **1976,** *56* (4), 331-332.

67. Yang, R.; Qin, Y.; Li, C.; Zhu, G.; Wang, Z. L., Converting biomechanical energy into electricity by a muscle-movement-driven nanogenerator. *Nano Letters* **2009,** *9* (3), 1201-1205.

68. Wang, Z. L.; Wu, W., Nanotechnology-enabled energy harvesting for self-powered micro-/nanosystems. *Angewandte Chemie International Edition* **2012,** *51* (47), 11700-11721.

69. Pradel, K. C.; Wu, W.; Ding, Y.; Wang, Z. L., Solution-derived ZnO homojunction nanowire films on wearable substrates for energy conversion and self-powered gesture recognition. *Nano letters* **2014,** *14* (12), 6897-6905.

70. Schwartz, G.; Tee, B. C.-K.; Mei, J.; Appleton, A. L.; Kim, D. H.; Wang, H.; Bao, Z., Flexible polymer transistors with high pressure sensitivity for application in electronic skin and health monitoring. *Nature communications* **2013,** *4*, 1859.

71. Park, J.; Kim, M.; Lee, Y.; Lee, H. S.; Ko, H., Fingertip skin–inspired microstructured ferroelectric skins discriminate static/dynamic pressure and temperature stimuli. *Science advances* **2015,** *1* (9), e1500661.

72. Avolio, A. P.; Butlin, M.; Walsh, A., Arterial blood pressure measurement and pulse wave analysis—their role in enhancing cardiovascular assessment. *Physiological measurement* **2009,** *31* (1), R1.

73. Lin, Z.; Chen, J.; Li, X.; Zhou, Z.; Meng, K.; Wei, W.; Yang, J.; Wang, Z. L., Triboelectric nanogenerator enabled body sensor network for self-powered human heart-rate monitoring. *ACS nano* **2017,** *11* (9), 8830-8837.

74. Nichols, W. W., Clinical measurement of arterial stiffness obtained from noninvasive pressure waveforms. *American journal of hypertension* **2005,** *18* (S1), 3S-10S.

75. Saba, P. S.; Roman, M. J.; Pini, R.; Spitzer, M.; Ganau, A.; Devereux, R. B., Relation of arterial pressure waveform to left ventricular and carotid anatomy in normotensive subjects. *Journal of the American College of Cardiology* **1993,** *22* (7), 1873-1880.

76. Lee, M.; Chen, C.-Y.; Wang, S.; Cha, S. N.; Park, Y. J.; Kim, J. M.; Chou, L.-J.; Wang, Z. L., A Hybrid Piezoelectric Structure for Wearable Nanogenerators. *Advanced Materials* **2012,** *24* (13), 1759-1764.

77. Lipson, H.; Kurman, M., *Fabricated: The new world of 3D printing*. John Wiley & Sons: 2013.

78. Bose, S.; Vahabzadeh, S.; Bandyopadhyay, A., Bone tissue engineering using 3D printing. *Materials today* **2013,** *16* (12), 496-504.

79. Chia, H. N.; Wu, B. M., Recent advances in 3D printing of biomaterials. *Journal of biological engineering* **2015,** *9* (1), 4.

80. Lewis, J. A.; Ahn, B. Y., Device fabrication: Three-dimensional printed electronics. *Nature* **2015,** *518* (7537), 42.

81. Bodkhe, S.; Turcot, G.; Gosselin, F. P.; Therriault, D., One-step solvent evaporation-assisted 3D printing of piezoelectric pvdf nanocomposite structures. *ACS applied materials & interfaces* **2017,** *9* (24), 20833-20842.

82. Liang, H. W.; Liu, S.; Gong, J. Y.; Wang, S. B.; Wang, L.; Yu, S. H., Ultrathin Te nanowires: an excellent platform for controlled synthesis of ultrathin platinum and palladium nanowires/nanotubes with very high aspect ratio. *Advanced Materials* **2009,** *21* (18), 1850-1854.

83. Gao, M.; Li, L.; Li, W.; Zhou, H.; Song, Y., Direct writing of patterned, lead-free nanowire aligned flexible piezoelectric device. *Advanced science* **2016,** *3* (8), 1600120.

84. Wu, W.; DeConinck, A.; Lewis, J. A., Omnidirectional printing of 3D microvascular networks. *Advanced materials* **2011,** *23* (24), H178-H183.

85. Muth, J. T.; Vogt, D. M.; Truby, R. L.; Mengüç, Y.; Kolesky, D. B.; Wood, R. J.; Lewis, J. A., Embedded 3D printing of strain sensors within highly stretchable elastomers. *Advanced materials* **2014,** *26* (36), 6307-6312.

86. Park, J.; Wang, S.; Li, M.; Ahn, C.; Hyun, J. K.; Kim, D. S.; Kim, D. K.; Rogers, J. A.; Huang, Y.; Jeon, S., Three-dimensional nanonetworks for giant stretchability in dielectrics and conductors. *Nature communications* **2012,** *3* (1), 1-8.

87. Wang, Z.; Liu, X.; Shen, X.; Han, N. M.; Wu, Y.; Zheng, Q.; Jia, J.; Wang, N.; Kim, J. K., An Ultralight Graphene Honeycomb Sandwich for Stretchable Light-Emitting Displays. *Advanced Functional Materials* **2018,** *28* (19), 1707043.

88. Wang, Y.; Wang, R.; Wan, S.; Wang, Q.; Kim, M. J.; Ding, D.; Wu, W., Scalable nanomanufacturing and assembly of chiral-chain piezoelectric tellurium nanowires for wearable self-powered cardiovascular monitoring. *Nano Futures* **2019,** *3* (1), 011001.

89. Kim, K.; Zhu, W.; Qu, X.; Aaronson, C.; McCall, W. R.; Chen, S.; Sirbuly, D. J., 3D optical printing of piezoelectric nanoparticle–polymer composite materials. *ACS nano* **2014,** *8* (10), 9799-9806.

90. Mukhopadhyay, S. C., Wearable sensors for human activity monitoring: A review. *IEEE sensors journal* **2015,** *15* (3), 1321-1330.

91. Son, D.; Lee, J.; Qiao, S.; Ghaffari, R.; Kim, J.; Lee, J. E.; Song, C.; Kim, S. J.; Lee, D. J.; Jun, S. W., Multifunctional wearable devices for diagnosis and therapy of movement disorders. *Nature nanotechnology* **2014,** *9* (5), 397.

92. Heikenfeld, J.; Jajack, A.; Rogers, J.; Gutruf, P.; Tian, L.; Pan, T.; Li, R.; Khine, M.; Kim, J.; Wang, J., Wearable sensors: modalities, challenges, and prospects. *Lab on a Chip* **2018,** *18* (2), 217-248.

93. Leonov, V.; Vullers, R. J., Wearable electronics self-powered by using human body heat: The state of the art and the perspective. *Journal of Renewable and Sustainable Energy* **2009,** *1* (6), 062701.

94. Ha, M.; Park, J.; Lee, Y.; Ko, H., Triboelectric generators and sensors for self-powered wearable electronics. *Acs Nano* **2015,** *9* (4), 3421-3427.

95. Wu, M.; Wang, Y.; Gao, S.; Wang, R.; Ma, C.; Tang, Z.; Bao, N.; Wu, W.; Fan, F.; Wu, W., Solution-synthesized chiral piezoelectric selenium nanowires for wearable self-powered human-integrated monitoring. *Nano energy* **2019,** *56*, 693-699.

96. Khan, U.; Kim, S.-W., Triboelectric nanogenerators for blue energy harvesting. *ACS nano* **2016,** *10* (7), 6429-6432.

97. Yang, Y.; Zhang, H.; Lin, Z.-H.; Zhou, Y. S.; Jing, Q.; Su, Y.; Yang, J.; Chen, J.; Hu, C.; Wang, Z. L., Human skin based triboelectric nanogenerators for harvesting biomechanical energy and as self-powered active tactile sensor system. *ACS nano* **2013,** *7* (10), 9213-9222.

98. Chun, J.; Ye, B. U.; Lee, J. W.; Choi, D.; Kang, C.-Y.; Kim, S.-W.; Wang, Z. L.; Baik, J. M., Boosted output performance of triboelectric nanogenerator via electric double layer effect. *Nature communications* **2016,** *7*, 12985.

99. Lin, Z.-H.; Xie, Y.; Yang, Y.; Wang, S.; Zhu, G.; Wang, Z. L., Enhanced triboelectric nanogenerators and triboelectric nanosensor using chemically modified TiO2 nanomaterials. *ACS nano* **2013,** *7* (5), 4554-4560.

100. Chen, J.; Guo, H.; He, X.; Liu, G.; Xi, Y.; Shi, H.; Hu, C., Enhancing performance of triboelectric nanogenerator by filling high dielectric nanoparticles into sponge PDMS film. *ACS applied materials & interfaces* **2015,** *8* (1), 736-744.

101. Wang, Z.; Cheng, L.; Zheng, Y.; Qin, Y.; Wang, Z. L., Enhancing the performance of triboelectric nanogenerator through prior-charge injection and its application on self-powered anticorrosion. *Nano Energy* **2014,** *10*, 37-43.

102. Kim, S.; Gupta, M. K.; Lee, K. Y.; Sohn, A.; Kim, T. Y.; Shin, K. S.; Kim, D.; Kim, S. K.; Lee, K. H.; Shin, H. J., Transparent flexible graphene triboelectric nanogenerators. *Advanced materials* **2014,** *26* (23), 3918-3925.

103. Wang, Y.; Yang, Y.; Wang, Z. L., Triboelectric nanogenerators as flexible power sources. *npj Flexible Electronics* **2017,** *1* (1), 10.

104. Lai, Y. C.; Deng, J.; Liu, R.; Hsiao, Y. C.; Zhang, S. L.; Peng, W.; Wu, H. M.; Wang, X.; Wang, Z. L., Actively Perceiving and Responsive Soft Robots Enabled by Self-Powered, Highly Extensible, and Highly Sensitive Triboelectric Proximity-and Pressure-Sensing Skins. *Advanced Materials* **2018,** *30* (28), 1801114.

105. Bao, Y.; Wang, R.; Lu, Y.; Wu, W., Lignin biopolymer based triboelectric nanogenerators. *APL Materials* **2017,** *5* (7), 074109.

106. Wang, R.; Gao, S.; Yang, Z.; Li, Y.; Chen, W.; Wu, B.; Wu, W., Engineered and laser-processed chitosan biopolymers for sustainable and biodegradable triboelectric power generation. *Advanced Materials* **2018,** *30* (11), 1706267.

107. Liang, Q.; Zhang, Q.; Yan, X.; Liao, X.; Han, L.; Yi, F.; Ma, M.; Zhang, Y., Recyclable and green triboelectric nanogenerator. *Advanced Materials* **2017,** *29* (5), 1604961.

108. Ccorahua, R.; Huaroto, J.; Luyo, C.; Quintana, M.; Vela, E. A., Enhanced-performance bio-triboelectric nanogenerator based on starch polymer electrolyte obtained by a cleanroom-free processing method. *Nano Energy* **2019,** *59*, 610-618.

109. Xie, C.; Wang, X.; He, H.; Ding, Y.; Lu, X., Mussel-Inspired Hydrogels for Self-Adhesive Bioelectronics. *Advanced Functional Materials* **2020**, 1909954.

110. Pu, X.; Liu, M.; Chen, X.; Sun, J.; Du, C.; Zhang, Y.; Zhai, J.; Hu, W.; Wang, Z. L., Ultrastretchable, transparent triboelectric nanogenerator as electronic skin for biomechanical energy harvesting and tactile sensing. *Science advances* **2017,** *3* (5), e1700015.

111. Xu, W.; Huang, L. B.; Wong, M. C.; Chen, L.; Bai, G.; Hao, J., Environmentally friendly hydrogel-based triboelectric nanogenerators for versatile energy harvesting and self-powered sensors. *Advanced Energy Materials* **2017,** *7* (1), 1601529.

112. Liu, T.; Liu, M.; Dou, S.; Sun, J.; Cong, Z.; Jiang, C.; Du, C.; Pu, X.; Hu, W.; Wang, Z. L., Triboelectric-nanogenerator-based soft energy-harvesting skin enabled by toughly bonded elastomer/hydrogel hybrids. *ACS nano* **2018,** *12* (3), 2818-2826.

113. Liu, T.-Y.; Chen, S.-Y.; Lin, Y.-L.; Liu, D.-M., Synthesis and characterization of amphiphatic carboxymethyl-hexanoyl chitosan hydrogel: water-retention ability and drug encapsulation. *Langmuir* **2006,** *22* (23), 9740-9745.

114. Lee, J.; Kwon, H.; Seo, J.; Shin, S.; Koo, J. H.; Pang, C.; Son, S.; Kim, J. H.; Jang, Y. H.; Kim, D. E., Conductive fiber-based ultrasensitive textile pressure sensor for wearable electronics. *Advanced materials* **2015,** *27* (15), 2433-2439.

115. Han, L.; Liu, K.; Wang, M.; Wang, K.; Fang, L.; Chen, H.; Zhou, J.; Lu, X., Mussel-inspired adhesive and conductive hydrogel with long-lasting moisture and extreme temperature tolerance. *Advanced Functional Materials* **2018,** *28* (3), 1704195.

116. Guo, M.; Wu, Y.; Xue, S.; Xia, Y.; Yang, X.; Dzenis, Y.; Li, Z.; Lei, W.; Smith, A. T.; Sun, L., A highly stretchable, ultra-tough, remarkably tolerant, and robust self-healing glycerol-hydrogel for a dual-responsive soft actuator. *Journal of Materials Chemistry A* **2019,** *7* (45), 25969-25977.

117. Ngo, T. D.; Kashani, A.; Imbalzano, G.; Nguyen, K. T.; Hui, D., Additive manufacturing (3D printing): A review of materials, methods, applications and challenges. *Composites Part B: Engineering* **2018,** *143*, 172-196.

118. Highley, C. B.; Prestwich, G. D.; Burdick, J. A., Recent advances in hyaluronic acid hydrogels for biomedical applications. *Current opinion in biotechnology* **2016,** *40*, 35-40.

119. Yue, K.; Trujillo-de Santiago, G.; Alvarez, M. M.; Tamayol, A.; Annabi, N.; Khademhosseini, A., Synthesis, properties, and biomedical applications of gelatin methacryloyl (GelMA) hydrogels. *Biomaterials* **2015,** *73*, 254-271.

120. Zhang, Y. S.; Khademhosseini, A., Advances in engineering hydrogels. *Science* **2017,** *356* (6337), eaaf3627.

121. Zolfagharian, A.; Kouzani, A. Z.; Khoo, S. Y.; Moghadam, A. A. A.; Gibson, I.; Kaynak, A., Evolution of 3D printed soft actuators. *Sensors and Actuators A: Physical* **2016,** *250*, 258-272.

122. Yuk, H.; Lin, S.; Ma, C.; Takaffoli, M.; Fang, N. X.; Zhao, X., Hydraulic hydrogel actuators and robots optically and sonically camouflaged in water. *Nature communications* **2017,** *8*, 14230.

123. Zargar, V.; Asghari, M.; Dashti, A., A review on chitin and chitosan polymers: structure, chemistry, solubility, derivatives, and applications. *ChemBioEng Reviews* **2015,** *2* (3), 204-226.

124. Ma, C.; Gao, S.; Gao, X.; Wu, M.; Wang, R.; Wang, Y.; Tang, Z.; Fan, F.; Wu, W.; Wan, H., Chitosan biopolymer-derived self-powered triboelectric sensor with optimized performance through molecular surface engineering and data-driven learning. *InfoMat* **2019,** *1* (1), 116-125.

125. Wu, Q.; Therriault, D.; Heuzey, M.-C., Processing and properties of chitosan inks for 3D printing of hydrogel microstructures. *ACS Biomaterials Science & Engineering* **2018,** *4* (7), 2643-2652.

126. Qi, L.; Xu, Z.; Jiang, X.; Hu, C.; Zou, X., Preparation and antibacterial activity of chitosan nanoparticles. *Carbohydrate research* **2004,** *339* (16), 2693-2700.

127. Abdeen, Z.; Mohammad, S.; Mahmoud, M., Adsorption of Mn (II) ion on polyvinyl alcohol/chitosan dry blending from aqueous solution. *Environmental Nanotechnology, Monitoring & Management* **2015,** *3*, 1-9.

128. Nie, J.; Wang, Z.; Hu, Q., Chitosan hydrogel structure modulated by metal ions. *Scientific reports* **2016,** *6* (1), 1-8.

129. Nie, J.; Wang, Z.; Hu, Q., Difference between chitosan hydrogels via alkaline and acidic solvent systems. *Scientific reports* **2016,** *6*, 36053.

130. Croisier, F.; Jérôme, C., Chitosan-based biomaterials for tissue engineering. *European polymer journal* **2013,** *49* (4), 780-792.

131. Niu, S.; Wang, S.; Lin, L.; Liu, Y.; Zhou, Y. S.; Hu, Y.; Wang, Z. L., Theoretical study of contact-mode triboelectric nanogenerators as an effective power source. *Energy & Environmental Science* **2013,** *6* (12), 3576-3583.

132. Wang, Z. L., Triboelectric nanogenerators as new energy technology and self-powered sensors–Principles, problems and perspectives. *Faraday discussions* **2015,** *176*, 447-458.

133. London, G. M.; Guerin, A. P., Influence of arterial pulse and reflected waves on blood pressure and cardiac function. *American heart journal* **1999,** *138* (3), S220-S224.

134. Choi, S.; Park, J.; Hyun, W.; Kim, J.; Kim, J.; Lee, Y. B.; Song, C.; Hwang, H. J.; Kim, J. H.; Hyeon, T., Stretchable heater using ligand-exchanged silver nanowire nanocomposite for wearable articular thermotherapy. *ACS nano* **2015,** *9* (6), 6626-6633.

135. Hazarika, A.; Deka, B. K.; Kim, D.; Jeong, H. E.; Park, Y.-B.; Park, H. W., Woven Kevlar Fiber/Polydimethylsiloxane/Reduced Graphene Oxide Composite-Based Personal Thermal Management with Freestanding Cu–Ni Core–Shell Nanowires. *Nano letters* **2018,** *18* (11), 6731-6739.

136. Gupta, R.; Rao, K.; Srivastava, K.; Kumar, A.; Kiruthika, S.; Kulkarni, G. U., Spray coating of crack templates for the fabrication of transparent conductors and heaters on flat and curved surfaces. *ACS applied materials & interfaces* **2014,** *6* (16), 13688-13696.

137. Park, S.-H.; Lee, S.-M.; Ko, E.-H.; Kim, T.-H.; Nah, Y.-C.; Lee, S.-J.; Lee, J. H.; Kim, H.-K., Roll-to-Roll sputtered ITO/Cu/ITO multilayer electrode for flexible, transparent thin film heaters and electrochromic applications. *Scientific reports* **2016,** *6*, 33868.

138. Ma, Z.; Kang, S.; Ma, J.; Shao, L.; Wei, A.; Liang, C.; Gu, J.; Yang, B.; Dong, D.; Wei, L., High-performance and rapid-response electrical heaters based on ultraflexible, heat-resistant, and mechanically strong aramid nanofiber/Ag nanowire nanocomposite papers. *ACS nano* **2019,** *13* (7), 7578-7590.

139. Ghosh, D. S.; Chen, T. L.; Mkhitaryan, V.; Pruneri, V., Ultrathin transparent conductive polyimide foil embedding silver nanowires. *ACS applied materials & interfaces* **2014,** *6* (23), 20943-20948.

140. Hong, C.-H.; Oh, S. K.; Kim, T. K.; Cha, Y.-J.; Kwak, J. S.; Shin, J.-H.; Ju, B.-K.; Cheong, W.-S., Electron beam irradiated silver nanowires for a highly transparent heater. *Scientific reports* **2015,** *5*, 17716.

141. Huang, Q.; Shen, W.; Fang, X.; Chen, G.; Guo, J.; Xu, W.; Tan, R.; Song, W., Highly flexible and transparent film heaters based on polyimide films embedded with silver nanowires. *RSC Advances* **2015,** *5* (57), 45836-45842.

142. Yuk, H.; Lin, S.; Ma, C.; Takaffoli, M.; Fang, N. X.; Zhao, X., Hydraulic hydrogel actuators and robots optically and sonically camouflaged in water. *Nature communications* **2017,** *8* (1), 1-12.

143. Pelton, M., Modified spontaneous emission in nanophotonic structures. *Nature Photonics* **2015,** *9* (7), 427.

144. Ahn, J.; Lim, T.; Yeo, C. S.; Hong, T.; Jeong, S.-M.; Park, S. Y.; Ju, S., Infrared Invisibility Cloak Based on Polyurethane–Tin Oxide Composite Microtubes. *ACS applied materials & interfaces* **2019,** *11* (15), 14296-14304.

145. Chen, C.; Hu, L., Super Elastic and Thermally Insulating Carbon Aerogel: Go Tubular Like Polar Bear Hair. *Matter* **2019,** *1* (1), 36-38.

146. Moghimi, M. J.; Lin, G.; Jiang, H., Broadband and ultrathin infrared stealth sheets. *Advanced Engineering Materials* **2018,** *20* (11), 1800038.

147. Ye, D.; Lu, L.; Joannopoulos, J. D.; Soljačić, M.; Ran, L., Invisible metallic mesh. *Proceedings of the National Academy of Sciences* **2016,** *113* (10), 2568-2572.

148. Liu, G.; Liu, Y.; Zhao, X., The influence of spherical nano-SiO2 content on the thermal protection performance of thermal insulation ablation resistant coated fabrics. *Journal of Nanomaterials* **2017,** *2017*.

149. Cai, L.; Song, A. Y.; Wu, P.; Hsu, P.-C.; Peng, Y.; Chen, J.; Liu, C.; Catrysse, P. B.; Liu, Y.; Yang, A., Warming up human body by nanoporous metallized polyethylene textile. *Nature communications* **2017,** *8* (1), 1-8.

150. Hsu, P.-C.; Liu, C.; Song, A. Y.; Zhang, Z.; Peng, Y.; Xie, J.; Liu, K.; Wu, C.-L.; Catrysse, P. B.; Cai, L., A dual-mode textile for human body radiative heating and cooling. *Science advances* **2017,** *3* (11), e1700895.

151. Benchabane, A.; Bekkour, K., Rheological properties of carboxymethyl cellulose (CMC) solutions. *Colloid and Polymer Science* **2008,** *286* (10), 1173.

152. Song, S. J.; Choi, J.; Park, Y. D.; Hong, S.; Lee, J. J.; Ahn, C. B.; Choi, H.; Sun, K., Sodium alginate hydrogel-based bioprinting using a novel multinozzle bioprinting system. *Artificial organs* **2011,** *35* (11), 1132-1136.

153. Lin, Y.-H.; Liang, H.-F.; Chung, C.-K.; Chen, M.-C.; Sung, H.-W., Physically crosslinked alginate/N, O-carboxymethyl chitosan hydrogels with calcium for oral delivery of protein drugs. *Biomaterials* **2005,** *26* (14), 2105-2113.

154. Chevva, H.; Chandran, R.; LaJeunesse, D.; Wei, J. In *Silver nanowires (AgNWs) growth in-situ on chitosan polymer matrix film for SERS application*, 2017 IEEE 17th International Conference on Nanotechnology (IEEE-NANO), IEEE: 2017; pp 885-889.

155. Lee, S.; Shin, S.; Lee, S.; Seo, J.; Lee, J.; Son, S.; Cho, H. J.; Algadi, H.; Al-Sayari, S.; Kim, D. E., Ag nanowire reinforced highly stretchable conductive fibers for wearable electronics. *Advanced Functional Materials* **2015,** *25* (21), 3114-3121.

156. Riyajan, S.-A.; Nuim, J., Interaction of green polymer blend of modified sodium alginate and carboxylmethyl cellulose encapsulation of turmeric extract. *International Journal of Polymer Science* **2013,** *2013*.

157. Solanki, H. K.; Shah, D. A., Formulation optimization and evaluation of probiotic Lactobacillus sporogenes-loaded sodium alginate with carboxymethyl cellulose mucoadhesive beads using design expert software. *Journal of Food Processing* **2016,** *2016*.

158. Zhang, Y.; Wang, S.; Li, X.; Fan, J. A.; Xu, S.; Song, Y. M.; Choi, K. J.; Yeo, W. H.; Lee, W.; Nazaar, S. N., Experimental and theoretical studies of serpentine microstructures bonded to prestrained elastomers for stretchable electronics. *Advanced Functional Materials* **2014,** *24* (14), 2028-2037.